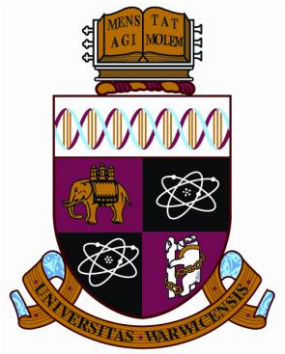

Developments of New Techniques for Studies of Coupled Diffusional and Interfacial Physicochemical Processes

By

Tahani Mohammad Bawazeer

A thesis submitted for the degree of

Doctor of Philosophy

Department of Chemistry

United Kingdom

December 2012

THE UNIVERSITY OF WARWICK

For

my parents…

my husband…

and my Children…

I would never have

reached this point without you,

and I will never be able to thank you enough

List of Illustrations

List of Tables

List of Abbreviations

1D	One Dimensional
2D	Two Dimensional
3D	Three Dimensional
AFM	Atomic Force Microscopy
Ag/Agcl RE	Silver/Silver Chloride Reference Electrode
ATP	Biosphere Adenosine Triphophate
CA	Chronoampermoetry
Ccvd	Catalysed Chemical Vapour Deposition
CE	Counter Electrode
CLSM	Confocal Laser Scanning Microscopy
CNT	Carbon Nanotube
CV	Cyclic Voltammetry
DNQ	Diazonaphthoquinone
DSPG	Distearoyl phosphatidylglycerol 1,2-ditetradecanoyl-sn-glycero-3-phospho-(1'-rac-glycerol)
EPC	Egg Phosphatidylcholine
F^{2-}	Fluorescein Monoanion
FEM	Finite Element Model
FH^{-}	Fluorescein Dianion
FH_2	Fully Protonated Form Of Fluorescein
FISE	Fluoride Ion Selective Electrode
GC	Glassy Carbon
HAP	Hydroxyapatite
HOMO	Highest Occupied Molecular Orbital
ICP-MS	Inductively Coupled Plasma Mass Spectroscopy
IC-SECM	Intemitting Contact Scanning Electrochemical Microscopy
LSV	Linear Sweep Voltammetry
LUMO	Lowest Unoccupied Molecular Orbital
MWNT	Multi-walled carbon nanotube
ORR	Oxygen Reduction Reaction
SWNTs	Single-Walled Carbon Nanotubes
OTEs	Optically Transparent Electrodes

Ox	Oxidised Form Of A Species
PLG	Poly-l-Glutamic Acid
PLL	Poly-l-Lysine
RE	Reference Electrode
Red	Reduced Form Of A Species
RG	Ratio Of Glass To Wire
ROI	Region of Interest
RBM	Radial Breathing Mode
$Ru(Bpy)_3^{2+}$	Tris(2,2'-Bipyridine)Retheniun
SA-AFM	ScanAsyst-atomic force microscopy
SECM	Scanning Electrochemical Microscopy
SEM	Scanning Electron Microscopy
SLB	Supported Lipid Bilayer
SUVs	Small Vesicle Fusion
TCNQ	Tetracyanoquinodimethane
UME	Ultra Micro Electrode
UV	Ultraviolet
Vis	Visible
WE	Working Electrode

List of Symbols

a	disc electrode radius
A	electrode area
D_j	diffusion coefficient of species j
F	Faraday's constant
i	current
i_{lim}	limiting current
n	number of electrons transferred during the electrode reaction
P	pressure
RG	radius of the insulating glass sheath surrounding an electrode relative to
T	temperature
t	time
ρ	density
λ	wavelength
δ	diffusion layer thickness
J_j	diffusive flux of species j to/from the electrode
k	rate constant
j	current density
c_j	concentration of species j
V	velocity vector
z_j	charge on species
φ	electrostatic potential

r_{glass}	radius of insulating glass
E_1	initial applied potential in a CV or LSV
E_2	final applied potential in an LSV or switching potential in a CV
c^*	bulk concentration
C_i	concentration of species i
D_i	diffusion coefficient of species
R_i	net production of species i
h_{surf}	height of the surface
d	UME-surface separation
h_{UME}	height of the UME
r_{UME}	radius of the active UME
r_{pit}	radius of the etch pit
r_{surf}	radius of the surface

Acknowledgment

I would like to thank my supervisor, Professor Patrick Unwin, whose support, advice and enthusiasm has been invaluable throughout my PhD. Thank you so much Pat, for giving me the chance to be a PhD student in your group, for being such a great supervisor, for miraculously coming up with time to read this thesis, also being so patient with me during the period of my PhD and the last stage of it. Thanks also go to Professor Julie Macpherson for useful discussions, for her help with the nanotube work, for knowing how to motivate me, and for listening to my problems.

Huge thanks also go to Dr. Massimo Peruffo, your intuition, patience and kindness are limitless. I would also like to thank Dr. Alex Colburn for manufacturing the galvanostat which made the research in Chapters 4 and 5 possible. With special thanks to workshop staffs Marcus Grant and Lee Butcher for making CLSM cells and other vital equipments. I was fortunate to work in a very pleasant Electrochemistry and Interfaces Group; I would like to thank all the members of them, past and present. Your friendship has meant a lot to me and we have had lots of good times. I offer my thanks to my friends outside who were always there when I needed them, who were always there to keep my feet firmly on the ground.

I must also thank the Ministry of Higher Education and Umm Al-Qura University in kingdom of Saudi Arabia for the full financial support of my study. Special thanks for the recognition of this work as Distinguished Research Award from Royal Embassy of Saudi Arabia, Cultural Bureau in London, based on achievements during my PhD research.

I would like to express my heartfelt gratitude to my wonderful husband and best friend Dr. Mohammad S. Alsoufi and my lovely children (Rahaf, Moutaz and Anas) for your constant love, understanding and patience during my study and for your continual faith in me, even when I am at my most difficult. Without your love and support this last year would have been impossible and I am ever thankful to be blessed with you in my life.

Finally, I would like to thank my family especially to my Mom and Dad. Your love and support has got me through this. I can only hope that I have made you proud.

Declaration

The work contained within this thesis is my own, except where acknowledged as for following collaborations: *(i)* finite element simulations in CHAPTER 4 were performed with Dr. Martin Edwards; *(ii)* the growth procedure for producing single-walled carbon nanotubes mats used in CHAPTERS 3 was developed by Dr. Agnieszka Rutkowska; *(iv)*enamel studies were carried out in conjunction with Dr. Carrie-Anne McGeouch-Flaherty; *(v)*Proton Lateral Diffusion studies were carried out in conjunction with Binoy Paulose. I confirm that this thesis has not been submitted for a degree at another university.

Parts of this thesis have been published as detailed below:

- Visualisation of electrochemical processes at optically transparent carbon Nanotube ultramicroelectrodes (OTCNT-UME) Agnieszka Rutkowska, **Tahani M. Bawazeer**, Julie V. Macpherson and Patrick R. Unwin. *PCCP*, **2010**, 82, (22), 9233-8.

- A Novel Approach to Study Proton Dispersion Kinetics: Application to Enamel Dissolution and the Effect of Inhibitors using Confocal Laser Scanning Microscopy Coupled with Scanning Electrochemical Microscopy. **Tahani. M. Bawazeer**, C-A. McGeouch, M. Peruffo, M.A. Edwards, A. Colburn, P. R. Unwin. *In Preparation.*

- Combined Confocal Laser Scanning Microscopy - Electrochemical Techniques for the Investigation of Proton Lateral Diffusion at Surfaces. **Tahani. M. Bawazeer**, B. Paulose, M. Peruffo, A. Colburn, P. R. Unwin. *In Preparation.*

Tahani Mohammad Bawazeer
Department of Chemistry
Warwick University, UK

Abstract

This study is concerned with the development and application of electrochemical techniques combined with confocal laser scanning microscopy (CLSM) as a probe of the kinetics of electrochemical and surface reactions at different interfaces. A CLSM set up has been designed which combines electrochemical and microscopic techniques to extend the applications of CLSM in a new research fields. This methodology has been applied to various electrochemical systems in this thesis. The electrochemical activity of ultramicroelectrodes (UMEs) has been quantified using CLSM. A special optically transparent electrode, comprising a thin film of carbon nanotube network has been developed for these studies. The methodology comprises of tracking the dynamic, reversible concentration profiles of electroactive and photoactive tris(2,2'-bipyridine)ruthenium(II) species in aqueous solutions during cyclic voltammetry experiments. A decrease of the solution intensity is recorded at and around the UME surface during the oxidation of luminescent $Ru(bpy)_3^{2+}$ to non-luminescent $Ru(bpy)_3^{3+}$, followed by an increase of the intensity signal in the reverse scan direction as the oxidized $Ru(bpy)_3^{3+}$ is consumed at the electrode surface. A three dimensional map of the concentration gradients of $Ru(bpy)_3^{2+}$ is constructed by collecting sections of the object across the normal to the electrode plane at the steady state current regime. The first use of CLSM coupled with scanning electrochemical microscopy (SECM) has been introduced as a means of time dependent visualisation and measurement of proton dispersion at dental enamel surfaces and the effectiveness of inhibitors on substrates. This new technique provides an analytical method with high spatial and temporal resolution permitting sub-second analysis of treatment effects on enamel substrates. In this case the UME tip of SECM is used to generate protons galvanostatically in a controlled manner and the resulting proton fields were quantified by CLSM using a pH sensitive fluorophore. Given the advantage of SECM to deliver high controllable, and local acid challenges in a defined way, and the high temporal and spatial resolution in the millisecond and micrometer range, respectively, in CLSM allows the surface kinetics of dissolution and the effect of barriers on the enamel surfaces to be evaluated. Finite element model has been used to describe the dissolution process, which allows the kinetics to be evaluated quantitatively, simply by measuring the size of pH profiles over time. Fluoride and zinc were used as treatments for enamel surfaces to investigate the effect of inhibitors on proton distribution, since they are generally considered to impede the dissolution process. Proton lateral diffusion at modified surfaces was also investigated using CLSM and SECM to validate the use of these techniques. A disc UME was brought close to the membrane and the oxidation of water was induced. Proton lateral diffusion was observed as a change in pH along the membrane. Different electrostatic interactions were investigated by functionalising the surface with different phospholipid head group and polypeptide multilayer films, since they are thought to have an effect on facilitate or retreat the process. Anionic lipids head groups share protons as acid-anion dimmers and thus trap and conduct protons along the head group domain of bilayers that contain such anionic lipids. The results also indicate the rate and mobility of proton diffusion along membrane are largely determined by the local structure of the bilayer interface.

Introduction

Introduction

The ultimate aim of this thesis is to obtain quantitative insights into concentration gradients developed near active surfaces using a combination of experimental techniques and numerical simulation methods. In this introduction the fundamentals of dynamic electrochemistry and electrochemical processes are briefly considered, with a focus on ultramicroelectrodes. This chapter also provides a discussion of the principle and previous work on the experimental techniques used, including fluorescence confocal laser scanning microscopy (CLSM), and scanning electrochemical microscopy (SECM).

1.1. Fluorescence Confocal Laser Scanning Microscopy

1.1.1. Literature Survey

In the 1980s, there were rapid innovations and improvements in the images obtained from common microscopes such as the fluorescence microscope. Although this type of microscope had been invented in 1904, it did not become really effective until the end of the 1970's and beginning of the 1980's [1,2] when the structure of the cytoskeleton was revealed by attaching fluorescent labels to antibodies, that were applied to cells.[1] This approach provoked a great deal of interest and, as a result, applications increased in a variety of fields which had been previously dominated by biochemistry and electrophysiology methods.[1-3] This epi-illumination fluorescence microscopy found its main application in cell biology and a huge amount of work was reported using this

technique.[2-4] However, a major problem is that conventional (widefield) microscopy of any thick biological sample often yields blurred, low-contrast images in which the fine details of cell structure are obscured.[3,5] This results primarily from the scatter of light from the specimen, and light coming from out-of-focus optical planes. To improve this, there was an attempt by Naora to build a confocal optics system based upon a theoretical concept from his supervisor Koana to perform high resolution micro-spectrophotometry.[2]

In 1957, Minsky [4-6] developed the first confocal microscopy in order to resolve the fine details of brain tissue to gain a fundamental understanding of the brain.[7] This quest led him to create a system that was able to obtain an optical section through a thick specimen,[3] that is, to systematically collect two dimensional (2D) images from different levels of depth in the tissue with the same high contrast and clarity. Minsky's development was facilitated by the addition of a scanning stage which enabled his invention to scan the sample and generate 2D images of specimens.[1,4,6-7] A further improvement resulted by using a (confocal) pinhole aperture to remove light that was focused above and below the focal plane, since these beams were focused behind and before the confocal pinhole and so did not reach the detector. This removes much of the out-of-focus blur that is often visible with conventional optical microscopy.[4,7] Minsky's approach initiated a series of confocal microscopy developments that by the mid 1980's became commercially available. Many of these developments have been summarised in several reviews.[1-4,6-7] CLSM is discussed further in section 1.1.2.

Nowadays, fluorescence microscopy of either the conventional widefield microscope or the more recent confocal microscope is a widely used method in biophysical studies, the

main advantage being that the signal to noise ratio is high since, under ideal conditions, the background dose not fluoresce.[3,5] Both of these have relatively different applications depending on the type of sample, with CLSM performing better on thick samples and widefield microscopes on thin ones if no deconvolution is applied.[7] The methodology is specific, as fluorescent molecules absorb and emit light at characteristic wavelengths with the signal being sensitive to small numbers of fluorescent molecules and to changes in the chemical environment. The availability of hundreds of fluorescent labels with known excitation and emission curves has accelerated and expanded the application of these fluorescence microscopes in biological research as well as in the physical sciences.[8-9]

In general, the confocal scanning optical microscope is undoubtedly the most significant advance in optical microscopy within the last few decades and has become a powerful tool for biologists, material scientists and microelectronics engineers.[10] In conventional epi-illumination fluorescence microscopy, the simultaneous illumination of the entire field of view of a specimen will excite fluorescent emissions throughout a considerable depth of the specimen, rather than just at the focal plane (Figure 1.1(a)). The image is thus formed from a high proportion of light, which is out of focus, seriously degrading the final image, by reducing contrast and sharpness (Figure 1.1(b)). A major advantage of CLSM over conventional fluorescence microscopy[3,5] is the removal of the out-of-focus interference by introducing two pinhole apertures at the light source and detecting apparatus of the microscope; this has the benefit of allowing the efficient filtering of light from regions outside the focal plane which may otherwise contribute to the signal.

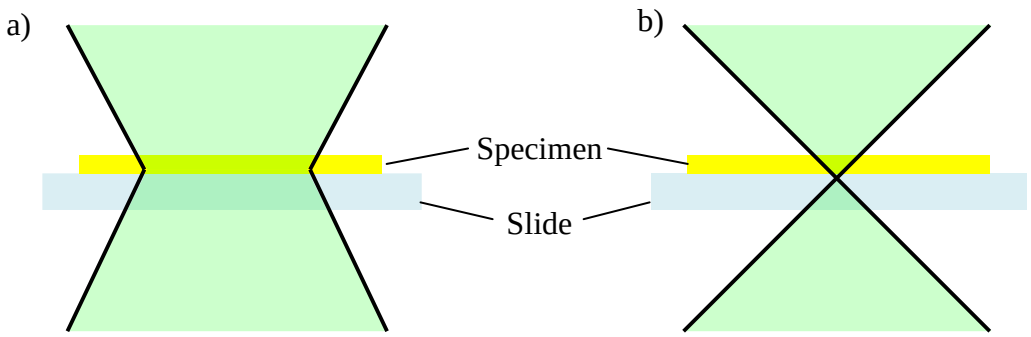

Figure 1.1: **(**a) Full-field illumination (b) Single point illumination

1.1.2. CLSM Principle

In CLSM, a beam of excitatory laser light from the illuminating aperture passes through an excitation filter and is reflected by a dichroic mirror to be focused by the microscope objective lens to a diffraction limited spot at the focal plane. [2-3,5,11] Fluorescence emissions excited both within the illuminated in-focus region, and within the illuminated cones above and below it, are collected by the objective and pass through the dichroic mirror and emission filter. However, only emissions from the in- focus region are able to pass through the confocal detector aperture, or pinhole, to be detected by the photomultiplier. This process is demonstrated schematically in Figure 1.2.[10-11]

In particular, fluorescence CLSM is a powerful and non-invasive in-situ technique which allows a 2D and 3D imaging of a sample.[12-17] 3D imaging of the sample may be constructed using a technique known as a z-stack illustrated in Figure 1.3. A 3D confocal image is created by collecting light from a single focal point of the sample at a time tracking many slices through the sample in the z-direction. These slices are then reconstituted into a three-dimensional picture by the software. A time series can be set

up so that an image or a z-stack can be taken at certain time intervals. This means that a reaction can be monitored over a particular time scale of interest.[10]

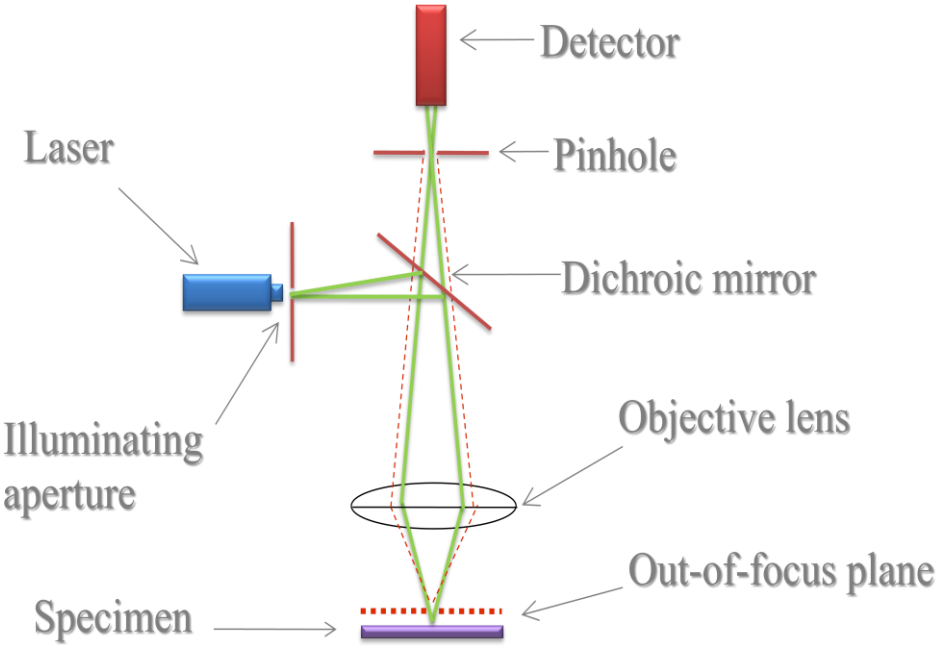

Figure 1.2: Schematic diagram of a confocal microscope.

There are certain considerations that must be made when using CLSM. A potential drawback of scanning microscopes, in general, is the time taken to obtain an image. In full-field illumination, the entire image is taken at once and thus a time series of images can be generated at video rates. In CLSM, the series of points required to generate an entire image is dependent on how rapidly the laser beam can be scanned across the surface. Normally, this is done using two oscillating mirrors that deflect the laser beams to cover the whole sample.[18] Thus, if time resolution is required, a one-dimensional line scan can be used instead of a two-dimensional image and this reduces the acquisition time considerably.

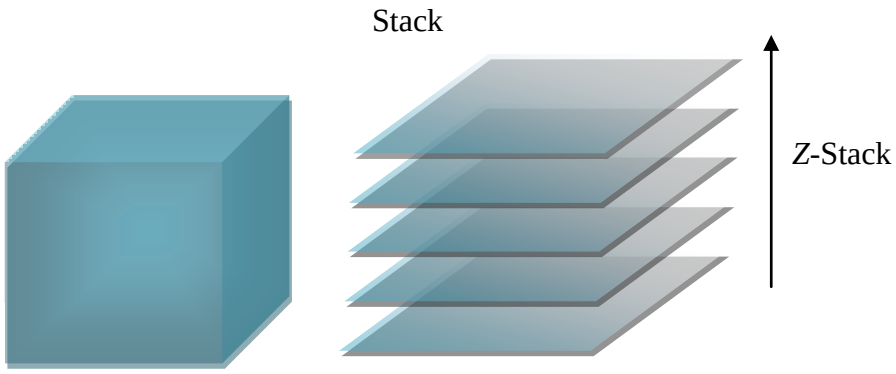

Figure 1.3: Schematic of 3D *z*-stack imaging in CLSM.

Another important factor is the size of the pinhole. The smaller the pinhole used, the smaller the depth of focus. However, the use of very small pinholes may lead to darkening of the images because insufficient light can reach the detector. Thus, there is always a compromise between image clarity and pinhole size. Moreover, as discussed above, both fluorescent and reflected light from the sample pass back to a detector (photodiode system) through the objective in use. The objective lens parameters: (i) magnification, (ii) numerical aperture (NA) and (iii) free working distance, determine the resolution capacities of a given objective.[3,5] The finest detail of the sample, that can be visualised with a microscope, is proportional to λ=NA (λ is the wavelength of the light).

1.1.3. Fluorescence

CLSM is particularly effective when fluorescent dyes are excited with the sharp band width of a laser. The fluorophores subsequently emit light of a sufficiently different wavelength to allow separation of the excitation and emission signals. The process involved in fluorescence is shown in a Jablonski diagram in Figure 1.4. A photon of

energy hv_{ex} excires an electron from the ground state of molecule (S_0) (1) into vibrationally excited singlet state (S_1^v) (2)(one or higher excited state of a higher energy).[18-19] This excited state typically has a lifetime of 1-10 nanoseconds, and during this period the fluorophore may undergo conformational changes or be subject to possible interactions with its molecular environment. During these processes the energy of (S_1^v) is partially dissipated to yield a relaxed singlet excited state, (S_1^v) (3). Finally, a photon of energy hv_{em} is emitted returning the fluorophore to its ground state, S_0 (1).[18]

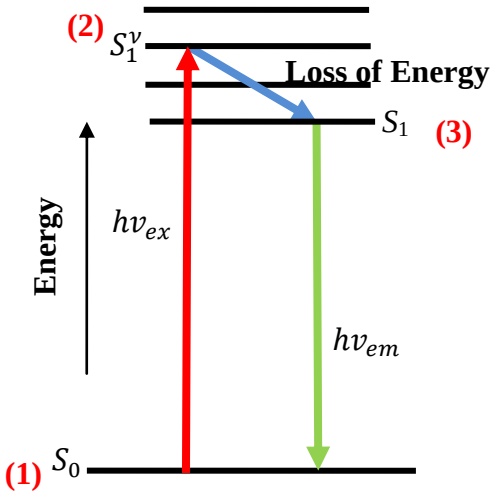

Figure 1.4: A Jablonski diagram showing the origin of fluorescence, with the photoexitation of an electron from (1) to (2) and emission light when the electron moves from (3) to (1).

The difference between the positions of the band maxima of the excitation and emission wavelengths is known as the Stokes' shift (see Figure 1.5). The wavelength of the emitted light is characteristically longer than the wavelength of the absorbed light, as the energy of the emitted photon is lower due to the energy dissipation when the molecule is in the excited state. A large Stokes shift is a valuable attribute when trying

to detect the fluorescence since this means that the excitation and emitted photons can be easily distinguished and thus separated.

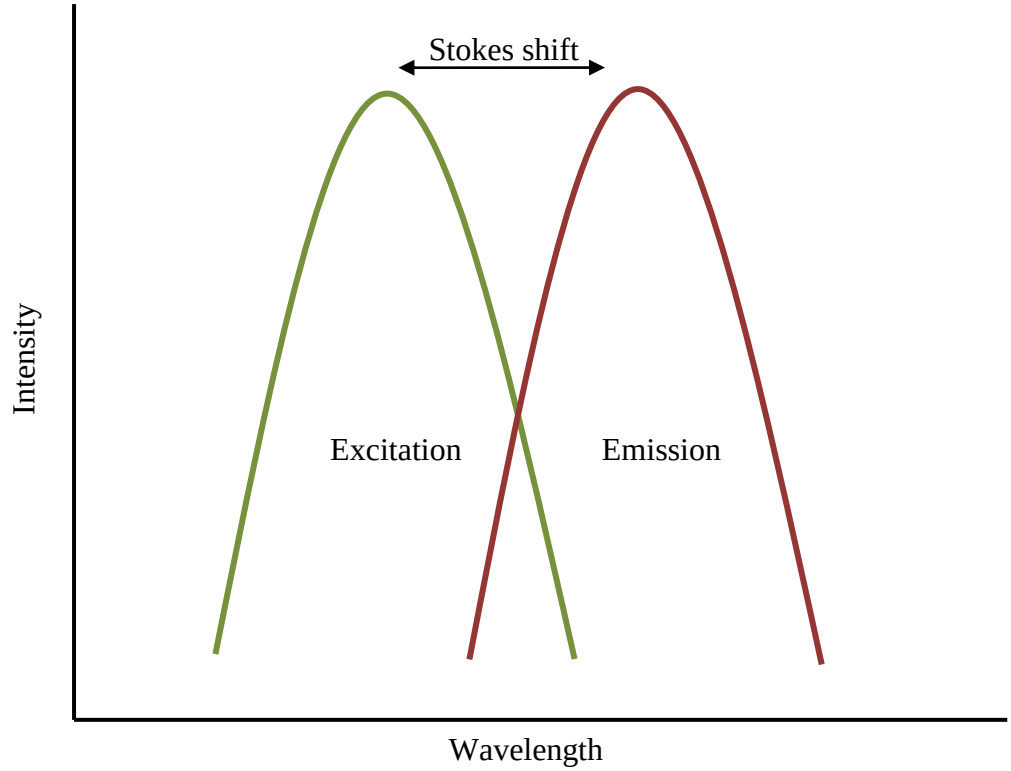

Figure 1.5: Definition of Stokes shift

1.1.3.1. Fluorescein

A molecule that is fluorescent is often called a fluorophore or a fluorescent dye. Fluorophores are fluorescent molecules which are usually polyaromatic hydrocarbons.[20-21] They are generally used to label biological molecules and they respond to changes in their surroundings. A commonly used fluorophore, and one of particular relevance to this thesis, is fluorescein. Fluorescein is Bronsted-Lowry acid with a p*K*a 6.4[22] for the main ionization equilibrium of the mono and deprotonated form. The maximum excitation peak of fluorescein occurs at 494 nm; emission occurs only for the deprotonated form with maximum peak at 518 nm.[3]

$$HF \leftrightarrow F^- + H^+ \quad (1.1)$$

Figure 1.6 (blue squares) shows a sigmoidal relationship of fluorescein fluorescence intensity (normalized) collected at the marked pH values.[15,17] No fluorescence was observed below pH 5 and no increase in fluorescence occurred above pH 7. A calibration curve was obtained by a sigmoidal 3 parameter empirical fit.[23]

$$I = 1 - \frac{1}{1 + \exp[(\mathrm{pH} - a)/b]} \quad (1.2)$$

where a and b are fitting parameters.

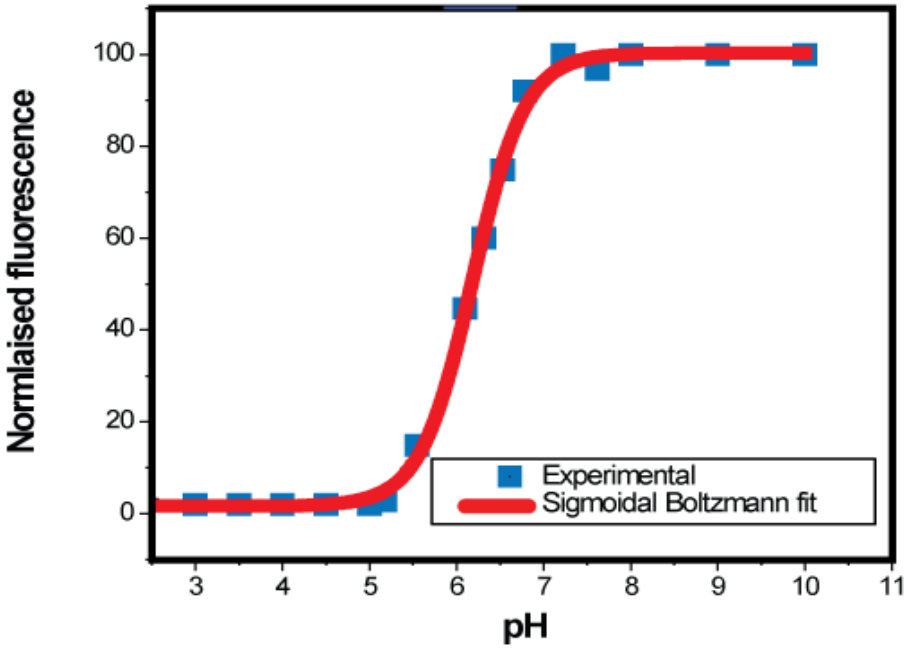

Figure 1.6: Illustration of intensity of fluorescence vs. pH after fluorescein excitation at 488 nm and detection at 530 nm.

The major change in intensity occurs between pH 5.5 and 7. The structure of fluorescein is shown in Figure 1.7. It has a very intense, pH dependent fluorescence signal. Fluorescein has 2 weak acid groups in this range and the sensitivity of fluorescein to changes in pH is due to a reconfiguration of the pi-electron system that occurs during the protonation of both the phenol and carboxylic acid groups in the fluorescein molecule.[19,24] At high pH, it is in its anionic highly fluorescent form and the

fluorescence emission spectrum of fluorescein is dominated by the dianion with only small contribution from the monoanion until the pH falls below ca. 6.5 at which point the monanion becomes the prevalent species. The phenolic proton has a p*K*a of 6.5, whilst the carboxylic acid group has a p*K*a of 4.4.[19] At very low pH, the quinine carbonyl group becomes protonated (p*K*a 2.1). Only the dianion is fluorescent, thus there is a sharp decrease in fluorescence at low pH where the neutral and cationic species dominate.

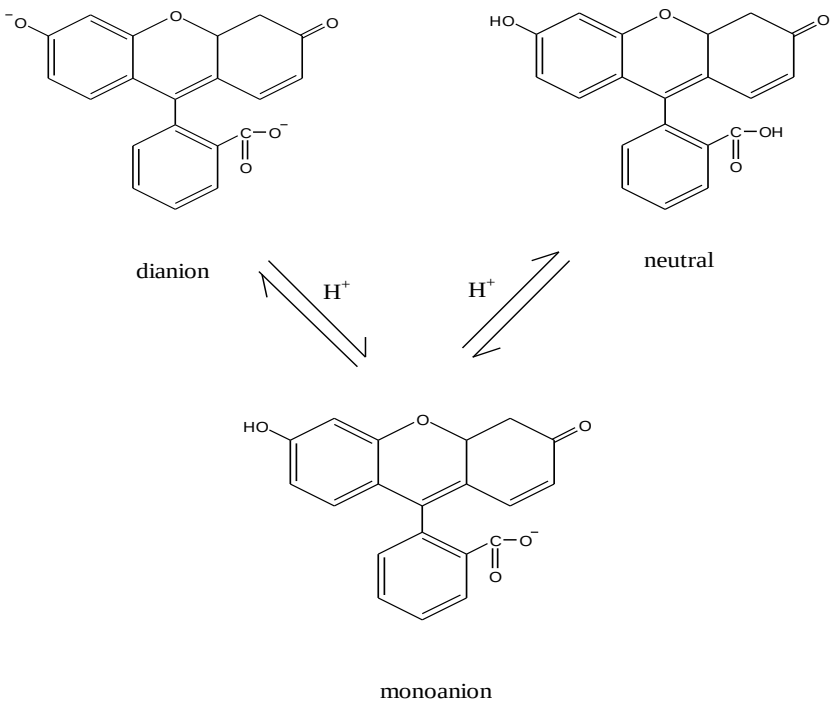

Figure 1.7: Molecular structures of neutral fluorescein and its anions.

The use of CLSM and fluorescein as a pH dependent probe of local pH is fundamental of much of the work in this thesis.

1.2. Electrochemistry and Microelectrodes

1.2.1. Introduction to electrochemistry

The simplest electrode system is when a metal (or object) is placed in an electrolyte solution. This results in charge transfer at the interface between the electrode and the electrolyte, where gradients in electrical and chemical potentials constitute the driving force for electrochemical reactions. An electrical double layer forms [25-26] with the model outlined in Figure 1.8 showing a representation of the Grahame model. [27] This classical approach describes the electric double layer (EDL) of a metal electrolyte interface by a plate condenser of molecular dimensions. One plate is the metal surface with its excess charge; the other is formed by the solvated ions at closest approach. The solvated ions that form the outer Helmholtz plane (OHP) and that are held in position by purely electrostatic forces are termed "nonspecifically adsorbed". These are mainly solvated cations.

Most anions, however, if the electrode is positively charged give away part of that solvation shell when entering the double layer to form a chemical bond with the electrode surface. These ions are termed "specifically adsorbed" and their centres form the inner Helmholtz plane (IHP). In addition, the electrolyte may also contain specifically or non-specifically adsorbed organic molecules as well as redox-active species. Much of the importance of electrochemistry lies in the ways that these potential differences can be related to the thermodynamics and kinetics of electrode reactions. In particular, manipulation of the interfacial potential difference affords an important way of exerting external control on an electrode reaction. [28]

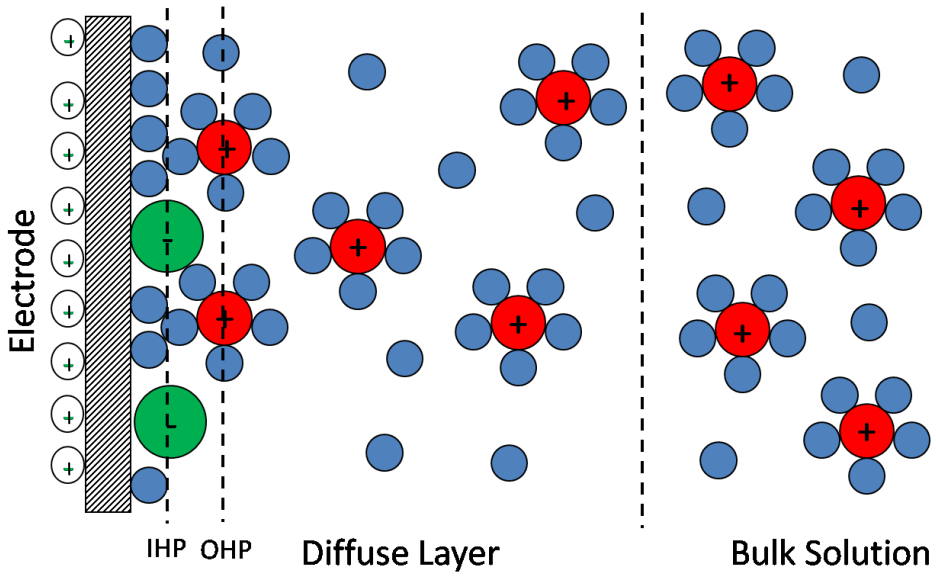

Figure 1.8: A diagrammatic representation of the electrical double layer where the red cations are solvated with small blue circles representing water molecules, and large green anions are specifically adsorbed onto the electrode surface.

The double layer is frequently represented in an equivalent circuit as a capacitor. The current flowing due to the changing of the composition of the double layer is usually termed the charging current. It can limit the sensitivity of electrochemical measurements, particularly in a temporal sense. Also as the double layer can be thought of as a parallel plate capacitor, the size (spacing) is dependent on the concentration of electrolyte.[25-26] High electrolyte concentrations reduce the size of this double layer.

1.2.2. Dynamic electrochemistry

Dynamic electrochemistry involves the study of charge transfer processes between an electrode (normally metallic) and a redox-active species under non-equilibrium conditions. The simplest experimental system includes a working electrode (WE) (the location of the redox reactions) and a reference electrode (RE) relative to which the applied potential is measured. The reaction of interest takes place at the WE, and the

reference electrode is chosen to have constant composition, and therefore a fixed potential.[28] Where the typical current is expected to be greater than about 100 nA, a 3-electrode set-up is required. This introduction of a counter electrode is necessary as such large currents would otherwise perturb the fixed potential of the reference electrode and render it unstable (due to electrolysis of its components).[28]

Measurement of the current that flows provides information on the solution, the electrodes and the interfacial reactions. The rate of the WE reaction is influenced by several factors, including the rate of the electron transfer at the electrode surface, mass transport of the redox-active species to the electrode, chemical reactions in the solution, the nature of the electrode surface, and the structure of the interfacial region over which the reaction occurs.

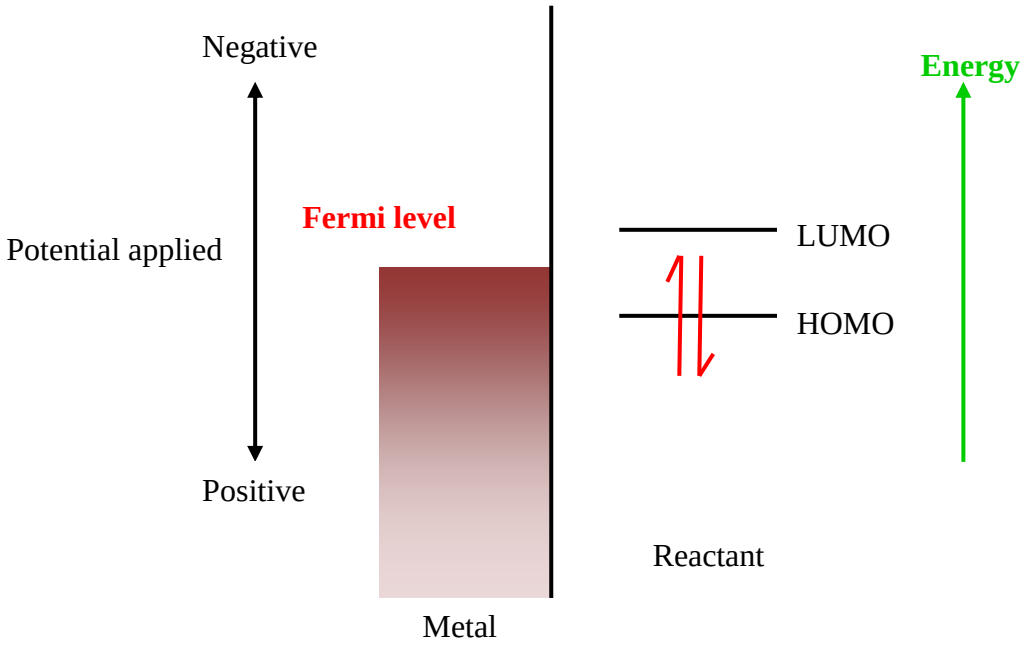

Figure 1.9: The effect of the applied potential on the Fermi level.[27]

The maximum of the continuum is known as the Fermi level. Application of a potential to the WE, with respect to the RE, can change the Fermi level of the metal used as the electrode (see Figure 1.9). While the Fermi level is of an energy between that of the lowest unoccupied molecular orbital (LUMO) and the highest occupied molecular orbital (HOMO), no electron transfer will occur. If a sufficiently negative potential is applied, the Fermi level increases in energy such that it is above the LUMO. In this situation, electron transfer occurs from the metal to the reactant, causing reduction of the reactant. Conversely, if a sufficiently positive potential is applied, the Fermi level decreases in energy such that it is below the HOMO. Electron transfer proceeds from the reactant to the metal electrode, leading to oxidation of the reactant.[27]

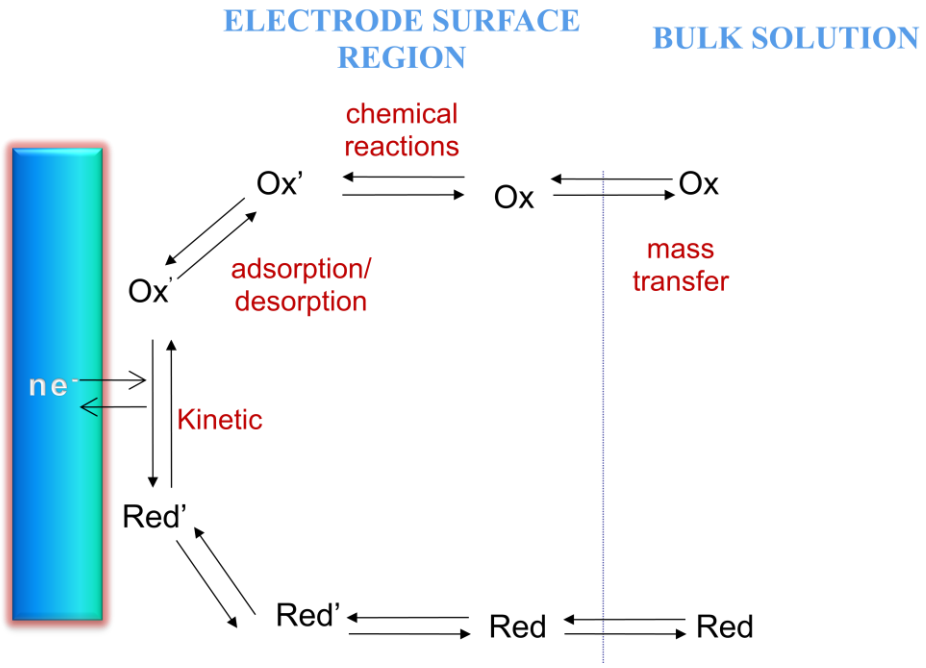

Figure 1.10: A schematic representation of a typical electrode reaction.[28]

The reaction rate of a typical electrode reaction involves several steps, which are illustrated schematically in Figure 1.10. The overall reaction rate is limited by the slowest step. It is often the case that the applied potential is increased to such an extent that the electron transfer process occurs more rapidly than material can be transported to

or from the electrode. Under these conditions, the current response is limited by the rate of mass transport,[27] which is the subject of the next section. More complex reactions may involve chemical reactions in solution, either before or after electron transfer, and surface reactions such as adsorption or desorption. Protonation is a common chemical reaction that is often coupled to electron transfer which leads to the production of pH gradients between the interfacial region and bulk solution, if the solution is not buffered. The aim of this thesis is to image and quantify the pH gradients that develop at active surfaces. These can arise either through chemical reactions in solution or electrode reactions that produce or consume protons or hydroxide ions, for example tris(2,2'-bipyridine)ruthenium(II) oxidation (chapter 3) and water oxidation (chapter 4 and 5).

1.2.3. Mass transport

Mass transfer of dilute species in solution is governed by the Nernst-Planck equation[28] and for one-dimensional mass transfer along the *x*-axis the expression is as follows:

$$J_j = -D_j \nabla c_j + c_j \mathrm{V} - \frac{Z_j}{RT} D_j c_j \nabla \emptyset \qquad (1.3)$$

where J_j is the flux (i.e. the number of moles passing through a given area per unit time) of species j to/from the electrode, D_j is the diffusion coefficient of species j, c_j is the concentration of species j, **V** is the velocity vector, z_j is the charge on species j, F is the Faraday's constant, R is the gas constant, T is temperature and φ is the electrostatic potential. The three terms on the right hand side represents the contributions of diffusion, convection, and migration, respectively, to the flux.[25]

Thus, the factors contributing to mass transport include diffusion (movement along a concentration gradient), convection (the directed movement of the solution itself

carrying the species) and migration of the species (for example, the directed motion of ions due to some applied electrostatic potential).[28] An increase in any of these factors can promote mass transport, alleviating them as a possible rate limiting factor in reactions with fast electrode surface kinetics. Addition of a background electrolyte to a cell minimises any effects from migration, and can aid eliminating the development of liquid junction potential and prevent any contributions from ohmic drop by decreasing the resistivity of the solution. The background electrolyte does not take part/ interfere in the reaction occurring at the tip of WE but does decreases the size of the double layer at the electrode/surface interface; where a small double layer results in a high electric field, ensuring that the full potential applied at the electrode is available for the electrochemical process.[28-29]

Experimental conditions can be chosen so that no significant contribution is made by convection and migration so that diffusion is dominant (as discussed above). Thus, all mass transport models of fluxes in this thesis make use of only the diffusive aspects of the Nernst- Planck equation, significantly simplifying any numerical analysis of experimental results. To precisely quantify electrode reactions, it is necessary to take each aspect of mass transport into consideration.

1.2.3.1. Diffusion

Diffusion is always present in a dynamic electrode process and is defined as the movement of a species down a concentration (formally, activity) gradient, due to the difference in concentration (activity) of the species at the electrode surface and the bulk solution. Diffusion is described mathematically by Fick's laws[28], the first of which

(Equation 1.4) relates the diffusive flux to the concentration gradient (the rate of change of concentration with respect to distance).

$$J = -D\frac{\partial c}{\partial x} \tag{1.4}$$

where $\frac{\partial c}{\partial x}$ is the concentration gradient. The minus sign is because diffusion occurs down a concentration gradient. Fick's second law of diffusion describes the concentration of a species varies with time.

$$\frac{\partial c}{\partial t} = D\nabla^2 c \tag{1.5}$$

where ∇^2 is the Laplace operator which is also geometry dependent. Of particular relevance to the studies described herein are the 1D equations.[30]

$$\frac{\partial c}{\partial t} = D\frac{\partial^2 c}{\partial x^2} \tag{1.6}$$

where *c* is the concentration, and *x* the distance over which the concentration changes. Solution of Fick's second law can be used to give the variation in flux, or the diffusion-limited current with time.

In situations involving only diffusion, if the reaction on the surface proceeds more slowly than diffusion to the surface, the reaction is said to be kinetically controlled. In this case, the rate limiting process is the reactive step, meaning that by solving the diffusion equation coupled to appropriate boundary conditions, the actual surface reaction rate constant can be obtained. In some situations, the surface reaction may proceed in a diffusion-limited manner where the reaction is so fast that as soon as reactants are incident on the surface they are converted to product. In this case it is not possible to determine the rate constant from the data. However, it may be possible to increase mass transport by adding convection (movement induced by mechanical force

e.g. stirring), causing the reaction to become kinetically controlled as discussed in the next section.

1.2.3.2. Convection

Convection is the movement of species in a fluid due to an external mechanical force. The convective component of flux is given by:

$$J_{i,c} = C_i v \tag{1.7}$$

There are two types of convection. The first is *natural convection*, which can be present in any solution and arises from thermal gradients and/or density differences within the solution. Forced convection is normally orders of magnitude larger than natural convection, and so obscures any effect that natural convection may have. It arises when the solution is deliberately agitated which can be achieved in several different ways, leading to a multitude of convective (or hydrodynamic) systems.[31] In some electrochemical experiments an element of *forced convection* is deliberately introduced to swamp any contribution from natural convection, ensuring that reproducible experiments can be made over extended time-scales. Forced convection is usually achieved by external forces such as gas bubbling through solution, pumping, or stirring.[28]

1.2.3.3. Migration

From equation 1.1 it is apparent that migration only affects species which are charged. It is the movement of charged species under the influence of an external electric field ($\partial\varphi/\partial x$). Migrative flux is described by:

$$J_A = -\frac{z_i F}{RT} D_i C_i \nabla \emptyset \tag{1.8}$$

Due to the difficulty in quantifying its effect, migration is often removed during electrochemical experiments by the addition of an excess concentration of an inert supporting electrolyte.[28] As already mentioned, this also has the benefit of reducing the effect of uncompensated (Ohmic) resistance and compressing the size of the electrical double layer, such that the potential across the electrode/solution interface drops over a distance commensurate with electron transfer.[26,28] All studies in this thesis are carried out under conditions where migration can be ignored.

1.2.4 Ultramicroelectrodes (UMEs)

There are various types of electrodes employed and the critical factor determining their behaviour is the interplay between mass transport to the electrode and the electron transfer kinetics. The former may be directly linked to their size. Macroelectrodes have dimensions of the order of centimetres or millimetres; when one of the critical dimensions of the electrode is in the micrometer range, the electrode behaves as an ultramicroelectrode (UME).[32-35]

Ultramicroelectrodes, UMEs, have been widely used and characterised since the 1970's when it became apparent that electrodes of this type eliminated many of the unwanted characteristics of larger macro-electrodes, discussed below.[33,36-37] UME probes are generally fabricated using platinum, palladium, gold, silver wires or carbon fused into glass or embedded in plastic.[38-40] An electrical contact is then made by polishing away the extremity of the insulator to reveal the electrode material. Characterisation is often achieved using two electrochemical techniques: cyclic voltammetry (CV), and scanning electrochemical microscopy (SECM) in conjunction with optical microscopy.[39-40] These

techniques and their application in the characterisation of UMEs are discussed in sections 1.2.5.1and 1.2.6, respectively.

The exposed part of the metal can take different forms (Figure 1.14),[37,41] depending on the application[42] and on the method of fabrication such as: disc electrodes,[43] array, [44-45] band,[46-47] hemisphere, cylinder, spherical mercury electrodes,[48-49] ring electrodes,[50-51] and carbon fibre electrodes[52-53] ring,[54-55] but by far the most widely used is the disc electrode since its fabrication is relatively straight forward, the sensing area can be polished mechanically and it is easily modellable. The diffusion fields, which promote the movement of materials to and from the electrode, are dependent on the shape of the electrode and the timescale of the measurement. Diffusion processes that take place are shown schematically in Figure 1.11. All show substantial "edge effects" which lead to the enhanced mass transport rates.[41]

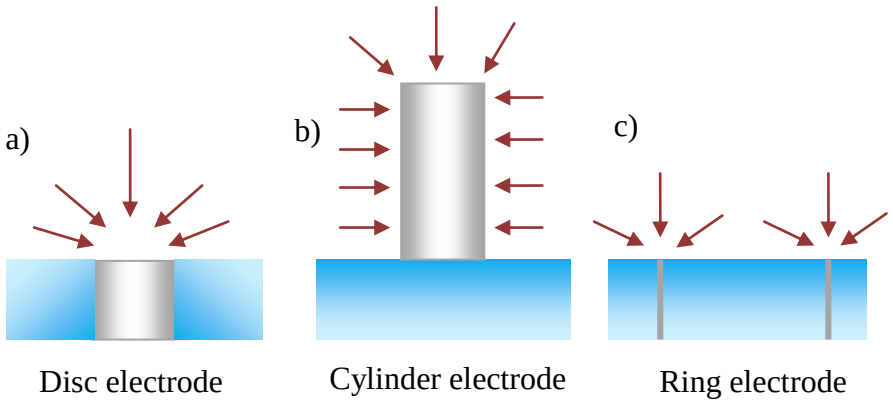

Figure 1.11: Different geometries of electrodes and their diffusion fields: (a) Disk electrode (b) Cylinder electrode and (c) Ring electrode. Reproduced from reference.[41]

The size of the working electrode is an important consideration in electrochemical experiments. First, we should consider the traditional macroelectrode. Diffusion to this type of electrode is predominately planar, as shown in Figure 1.12(*a*). In contrast, the small size of UMEs results in extremely efficient diffusional mass transport due to the

significant contribution of radial diffusion, resulting in the formation of a steady-state hemispherical diffusion field (in the case of a disc electrode). This is illustrated in Figure 1.12(b). Thus, more rapid and efficient mass transport occurs at a UME than that at a macroelectrode. This has important ramifications for the voltammetric response of UMEs, as discussed in section 1.2.5.

Thus, the use of UMEs allows fast kinetics to be observed and measured due to fast and well-defined mass transport properties as shown in Figure 1.12 [28,55] In comparison to larger electrodes in quiescent solution, the advantage of a UME is its ability to form a steady-state current under diffusion controlled conditions.[56] A small electrode area also results in a small charging current, allowing access to shorter time scales and fast response times. Small currents reduce effects from Ohmic drop, making UMEs effective in resistive media such as organic solutions, or in cases where electrolyte is not present.[57]

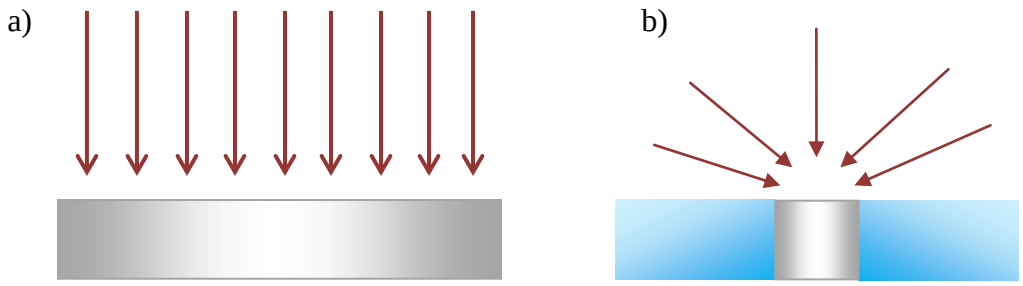

Figure 1.12: (a) Schematic of planar diffusion profile exhibited by a macroelectrode and (b) the hemispherical diffusion at disc UME.

The UME tip is often characterised by the *RG* value, which is the ratio of the radius of insulating glass, r_{glass}, to the electrode radius. It is defined as in equation (1.9), see Figure 1.13. For most SECM studies *RG* is typically around 10. This minimizes effects

from back diffusion (from behind the probe), making the electrode response more sensitive to the surface process when used in SECM.

$$RG = \frac{r_{glass}}{a} \quad (1.9)$$

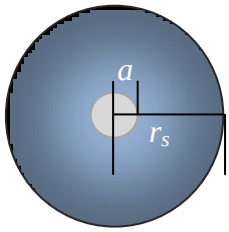

Figure 1.13: Showing the *RG* of an UME where *rs* is the radius of the whole UME and *a* is the radius of the metal wire.

1.2.5. Linear Sweep Voltammetry and Cyclic Voltammetry

Linear Sweep Voltammetry (LSV) and Cyclic voltammetry (CV)[58-59] are the simplest electrochemical techniques, and are used in most electrochemical investigations to provide information on the electrode/electrolyte interface. Consider the example electrode reaction $O + e^- \rightarrow R$. The basis of LSV is to ramp the potential linearly with time (V/s), at a particular scan rate. The potential increases from one where no reaction occurs, E_1, to a potential were electron transfer is driven very quickly, E_2. Upon reaching E_2, this will either oxidize or reduce an analyte of interest.

In CV, the direction of the sweep is reversed and the potential is scanned back to E_1. If the analyte of interest was reduced on the forward scan, the aim is that it may then be oxidised on the reverse scan, or vice-versa. This provides information on the reversibility of the reaction by analysis of the waveform produced; achieved by plotting the current recorded at the working electrode against the applied potential, as shown in Figure 1.14. At E_1, no reduction occurs and so the current is zero. As the potential

increases, the rate of reduction increases, and so the current increases approximately exponentially with increasing potential (and thus time), as predicted by the Butler-Volmer equation.[29] The current reaches a maximum value and a peak is seen. This occurs because the current depends not only on the rate constant for reduction, k_{red}, but also on the surface concentration of the redox species.

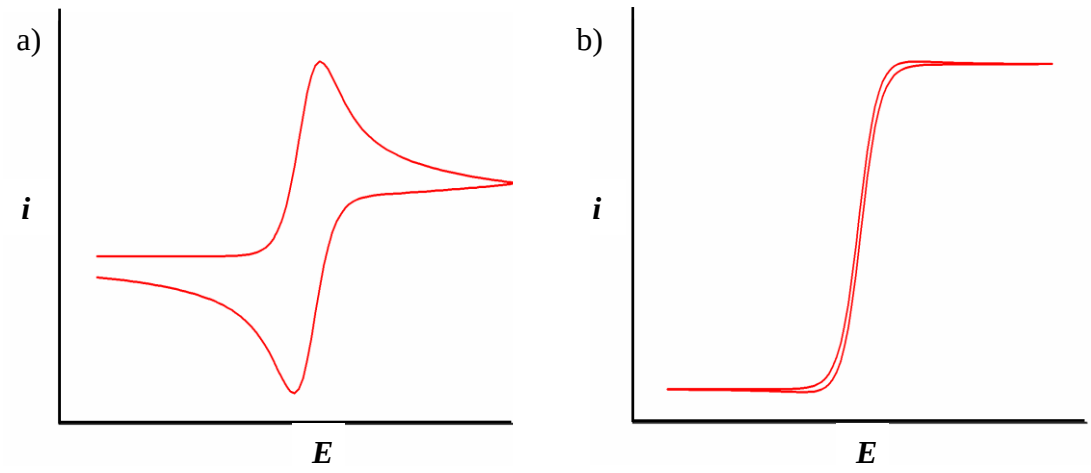

Figure 1.14: Typical CV responses for (a) a macroelectrode and (b) an ultramicroelectrode.

Once this peak in the current is reached, the current is limited by the rate of mass transport (i.e. diffusion) of reactant to the electrode surface. The fall in current that occurs is due to an increase in the depth of the depleted region next to the electrode and the inability of mass transfer to compete with the rate of electron transfer. Once the sweep reaches the switching potential, E_2, the potential reverses and the reaction proceeds in the opposite direction. The voltammogram takes the form of a mirror image of the forward sweep, but is shifted by 59/n mV, as dictated by the Nernst equation for the case of a completely reversible.[28] The scan rate plays an important role in the magnitude of the current. A typical voltammogram obtained for a macroelectrode is shown in Figure 1.14(*a*).

The cyclic voltammogram observed for a UME takes a different form to that described above for a traditional macroelectrode (Figure 1.14) for relatively low scan rate. Instead of the peaked reponse, the voltammogram takes a sigmoidal shape, as shown in Figure 1.14(*b*). A maximum value of the current is observed, and the voltammogram plateaus at this value. This is termed the diffusion-limited current. This value of the current is maintained due to efficient replenishment of reactant at the electrode surface, resulting from rapid hemispherical diffusion to the UME. This bulk steady-state limiting current, for a disc UME can be theoretically calculated from Equation 1.10.[25,60]

$$i = KnaFDc^* \qquad (1.10)$$

where n is the number of electrons transferred in the electrode reaction, a is the electrode radius, c^* is the bulk concentration of the electroactive species and K is a geometrydependent constant (K is 4 for a disc UME or 2π for a hemispherical UME).

Comparison of theoretical and experimental currents gives a quick indication that the system is working correctly. The shape of the sigmoidal waveform can be used to verify the electrode properties, e.g. the diameter of the active metal, the shape of the UME and how well the wire is sealed to the glass; and can be used to judge how good an electrode is. Both potential and scan rate can be controlled through a potentiostat, which monitors the potential applied to the tip and records the current response.

A galvanostat can also be employed to generate currents at the tip of the UME. This operates by varying the potential to maintain and monitor a controlled current. In principle, a galvanostat can act as a potentiostat and vice-versa, depending on how the cell is connected, however some models of potentiostat already have this feature built-in.[25-26]

1.2.6. Scanning electrochemical microscopy (SECM)

SECM is a powerful scanned probe technique for quantitative investigations of interfacial physicochemical processes, in a wide variety of areas, as considered in several recent reviews.[61-62] In the simplest terms, SECM involves the use of a mobile ultramicroelectrode (UME) probe, either amperometric or potentiometric, to investigate the activity and/or topography of an interface on a localized scale; typically resolution is on a micron length scale. It is capable of delivering a reagent to a surface with high rates of mass transport,[28,63] and is highly controlled[64-69] allowing the characterization of fast surface processes and the ability to study the chemical reactivity of analyte.[70-79] A comprehensive review of all these aspects can be found in Bard and Mirkin.[38]

SECM involves monitoring the current generated at a tip as it is scanned across or towards a sample.[80] The SECM tip is attached to a precise piezoelectric positioning system which allows the tip to be moved in the *x*, *y* or *z*-direction with submicron-scale precision.[40] Undoubtedly, the most crucial component of the SECM is the tip. A commonly used tip is based on an embedded disk-shaped geometry.[63] The tip typically consists of a disc UME surrounded by an insulating glass sheath. The quantity of glass surrounding the electrode can affect the current response obtained in certain cases. Because of this, the electrode is characterised by an *RG* value [8], *a*s defined in section 1.2.4. At *RG* values below 10, back diffusion increasingly influences the currents seen. Exceeding an *RG* of 10 tends to largely eliminate these effects. The UME is immersed into a liquid phase and then placed close to another phase, which could be solid, liquid or gas. A potential is applied to the UME as it is scanned across or moved towards the interface of interest. The current response of the UME can give a great deal of information about the topography and the chemical reactivity of the surface.[27]

The advantages of SECM are that it is typically a non-invasive, non-destructive technique. It is well suited to small volumes where reactions can be detected directly and it allows the study of interfacial kinetic processes due to the high rates of mass transport achievable. It has high spatial resolution, versatility and selectivity. It is well known for chemical mapping and is used to investigate surface topography.[81-82] As examples, the technique has been applied to air/water interfaces to study gas permeation,[83] liquid/liquid interfaces,[61,84-90] liquid/solid interfaces,[68,91] single crystal,[65-67,92-93] and porous membranes.[94-95]

Chapter 4 and 5 outlines some further examples of SECM applications applicable to the work herein, in the fields of dissolution processes, kinetics and proton dispersion at many interfaces. Several modes of SECM have been developed to allow the local chemical properties of interfaces to be investigated. The mode of SECM most relevant to this work is the feedback mode.[96] There are basically two forms: negative feedback and positive feedback.[63] In this work, SECM is employed in the feedback mode to obtain approach curves to the surface of interest in order to determine UME-surface separation distance (chapters 4 and 5).

1.2.6.1 Negative Feedback

Negative feedback, where a UME approaches an insulating substrate, is shown in Figure 1.15(a). A potential is applied to the UME in order to reduce electroactive species O (present in solution) to species R at a diffusion limited rate, which generate a current, i_{∞}, at the tip electrode. As the tip approaches an insulating (inert) substrate, the hemispherical diffusion to the tip becomes hindered, and as such the current generated

begins to decrease in magnitude. This drop in current occurs at distances $d < 10a$. This is known as negative feedback.

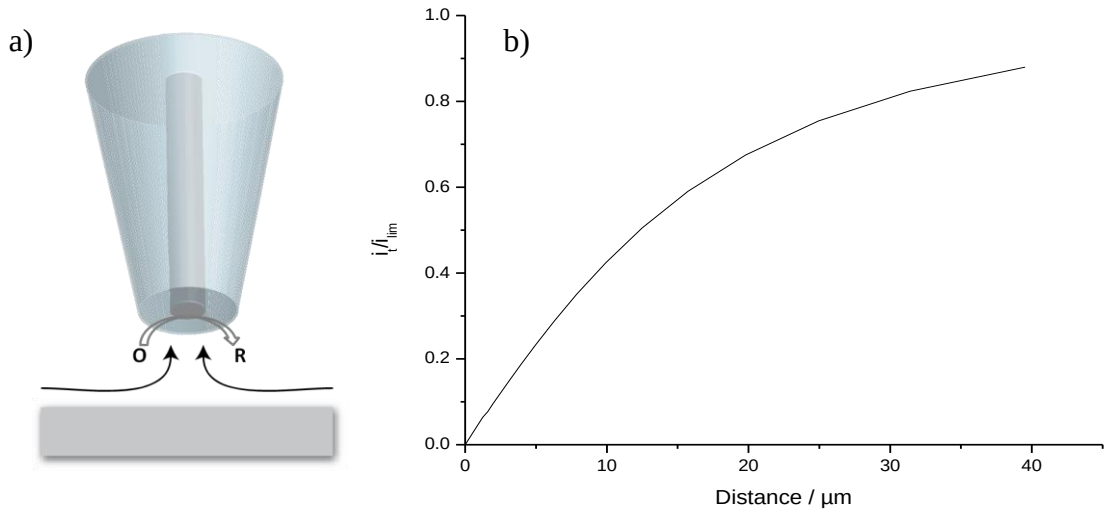

Figure1.15: (a) Schematic of negative feedback, for an UME near an insulating substrate and (b) Theoretical approach curve for a 25 µm diameter UME with an RG of 10, depicting negative feedback.

It is possible to plot curves showing i_t/i_∞ vs d, where i_t is the current at the tip, i_t/i_∞ is the normalised current, and d is the distance between the electrode and the surface. These are known as approach curves. Theoretical approach curves may be constructed using the tables of Kwak and Bard[96] and experimental data compared to them. A typical curve is shown in Figure 1.15 (b) for a 25 µm electrode with an RG of 10. This depicts a perfectly flat UME approaching an ideal insulator. As the electrode touches the surface, the flux of species is completely hindered and no current flows. However, in practice this is difficult to achieve and so a current of less than 10% of bulk at touch is considered sufficient (indicated by a point of inflection), i.e. the electrode and substrate are sufficiently well aligned and the UME is well polished.

1.2.6.2. Positive Feedback

Positive feedback[63,96] occurs when the UME approaches a conducting substrate as shown in Figure 1.16 (a). In this situation, when the UME reaches a certain tip-surface separation, species R which has been generated at the tip is oxidised back to species O at the surface. This leads to an increasing concentration of species O being provided for reduction at the UME, and, as such, an increase in the current is seen. This is termed positive feedback. Theoretical approach curves for conducting surfaces can be plotted in a similar manner to those for insulating surfaces, discussed in section 2.2.1. The theoretical approach curve for a conducting substrate is given in Figure 1.16 (b) using a 25 µm diameter electrode with an RG of 10.

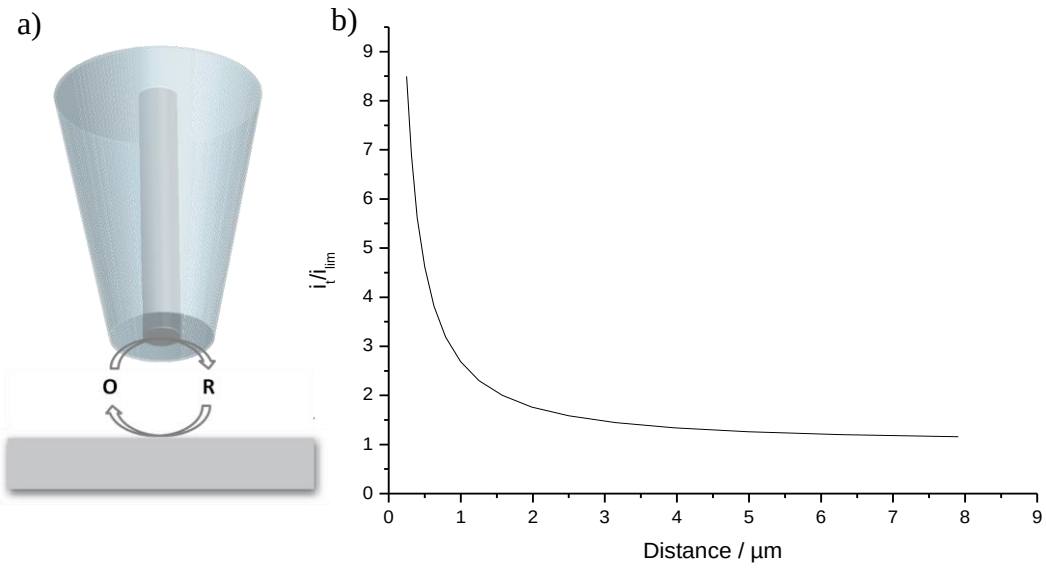

Figure 1.16: (a) Schematic of positive feedback near a conducting substrate (b) Theoretical approach curve for a 25 µm diameter UME displaying positive feedback.

1.4. Finite Element Modelling (FEM)

The simulation in this thesis was performed using the commercially available software package, Comsol Multiphysics. This environment provides the user with all of the

advantages of FEM, but a detailed knowledge of the complex mathematics behind this method is not required. It combines these advantages with an extremely user-friendly interface that enables simple construction of complex geometries (in one-, two- or three-dimensions) and simple definition of governing equations and boundary conditions. Many equations commonly used in the fields of engineering and physics are already built into the program (including diffusion, diffusion-convection and the Navier-Stokes equations for incompressible flow which are of relevance to this thesis) but a generic module is also present so that user defined equations can also be solved.

Essentially, COMSOL Multiphysics provides approximate solutions to differential equations using the finite element method. This technique uses a computer to solve a defined set of equations (i.e. Fick's second law of diffusion and Navier-Stokes equations for the work within this thesis) within a user defined domain. In 2D simulations applied herein the problem is broken down into a set of triangular elements, known as a mesh, which is used to approximate the domain being simulated (Figure 1.17(a)).[97-98] Generating a mesh the chosen equations are calculated at the corners of each triangular element. For areas where the result is likely to change the most, for example a concentration gradient near an electrode surface, the mesh density is increased (Figure 1.17 (b)). This can be either defined by the user or using an algorithm to focus on areas of greatest change in a property (e.g. fluid velocity and concentration). Both mesh refinement approaches allow simulations to be run efficiently without sacrificing accuracy.[99-101]

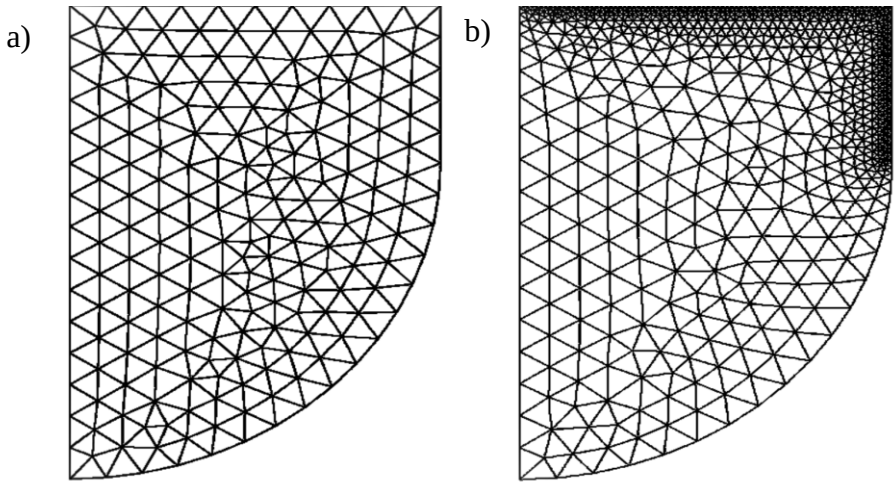

Figure 1.17: (a) An example of a simple triangular mesh used for FEM and (b) the same domain where the mesh is finer at two edges.

Many systems have used finite element models as a means of aiding understanding of reactions processes, mechanisms or kinetics.[97,102-103] In electrochemistry, FEM has been used both through self-written programs and commercially available software packages. In fact, one of the seminal SECM theory paper by Kwak and Bard,[63] describing the positive and negative feedback response expected during an approach curve measurement, relied on finite element simulations. With particular relevance to SECM, models have been used to monitor transport through porous membranes, [104] to understand catalytic processes,[105] and to develop tip positioning.[106] Other researchers have used models to visualise the permeability of films[107] and to define kinetics.[108-109]

For the work in this thesis and resulting publications, finite element models were created by a colleague, Dr. Martin Edwards to produce the theoretical characteristics and a fundamental understanding of the reaction processes occurring in solution. This aspect is described in more detail in Chapter 4 where boundary conditions and experimental parameters are also defined.

1.5. Aims of this Thesis

The overarching aim of thesis is to develop a new understanding of physiochemical processes and diffusion problems at interfaces by developing new techniques and exploring wider applications, which can be summarised as follows:

The main goal is to demonstrate the use of fluorescence CLSM coupled with electrochemical techniques and finite element modelling (through Comsol Multiphysics) in the quantification of concentration and pH gradients produced upon reaction at an electrode. The concentration gradient determined directly, while pH gradients are visualised through the addition of trace amounts of fluorescein, a dye that has a pH-dependent fluorescent signal. The fluorescence profile is predicted through simulation of the underlying mass transport equations.

Following on from the introduction, the apparatus used, experimental details and set-up are given in Chapter 2. This includes sample preparation, device microfabrication and characterisation, CLSM imaging experiments and the additional techniques used.

Chapter 3 includes a discussion on combining electrochemical investigation with fluorescence confocal laser scanning microscopy (CLSM) imaging to assess the usability of CNTs mats as disc OT-UMEs. Simultaneous monitoring of redox reactions is possible by using fluorophore the luminescent properties of which depend on either solution pH or fluorophore redox state. In this study a ST-cut quartz substrate is employed to grow ultrathin films of interconnected CNTs at optimised cCVD conditions utilising ethanol and cobalt as carbon feedstock and catalyst, respectively.

Chapter 4 describes the use of confocal microscopy coupled with SECM as a powerful technique for direct visualisation of acid-induced reaction processes and as a method for assessing the effectiveness of protective barriers on the enamel surface. It details the effect that fluoride and zinc treated enamel have on the prevention of acid attack. This found that Zn^{2+} treatment provides a much better barrier to prevent acid attack on enamel.

Chapter 5 investigates the lateral diffusion of protons through bilayer lipid membranes by the CLSM-SECM technique. A UME is brought close to the bilayer and galvanostatic water oxidation is induced, generating a proton gradient near the membrane. The transport of protons is observed as a pH change alongside bilayer. The effect of different ionisable head group, such as acidic distearoyl phosphatidylglycerol 1,2-ditetradecanoyl-sn-glycero-3-phospho-(1'-rac-glycerol) (DSPG) and zwitterionic phosphatidyl choline (EPC), on this process is also studied since it is thought that such negatively charged lipids facilitate proton lateral diffusion.

Finally, chapter 6 summarises the conclusions drawn and indicates potential directions for future study.

1.6. References

(1) Amos, W. B.; White, J. G. *Biology of the Cell* **2003**, *95*, 335.
(2) Cox, G. *Materials today* **2002**, 34.
(3) C.J.R.Sheppard; D.M.Shotton *Confocal laser scanning microscopy*; First ed.; BIOS Scientific Publisher Limited: Untied States of America, 1997.
(4) Minsky, M. **1957**, *7*, 107
(5) Webb, R. H. *Reports on Progress in Physics* **1996**, *59*, 427.
(6) Halbhuber, K. J.; Konig, K. *Annals of Anatomy-Anatomischer Anzeiger* **2003**, *185*, 1.
(7) Nathan S. Claxton, T. J. F., and Michael W. Davidson.
(8) Rudd, N. C., The University of Warwick, 2007.
(9) Amatore, C.; Chovin, A.; Garrigue, P.; Servant, L.; Sojic, N.; Szunerits, S.; Thouint, L. *Analytical Chemistry* **2004**, *76*, 7202.
(10) Foldes-Papp, Z.; Demel, U.; Tilz, G. P. *International Immunopharmacology* **2003**, *3*, 1715.
(11) Carlsson, K.; Danielsson, P. E.; Lenz, R.; Liljeborg, A.; Majlof, L.; Aslund, N. *Optics Letters* **1985**, *10*, 53.
(12) Navratil, M.; Mabbott, G. A.; Arriaga, E. A. *Analytical Chemistry* **2006**, *78*, 4005.
(13) Fiedler, S.; Hagedom, R.; Schnelle, T.; Richter, E.; Wagner, B.; Fuhr, G. *Analytical Chemistry* **1995**, *67*, 820.
(14) Amatore, C.; Bonhomme, F.; Bruneel, J. L.; Servant, L.; Thouin, L. *Journal of Electroanalytical Chemistry* **2000**, *484*, 1.
(15) Rudd, N. C.; Cannan, S.; Bitziou, E.; Ciani, L.; Whitworth, A. L.; Unwin, P. R. *Analytical Chemistry* **2005**, *77*, 6205.
(16) Grime, J. M. A.; Edwards, M. A.; Rudd, N. C.; Unwin, P. R. *Proceedings of the National Academy of Sciences of the United States of America* **2008**, *105*, 14277.
(17) Cannan, S.; Macklam, I. D.; Unwin, P. R. *Electrochemistry Communications* **2002**, *4*, 886.
(18) Lichtman, J. W.; Conchello, J. A. *Nature Methods* **2005**, *2*, 910.
(19) Haugland, R. P. *Molecular Probes Handbook of Fluorescent Probes and Research Products*,; 9 ed.; Molecular Probes: USA, 2002.
(20) Skoog, D. A. W., A. M.; Holler, F. J *Fundamentals of Analytical Chemistry*; 7th ed.; Saunders College Publishing: USA, 1996.
(21) Davidson, R. S. *Chemical Society Reviews* **1996**, *25*, 241.
(22) Sjoback, R.; Nygren, J.; Kubista, M. *Spectrochimica Acta Part A: Molecular and Biomolecular Spectroscopy* **1995**, *51*, L7.
(23) Marquardt, D. W. *the Society for Industrial and Applied Mathematics* **1936**, *11*, 431.
(24) Diehl, H.; Markuszewski, R. *Talanta* **1985**, *32*, 159.
(25) Bard, A. J.; Faulkner, L. R. *Electrochemical Methods: Fundamentals and Applications*; 2nd Edition ed.; John Wiley & Sons, Inc.: U.S.A., 2001.
(26) Brett, C. M. A.; Brett, A. M. O. *Electrochemistry: Principles, Methods, and Applications*; Oxford University Press: U.K., 2004.
(27) Fisher, A. C. *Electrode Dynamics* 4ed. Oxford UK, 2006.
(28) Bard, A. J.; Faulkner, L. R. *Electrochemical Methods. Fundamentals and Applications*; 2ed ed.; Wiley: India, 2006.
(29) C.M.A. Brett, A.M.O. Brett *Electrochemistry: Principles, Methods and Applications*; Oxford University Press: Oxford, 2000, p. 74.

(30) Donea, J.; Huerta, A.; Ponthot, J.-P.; Rodriguez-Ferran, A. *Encyclopedia of Computational Mechanics, Chapter 14 - Arbitrary Lagrangian-Eulerian Methods*; Wiley and Sons, Ltd, 2004; Vol. 1.
(31) Macpherson, J. V.; Simjee, N.; Unwin, P. R. *Electrochimica Acta* **2001**, *47*, 29.
(32) Zoski, C. G. *Electroanalysis* **2002**, *14*, 1041.
(33) Heinze, J. *Angewandte Chemie-International Edition in English* **1993**, *32*, 1268.
(34) Wightman, R. M. *Science* **1988**, *240*, 415.
(35) Fleischmann, M.; Pons, S. *Journal of Electroanalytical Chemistry* **1989**, *261*, 301.
(36) Penner, R. M.; Lewis, N. S. *Chemistry & Industry* **1991**, 788.
(37) Forster, R. J. *Chemical Society Reviews* **1994**, *23*, 289.
(38) Bard, A. J.; Mirkin, M. V. *Scanning Electrochemical Microscopy* New York, 2001.
(39) Kwak, J.; Bard, A. J. *Analytical Chemistry* **1989**, *61*, 1794.
(40) Bard, A. J.; Fan, F. R. F.; Kwak, J.; Lev, O. *Analytical Chemistry* **1989**, *61*, 132.
(41) Unwin, P. R. B., A. J., Stratmann, M., Eds., In *In Encyclopedia of Electrochemistry*; Wiley -VCH Weinheim: Germany, 2003; Vol. 3.
(42) R.M. Wightman *Science* **1988**, *240*, 415.
(43) R.M. Wightman, D.O. Wipf *Electroanalytical Chemistry: A Series of Advances*; A.J. Bard (Ed.), Marcel Dekker: New York, 1989; Vol. 15.
(44) Belal, F.; Anderson, J. L. *Analyst* **1985**, *110*, 1493.
(45) Ciszkowska, M.; Stojek, Z. *Journal of Electroanalytical Chemistry* **1985**, *191*, 101.
(46) K.R. Wehmeyer, M.R. Deakin, R.M. Wightman *Analytical Chemistry* **1985**, *57*, 1913.
(47) T.V. Shea, A.J. Bard *Analytical Chemistry* **1987**, *59*, 524.
(48) K.R. Wehmeyer, M.R. Deakin, R.M. Wightman *Analytical Chemistry* **1985**, *57*, 1989.
(49) M. Antonietta Baldo, S. Daniele, M. Corbetta, G.A. Mazzocchin *Electroanalysis* **1995**, *7*, 980.
(50) D.R. MacFarlane, D.K.Y. Wong *Journal of Electroanalytical Chemistry* **1985**, *185*, 197.
(51) M. Fleischmann, S. Bandyopadyhay, S. Pons *Journal of Physical Chemistry* **1985**, *89*, 5537.
(52) J.L. Ponchon, R. Cespuglio, F. Gonon, M. Jouvet, J.F. Pujol *Analytical Chemistry* **1979**, *51*, 1483.
(53) M.A. Dayton, J.C. Brown, K.J. Stutts, R.M. Wightman *Analytical Chemistry* **1980**, *52*, 946.
(54) Wightman, R. M. *Analytical Chemistry* **1981**, *53*, 1125.
(55) Woolaston, W. H. *Philos. Trans. R. Soc. London.* **1801**, *91*, 427.
(56) **Bindra, P.**; **Brown, A. P.**; **Fleischmann, M.**; **Pletcher, D.** *Journal of Electroanalytical Chemistry* **1975**, *58*, 31.
(57) Bond, A. M.; Fleischmann, M.; Robinson, J. *Journal of Electroanalytical Chemistry* **1984**, *180*, 257.
(58) Linge, H. G.; Nancolla.Gh *Calcified Tissue Research* **1973**, *12*, 193.
(59) Pletcher, D.; Sotiropoulos, S. *Journal of Electroanalytical Chemistry* **1993**, *356*, 109.
(60) Saito, Y. *Rev. Polarogr.* **1968**, *15*, 177.
(61) Barker, A. L.; Gonsalves, M.; Macpherson, J. V.; Slevin, C. J.; Unwin, P. R. *Analytica Chimica Acta* **1999**, *385*, 223.

(62) Wittstock, G.; Burchardt, M.; Pust, S. E.; Shen, Y.; Zhao, C. *Angewandte Chemie-International Edition* **2007**, *46*, 1584.
(63) Kwak, J.; Bard, A. J. *Analytical Chemistry* **1989**, *61*, 1221.
(64) Macpherson, J., V; Unwin, P., R. *Journal of the Chemical Society Faraday Transactions* **1993**, *89*, 1883.
(65) Macpherson, J. V.; Unwin, P. R. *Journal of Physical Chemistry* **1994**, *98*, 1704.
(66) Macpherson, J. V.; Unwin, P. R. *Journal of Physical Chemistry* **1995**, *99*, 3338.
(67) Unwin, P. R.; Macpherson, J. V. *Chemical Society Reviews* **1995**, *24*, 109.
(68) Macpherson, J. V.; Unwin, P. R. *Journal of Physical Chemistry* **1995**, *99*, 14824.
(69) Unwin, P. R.; Macpherson, J. V.; Martin, R. D.; McConville, C. F. *Electrochemical Society* **2000**, *99*, 104.
(70) Amemiya, S.; Bard, A. J.; Fan, F.-R. F.; Mirkin, M.; Unwin, P. R. *Analytical Chemistry* **2008**, *1*, 95.
(71) Barker, A. L.; Gonsalves, M.; Macpherson, J. V.; Slevin, C. J.; Unwin, P. R. *Analytica Chimica Acta* **1999**, *385*, 223.
(72) Wittstock, G.; Burchardt, M.; Pust, S.; Shen, Y.; Zhao, C. *Angewandte Chemie International Edition* **2007**, 1584.
(73) Bard, A. J.; Fan, F. R. F.; Pierce, D. T.; Unwin, P. R.; Wipf, D. O.; Zhou, F. M. *Science* **1991**, *254*, 68.
(74) Bard, A. J.; Unwin, P. R.; Wipf, D. O.; Zhou, F. M. *Aip Conference Proceedings* **1992**, *241*, 235.
(75) Unwin, P. R.; Bard, A. J. *Journal of Physical Chemistry* **1992**, 5035.
(76) Mirkin, M. V. *Mikrochim. Acta.* **1999**, *130*, 127.
(77) Mirkin, M. V.; Horrocks, B. R. *Analytical Chemistry Acta.* **2000**, *406*, 119.
(78) Barker, A. L.; Unwin, P. R. *Journal of Physical Chemistry* **2001**, *105*, 12019.
(79) Barker, A. L.; Unwin, P. R.; Zhang, J. *Electrochemistry Communications* **2001**, *3*, 372.
(80) Schulte, A.; Schuhmann, W. *Angewandte Chemie-International Edition* **2007**, *46*, 8760.
(81) Wipf, D. O.; Michael, A. C.; Wightman, R. M. *Journal of Electroanalytical Chemistry* **1989**, 15.
(82) Kwak, J.; Bard, A. J. *Anal. Chem.* **1989**, *61*, 1221.
(83) Ciani, I.; Burt, D. P.; Daniele, S.; Unwin, P. R. *Journal of Physical Chemistry B* **2004**, *108*, 3801.
(84) Zhang, J.; Slevin, C. J.; Unwin, P. R. *Chemical Communications* **1999**, 1501.
(85) Barker, A. L.; Unwin, P. R. *J. Phys. Chem.* **2001**, *105*, 12019.
(86) Barker, A. L.; Unwin, P. R.; Zhang, J. *Electrochem. Comm.* **2001**, *3*, 372.
(87) Barker, A. L.; Macpherson, J. V.; Slevin, C. J.; Unwin, P. R. *Journal of Physical Chemistry B* **1998**, *102*, 1586.
(88) Barker, A. L.; Unwin, P. R.; Amemiya, S.; Zhou, J. F.; Bard, A. J. *Journal of Physical Chemistry B* **1999**, *103*, 7260.
(89) Strutwolf, J.; Zhang, J.; Barker, A. L.; Unwin, P. R. *Physical Chemistry Chemical Physics* **2001**, *3*, 5553.
(90) Cannan, S.; Zhang, J.; Grunfeld, F.; Unwin, P. R. *Langmuir* **2004**, *20*, 701.
(91) Slevin, C. J.; Macpherson, J. V.; Unwin, P. R. *Journal of Physical Chemistry B* **1997**, *101*, 10851.
(92) Macpherson, J. V.; Unwin, P. R. *Progress in Reaction Kinetics and Mechanism* **1995**, *20*, 185.
(93) Macpherson, J. V.; Unwin, P. R. *Journal of Physical Chemistry* **1996**, *100*, 19475.
(94) Scott, E. R.; White, H. S.; Phipps, J. B. *Analytical Chemistry* **1993**, *65*, 1537.

(95) Scott, E. R.; White, H. S.; Phipps, J. B. *Journal of Membrane Science* **1991**, *58*, 71.
(96) Kwak, J.; Bard, A. J. *Anal. Chem.* **1989**, *61*, 1221.
(97) Huebner, K. J.; Thornton, E. A. *The Finite Element Method for Engineers*; 2nd ed. ed.; Wiley-Interscience: New York, 1982.
(98) Zimmerman, W. B. J. *Process Modelling and Simulation with Finite Element Methods*; World Scientific: : London, 2005.
(99) Melville, J. L.; Coles, B. A.; Compton, R. G.; Simjee, N.; Macpherson, J. V.; Unwin, P. R. *Journal of Physical Chemistry B* **2003**, *107*, 379.
(100) Melville, J. L.; Simjee, N.; Unwin, P. R.; Coles, B. A.; Compton, R. G. *Journal of Physical Chemistry B* **2002**, *106*, 10424.
(101) Klymenko, O. V.; Gavaghan, D. J.; Harriman, K. E.; Compton, R. G. *Journal of Electroanalytical Chemistry* **2002**, *531*, 25.
(102) Rao, S. S. *The Finite Element Method in Engineering*; Pergamagon Press: New York, 1982.
(103) Feldberg, S. *In Electrochemistry*; Marcel Dekker: New York, 1972; Vol. Vol. 2.
(104) McKelvey, K.; Snowden, M. E.; Peruffo, M.; Unwin, P. R. *Analytical Chemistry* **2011**, *83*, 6447.
(105) Cannan, S.; Cervera, J.; Steliaros, R. J.; Bitziou, E.; Whitworth, A. L.; Unwin, P. R. *Physical Chemistry Chemical Physics* **2011**, *13*, 5403.
(106) Edwards, M. A.; Whitworth, A. L.; Unwin, P. R. *Analytical Chemistry* **2011**, *83*, 1977.
(107) Cornut, R.; Lefrou, C. *Journal of Electroanalytical Chemistry* **2008**, *623*, 197.
(108) Burchardt, M.; Trauble, M.; Wittstock, G. *Analytical Chemistry* **2009**, *81*, 4857.
(109) McGeouch, C.-A.; Edwards, M. A.; Mbogoro, M. M.; Parkinson, C.; Unwin, P. R. *Analytical Chemistry* **2010**, *82*, 9322.

Experimental Methods

2.1. Sample Preparation

Enamel Sample Preparation

Buccal cuts of bovine enamel were provided by GSK (originating from Biohuz, UK) as discs of approximately 6.5 cm in diameter and 0.5 cm thick. The samples were halved using an open Stanley knife blade (Stanley, USA, no. 1992) to reduce number of samples needed and minimise the heterogeneity in samples. This also enabled studies of untreated and treated enamel from the same source. The samples were polished on microcloths (Struers,UK – grade MD-Dura) with 0.25 µm diamond paste (Struers A/S, Denmark), rinsed in Milli-Q reagent water and mounted (after drying) onto glass capillaries (1.6 mm external diameter) using Araldite (Huntsman International LLC, UK). Samples to be treated were placed in their respective solutions (NaF or $ZnCl_2$) at the desired concentration typically 1000 ppm, for 2 minutes and rinsed with reagent water ca. 5 seconds, and fitted in the purpose built confocal microscopy cell (vide infra) filled with fluorescein solution as described later.

Polyelectrolyte Ultrathin Films Modification

For studies of a positively charged poly-L-Lysine (PLL) modified surface, the surface of glass cover slip (glass bottom dishes, WillCo-dish®KIT, 0.15 or 0.17 mm thick) was coated with PLL (Sigma-Aldrich) using the drop coating method. The surface was

cleaned by exposure to oxygen plasma at 100 W for 3 min before mounting on the modified CLSM stage, as described in section 2.3. The film was deposited from 1mg ml^{-1} solutions for adsorption times of 20 min. A known volume, typically 500 µl of the solution was dropped into the cell using a plastic pipette. After adsorption of the polymer, the surface were rinsed with ultra-pure Milli-Q water and dried in an air flow. This yielded an intrinsically positively charged surface. The same procedure was used to deposit a poly-L-glutamic acid (PGA) (1 mg/ml PGA, Sigma-Aldrish) film onto a previously deposited PLL film to achieve a negatively charged surface.

Supported Lipid Bilayer (SLB) surface modification

Bilayers were formed using the vesicle fusion method (VFM); see section 5.1.1 for more details. For the preparation of vesicle solutions, desired amounts of lipids egg phosphatidyl choline (EPC); distearoyl phosphatidylglycerol 1,2-ditetradecanoyl-sn-glycero-3-phospho-(1'-rac-glycerol) (DSPG); from Avanti Polar Lipids were dissolved in chloroform, at a concentration of 1 mg/ml. Part of a stock solution of small unilamellar vesicles (SUV) was dried in a nitrogen stream and vacuum desiccated for at least 4 h to remove the chloroform. The lipids were then resuspended in the buffer to a concentration of 1 mg ml^{-1}, sonicated for 2 min to ensure complete resuspension, frozen and thawed five times in dry CO_2 and warm water, respectively, before finally being extruded 15 times through 100 nm polycarbonate membranes (GC Technology) using liposofat.

To form SLBs on the glass cover slip, the surface was cleaned by exposure to oxygen plasma at 100 W for 3 min before mounting on the modified CLSM stage, as described in section 2.3. 1 mg/ml solution of a pure EPC and a mixture EPC: DSPG in phosphate

buffer was prepared in two molar ratios 80:20 and 60:40. A known volume, typically 500 µl, of SUV solution was dropped into the cell using a plastic pipette containing buffer solution. After allowing 128 minutes to elapse the resulting SLB was rinsed with the buffer. The cell was filled gradually using a plastic pipette with 1 mL of the solution to be used for imaging, typically consisting of 8 µM fluorescein and 0.1 M potassium nitrate.

Monitoring SLB Formation

Bilayer formation was observed using ScanAsyst-atomic force microscopy (SA-AFM) in real time, with assistance from Mr. Mike O'Connell and Mr. Binoy Nadappuram. The glass cover slip (glass bottom dishes, WillCo-dish®KIT) were cleaned by exposure to oxygen plasma at 100 W for 3 min. 500 µl of 1 mg ml^{-1} EPC-DSPG SUV solution was pipetted into the buffer solution onto the glass microscope slides and kept under solution for SA-AFM imaging. Topographical images of the surface were obtained using a Veeco Bruker Bioscope Catalyst AFM typically at a resolution of 256 by 256 pixels at 2 Hz, using the different stiffness cantilevers of SNL-type silicon nitride probes with nominal force constant, k, of 0.32 and 0.58 N m^{-1}, respectively, and a resonant frequency, f_0, of 40−75 kHz.

2.2. Device Microfabrication and Characterisation

2.2.1. Pt Ultramicroelectrode (UME) Fabrication and Characterisation

The procedure used for UME fabrication was based on the method developed by Wightman and Bard *et al*..[1]. A disk-shaped tip was made by heat sealing a 1.5 cm length of 25 µm diameter metal microscopic wire (platinum) into a borosilicate glass capillary tube (GC200-10, 2.0 mm inner diameter, 1.16 mm outer diameter, Harvard Apparatus

Ltd. Kent, U.K.). The end was then polished to expose an embedded disk. A coarse carbimet paper disc (240 grit, Buehler, Coventry) was used to polish the tip of the glass capillary to expose the end of the wire. A finer grade (600 grit, Buehler, Coventry) and then waterproof silicon carbide paper (SIC Paper #4000, Struers) were used to smooth the surface of the tip, to obtain a flat surface. Further polishing with impregnated diamond polishing pads (Buehler, Coventry) of sequentially finer grades (from 9 μm to 0.1 μm) was carried out using a custom built polishing wheel.

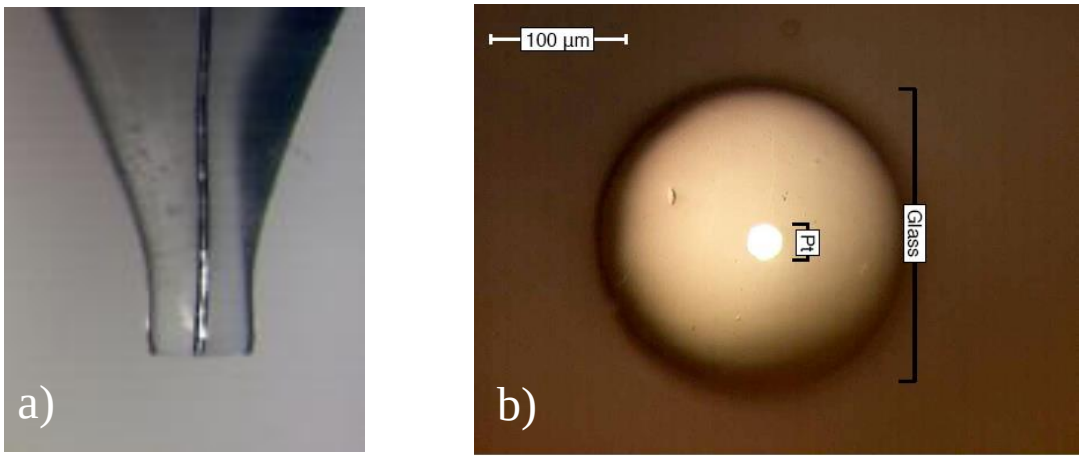

Figure 2.1: Conventional light microscope image of the tip of a 25 μm diameter platinum disc UME: (a) from the side; (b) the electrode surface.

An insulator radius of 10 times larger than the electrode radius (the *RG* ratio) is usually desirable.[2] The sides of the electrode were 'coned' (polished) using waterproof silicon carbide paper to give the electrode the required *RG* value. Optical microscope images of UMEs obtained in this way are given in Figure 2.1. Silver loaded epoxy adhesive (RS) was used to coat the end of a piece of tinned copper wire (RS), which was then inserted into the capillary, ensuring that it was in contact with the Pt wire. This was left to dry before testing the connection.

Characterisation of Pt-UME

UMEs prepared as described above were firstly checked by slow sweep voltammetry in an aqueous solution of 1 mM ferrocenylmethyltrimethylammonium (FcTMA) and 0.1 M KNO_3 over the potential range 0.1-0.5 V (vs Ag/AgCl). FcTMA undergoes a simple one-electrode reaction. A good electrode showed plateau steady-state limiting current and little hysteresis of the forward and reverse waves (see Figure 2.2).

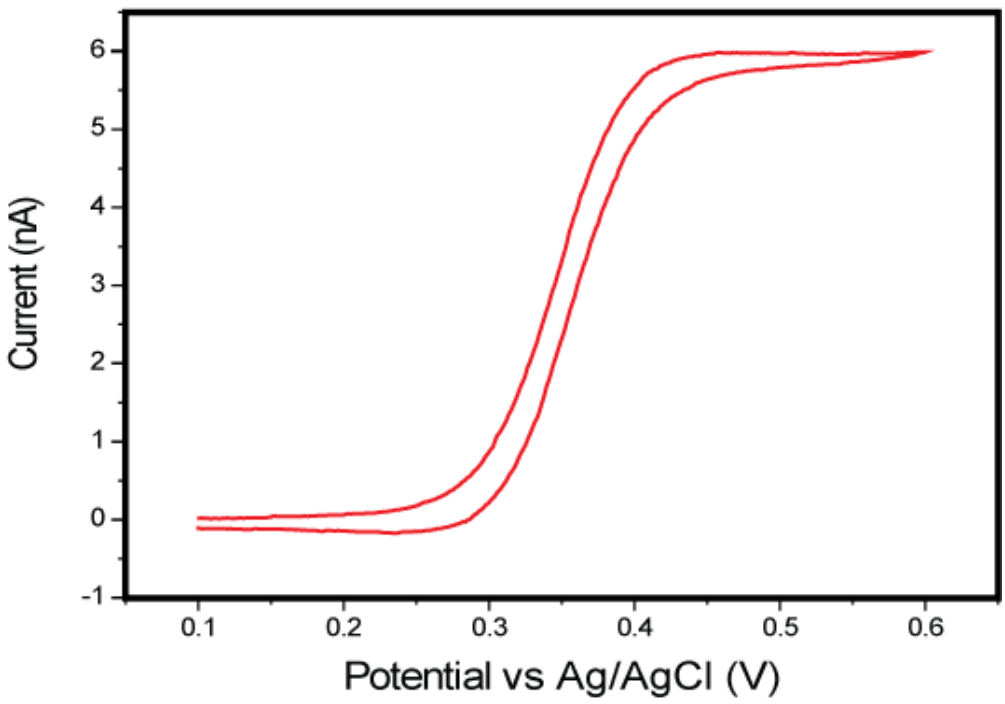

Figure 2.2: Cyclic voltammogram for the oxidation of 1 mM FcTMA at a 25-µm diameter Pt UME. The scan rate was 10 mV s^{-1}.

Additionally, SECM approach curves towards an inert glass substrate were recorded to further assess the quality and flatness of the UME surface. In Figure 2.3, i_{lim} is the steady-state current in the bulk solution and i_t the current response of the redox reaction at the tip. The data obtained bore out the theory of Bard et al[2-3] (Figure 2.3). In practice, the alignment of UME and the substrate used are never perfectly flat, therefore, it was acceptable for a UME to touch the surface at a value of no more than 10 % of the

normalised current. Experimentally, when the UME touches a surface there was a point of inflection, or plateau in the experimental curve as shown in Figure 2.3. Before each set of measurements, the electrode was polished using slurry of alumina particles (0.05 µm gamma alumina Micropolish, Buehler, Coventry) in water on a polishing cloth to ensure that the surface was clean and smooth.

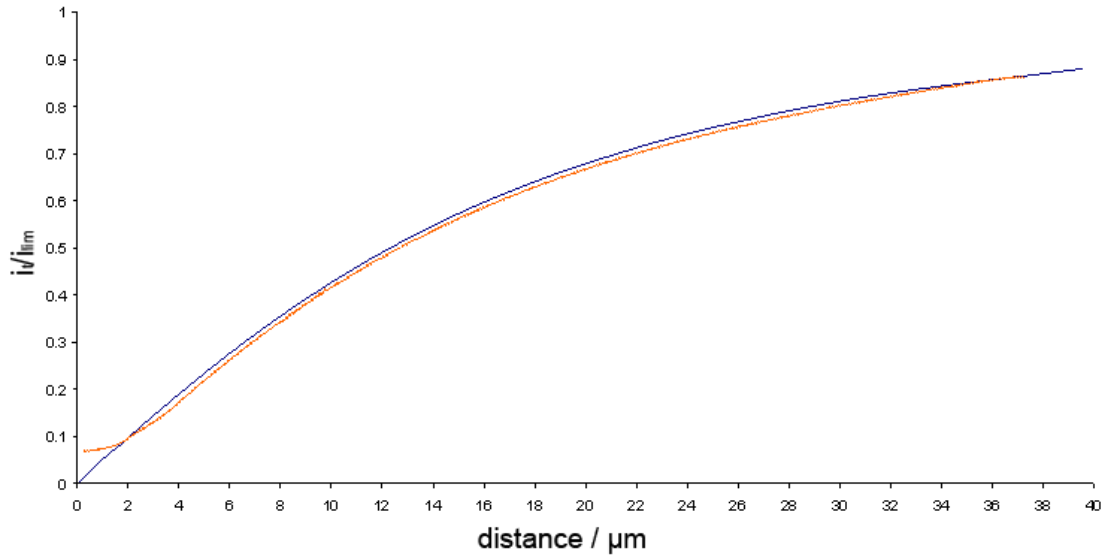

Figure 2.3: SECM experimental approach curve (red line) and the theory (blue line) towards inert glass substrate performed in 0.1 M KNO_3.

2.2.2. Optically Transparent Single-Walled Carbon Nanotubes Ultramicroelectrodes (OT-SWNTs- UMEs): Fabrication and Characterisation

cCVD Growth of CNT networks

Carbon nanotube ultrathin mats were grown (by Dr. Agnieszka Rutkowska)[4] directly on single crystal quartz substrates (Hoffman Materials, Inc., 3 in. diameter, angle cut: 42°45′, 500 µm thick, double side polish) using catalysed chemical vapour deposition technique (as illustrated in Figure 2.4). 1.2 cm x 1.2 cm quartz samples were cleaned with acetone and isopropanol and blown dry with nitrogen, followed by sputter

depositing of a thin film of cobalt for 20 seconds (Quorum Technologies sputter coater). The samples were placed on a quartz boat with a Si/SiO_2 support on top (IDB Technologies Ltd., 0.5 mm thick, n-type Si, 300 nm thermally grown SiO_2) in the centre of a 1 in. quartz tube of the cCVD oven (Lindberg Blue).[5] The magnitude of the hydrogen flow and the growth temperature were optimised by AFM examination of the NP size. For the conditions stated above, a NP size of ~ 4-8 nm was found to be optimal for SWNT growth. Methane was introduced at 875 °C for a period of time and the flow rate adjusted so that the total flow rate of gases was kept at 2000 sccm.

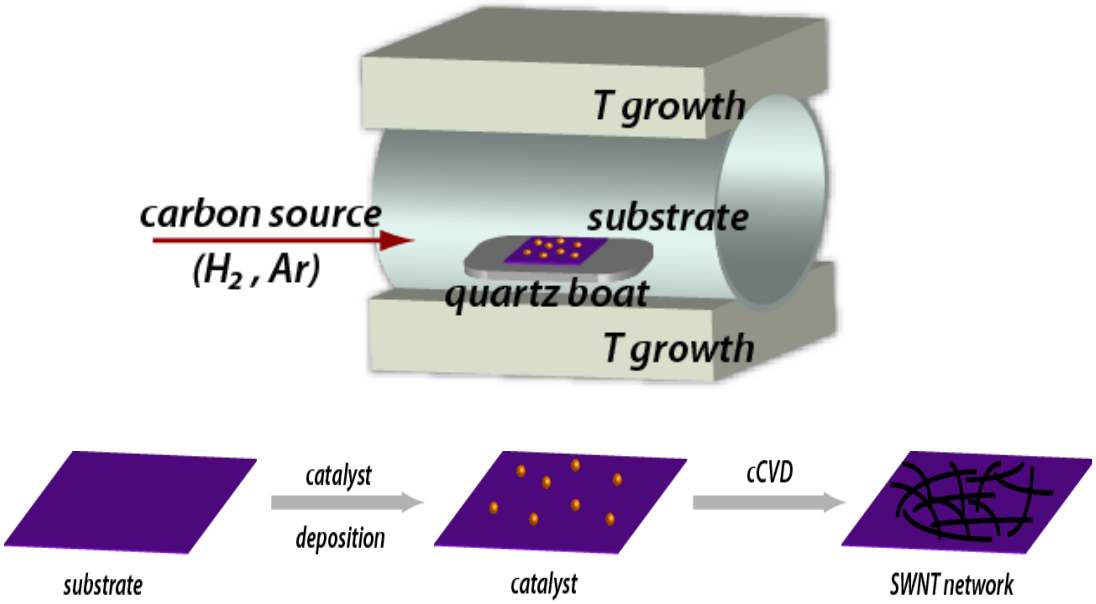

Figure 2.4: Schematic illustration the procedure for growing single-walled carbon nanotubes ultrathin mats using catalysed chemical vapour deposition technique.

The samples were heated from room temperature to 700 ºC within 10 min and up to 850 ºC within next 10 min in the presence of hydrogen flow (150 sccm). The system was stabilized for 5 min and ethanol was supplied by introducing a flow of argon (850 sccm) through an ethanol bubbler held at 0 ºC. The flow of argon was terminated after 10 min and the system was allowed to cool down to room temperature under a hydrogen flow (150 sccm).

Preparation of SWNTs-OT-UMEs

The gold contacts were evaporated onto SWNTs-functionalised quartz samples through a shadow mask (Figure 2.5) using a Moorfield Minilab Conversion evaporator/sputterer unit at a deposition rate of 0.05Å/s and 1.5 Å/s for chromium (Testbourne Ltd.) and gold (Goodfellow), respectively. Chromium with a thickness of 10 nm was used as a support layer to increase the adhesion of gold (thickness 120 nm) to the substrate. Disc UMEs were prepared by UV photolithographical exposure using Suss mask aligner (MJB4 mask aligner, Suss MicroTec, 4 seconds UV exposure time) and S1818 positive photoresist (Rohm and Haas Electronic Materials) with an adhesive microprimer support layer (Rohm and Haas Electronic Materials). The conditions for spin coating substrates with primer and S1818 are listed in Table 2.1. Spin coating samples with primer was followed by ca. 1.5 µm of primer + S1818 photoresist deposition. Samples coated with S1818 were soft baked at 115 °C for 1 min to ensure good adhesion of the layers to the substrate before the photolithographical step.

Table 2.1: Conditions for spin coating samples with microprime primer and S1818 positive photoresist.

Chemical Rotation	Acceleration time (s)	Spin time (s)	speed (rpm)	Deceleration time (s)
Primer	0.1	40	3000	0.1
S1818	0.1	40	3000	0.1

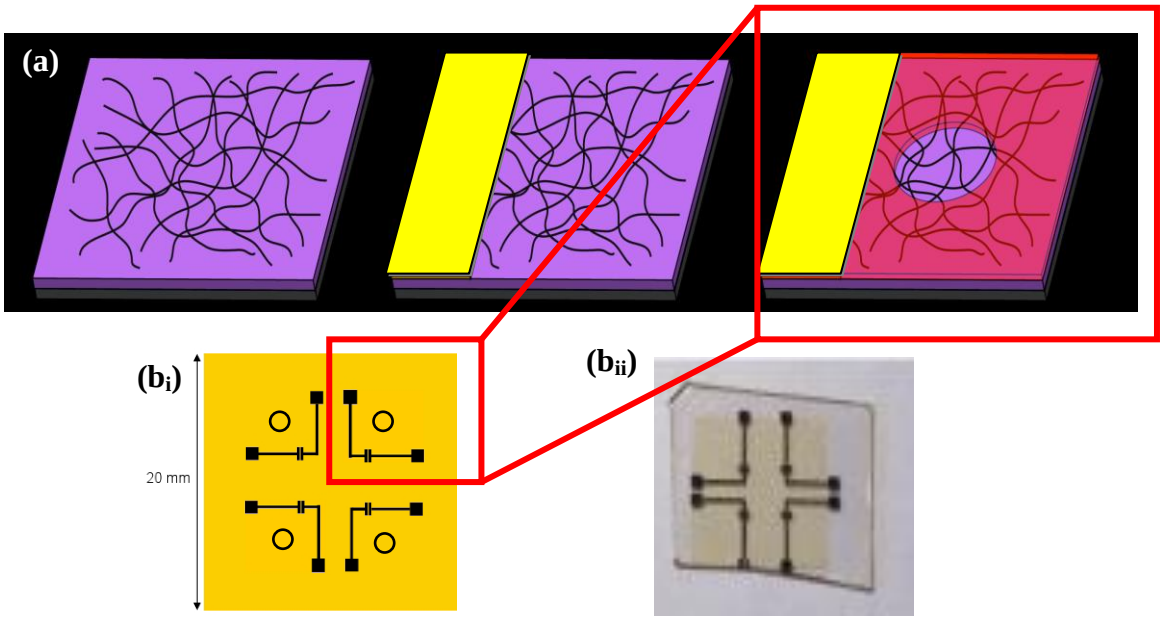

Figure 2.5: (a) Schematic of the procedure used for fabricating SWNTs network disk UMEs, (b_i) Geometry of the shadow mask used for microfabrication of Cr/Au bands for disk UME experiments, (b_{ii}) Photographs of CNT device used in electrochemical experiments.

50µm disc electrodes were aligned to the geometry of the Au bands so that the edge of the UME was at a sufficient distance away from the Cr/Au layer, ensuring it could not compromise the pristine integrity. The pattern was developed by soaking in MF 319 developer solution (Rohm and Haas Electronic Materials) for 1 min, followed by rinsing with Milli-Q water and blowing dry with nitrogen flow.

Characterisation of SWNTs network mat

Several techniques were employed throughout this thesis to investigate the results of cCVD growth and to characterize the SWNTs networks and devices obtained. Details of these techniques are given in this section. The transparency of SWNTs mats on ST-cut quartz was measured using a standard UV-Vis spectrophotometer (Jasco V-660).

Atomic Force Microscopy

Atomic force microscopy (AFM EnviroScopeTM, Veeco) was used to verify the density of SWNTs films. AFM was conducted in tapping mode. The principle of operation is based on a feedback loop, where the cantilever is brought to resonance and is oscillated close to the sample so that the tip periodically touches the surface. This imaging mode is used for soft samples, as lateral tip-surface forces are minimized. Most importantly for the work herein is that it prevents dragging of SWNTs on the surface. AFM tips employed (RFESP, Multi75 metrology probes, Veeco Probes, U.S.A.) had resonant frequencies of 75-100 kHz and force constants of 1.5-6 N m^{-1}.

Micro-Raman Spectroscopy

Micro-Raman spectra of SWNTs networks were recorded using a Renishaw inVia microscope incorporated with Leica microscope and CCD detector. SWNTs peaks were calibrated against at 521 cm^{-1}. A 514.5 nm (2.41 eV energy) excitation wavelength of an Ar laser, at 10 mW power, focused in a ~ 10 μm^2 spot size, was used in the experiments to determine the quality of the grown SWNTs and to confirm the presence of uniform and defect-free SWNTs. Raman spectroscopy is a broadly used technique for quantitative analysis of SWNTs structural and physical properties. The presence of SWNTs was confirmed with micro-Raman spectroscopy (Figure 2.6) by characteristic G^+ (1594:5 cm^{-1}) and G^- (1576:6 cm^{-1}) peaks and the small distortion (D) peak at 1342:6 cm^{-1}.

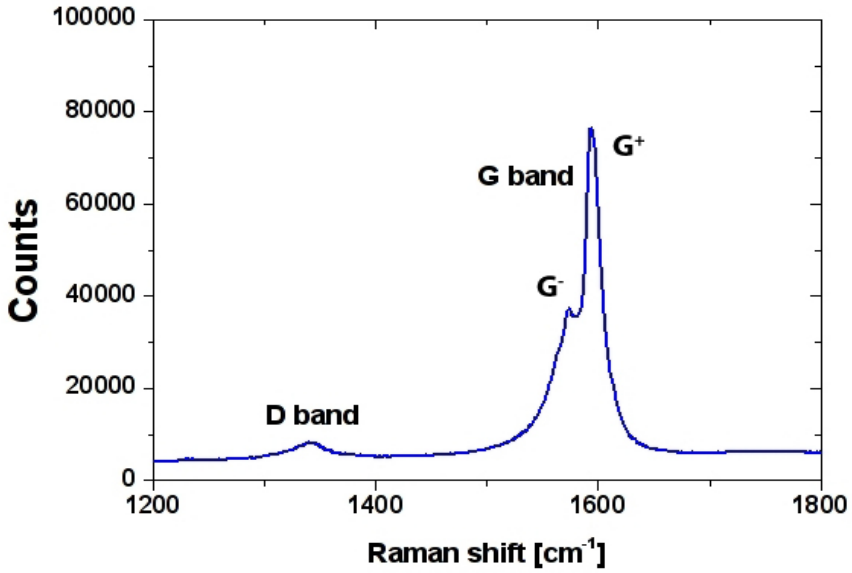

Figure 2.6: Micro-Raman spectrum of SWNTs ultrathin mats grown on single crystal quartz.

2.3. CLSM Experiments

Confocal fluorescence imaging was performed using a Leica TCS SP5X Supercontinuum laser scanning confocal microscope mounted on a Leica DMI6000 CS inverted microscope. Typically, the following parameters were used: 488 nm excitation wavelength (Ar laser), detector window 480-570 nm, and 8000 Hz line scanning frequency. Well-defined proton flux for high resolution time (ms) was achieved via a built in-house galvanostat. A two electrode galvanosatic arrangement with Pt reference electrode (Ag/AgCl RE), and an UME (25 μm diameter Pt disc, with a glass surround of 250 μm diameter, fabricated as described in section 2.1) as working electrode was used. Anodic current was applied at the working electrode to produce a proton flux via water oxidation and images of the resulting fluorescence profiles captured.

$$H_2O \longrightarrow 2H^+ + \tfrac{1}{2}\, O_2 + 2e^- \qquad (2.1)$$

2.3.1. Visualisation of Electrochemical Processes at OT-SWNTs-UMEs

The experimental setup for simultaneous electrochemical (CompactStat, Ivium Technologies) and fluorescence confocal imaging (Inverted Leica TCS SP5X Supercontinuum Confocal) studies is shown schematically in Figure 2.7. The CNT electrode device was placed on an aluminium sample holder (designed in house of size of 7.5 cm x 2.5 cm x 0.5 cm) with 1 cm x 1 cm hole in the centre for CLSM imaging. A drop of the solution of interest was cast on top of a 50 μm diameter OT-UME. Figure 2.5 illustrates the case for aqueous $Ru(bpy)_3^{2+}$ of various concentrations: 1 mM, 5 mM and 10 mM, in 0.1 M sodium chloride. The electrochemistry of redox reactions of $Ru(bpy)_3^{2+}$ and fluorescein were visualized using an inverted microscope (Leica DMI6000 CS) in fluorescence mode, using 488 nm argon laser.

The gain and the offset of the channel were adjusted according to the experiment: (i) low initial intensity below and at the electrode surface, (ii) high initial intensity at the electrode surface and low below its plane, for fluorescein and $Ru(bpy)_3^{2+}$ experiments, respectively. The surface was defined prior to any electrochemical experiment by scanning across the sample (in the z direction: *xyz* scan) in the bright field mode and collecting z-stacks (*z-volume* = 150 μm, *z-step* = 2 μm) from below and above the initially focused UME.

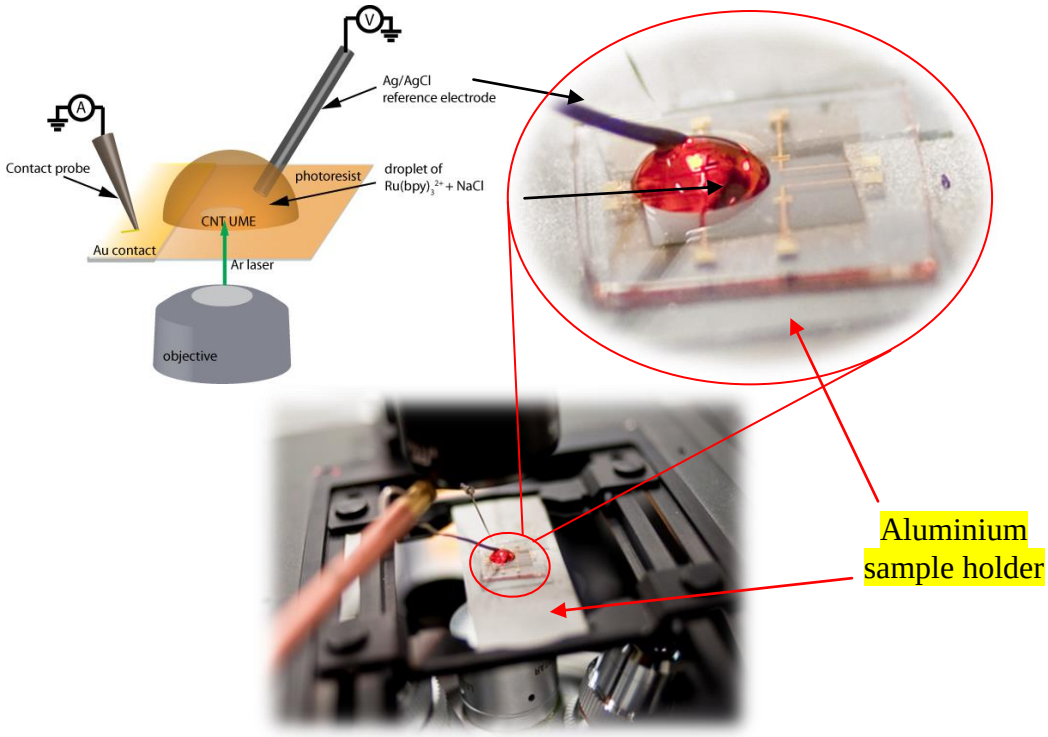

Figure 2.7: Schematic representation of the experimental setup used for visualising OT-SWNTs-UMEs.

Cyclic voltammetry (CVs) of the redox couples was performed by cyclic sweep of the potential in an appropriate range versus Ag/AgCl reference electrode at a scan rate of 10 mV/s and 5 mV/s for fluorescein and $Ru(bpy)_3^{2+}$, respectively. The process was monitored (*xyt* scan, t = 180 s) with CLSM fluorescence and brightfield modes. To synchronise the light intensity measured by CLSM and the potential applied, the CLSM was triggered by the potentiostat (Leica Trigger Unit connected with the Ivium CompactStat by DAQPad-6015, National Instruments). This enabled the CLSM light intensity signal adjacent to the electrode plane to be related to the potential change driving the redox reaction.

The choice of the microscope objectives was limited to 10x magnification and 0.3 aperture and 11.0 mm free working distance (HC PL FLUOTAR type for DRY

immersion) due the relatively large thickness of quartz used for the fabrication of the transparent electrode (0.5 mm) and the sample holder (0.5 mm). The resolution of this type of objective is shown in Table 2.1, as supplied by the manufacturer.

Table 2.1: Resolution characteristics of HC PL FLUOTAR objective with 10x magnification, 0.3 NA and 11.0 mm free working distance. The scan field size (*xy*) of this objective was 1500 µm × 1500 µm.

Resolution	(nm) at wavelength of 488 nm
Resolution (*xy*)	651
Resolution Air (*z*)	4768
Resolution Water (*z*)	6407
Resolution Oil (*z*)	7335

Chronoampermoetry (CA) experiments were conducted for $Ru(bpy)_3^{2+}$ oxidation and the oxygen reduction (ORR) by stepping the potential from 0 V, where no reaction occurred, to the diffusion-limited potential of 1.1 V and -1.0 V (vs. Ag/AgCl RE), respectively, for a time of 60 s. The potential step was recorded simultaneously in time and space, i.e., 2D and 3D concentration profiles at the steady state were obtained by *xyt* scanning (time interval as above) at the electrode surface, and *xyz* scanning through the electrode surface (with *z*-volume and z-step specified below for each experiment), respectively. In *xyz* scans, the intensity of the lowest *z*-stack was set to 0. Intensity values recorded during *xyt* and *xyz* scans were normalised by the initial intensity value at time = 0 s (I_t=0), and intensity maximum value, respectively, for both $Ru(bpy)_3^{2+}$ oxidation and the ORR. Current values (i) were normalised by i_{lim}.

2.3.2. Visualisation of Proton Diffusion at Active and Modified Surfaces

Enamel-UME Tip Positioning

The UME tip was positioned through a hole on the side of CLSM cell, perpendicular at fixed distance from the enamel surface via *xyz*-micrometers and a piezoelectric positioner (E-660, Physik Instrumente, *xyz* translation) (Figure 2.9) for optimum displacement. It consisted of a 25 µm *z*-axis piezo (Model P253.20, Physik Instrumente, Germany) attached to an *x*-*y* stage (Physik Instrumente, Germany). Three axis movements were possible by virtue of *x*, *y* and *z* axis micrometers to allow the position of the electrode to be adjusted so that it approached the appropriate region of the surface of interest.

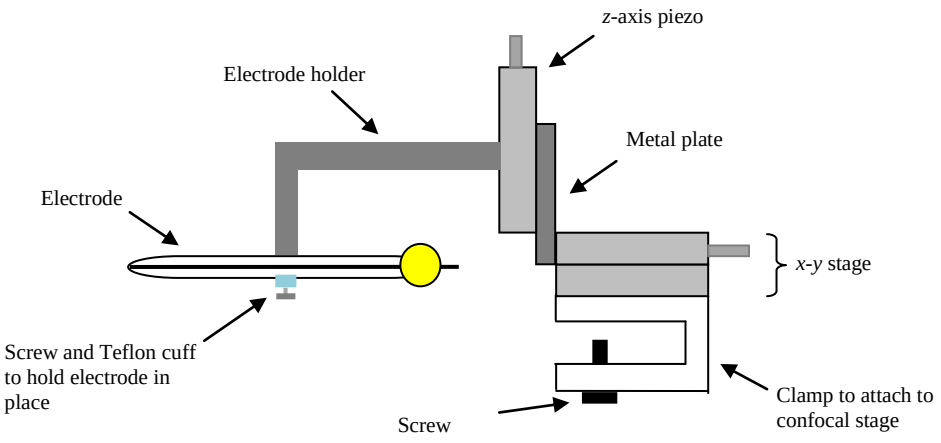

Figure 2.9: Schematic diagram of the clamp system developed for use with the confocal microscope.

The glass stage plate of the confocal microscope (held on a vibrationally isolated support) was removed to allow manipulation the attachment of the cell to a metal plate that fitted into the hole left by the glass stage plate so that the centre of the cell, where the glass window (Glass microscope slides) was located in the centre of CLSM

objective. The clamp system, shown in Figure 2.9, was attached to the right hand side of the stage and the electrode placed in the holder to be aligned above objective lens (10× magnification, HC PL FLUOTAR type for DRY immersion) and close to enamel surface.

Galvanostatic Proton Generation

Production of proton via water oxidation was achieved using a home built galvanostat. Ii utilised a triangle wave pulse generator (Colburn Electronics, Coventry, UK) as its potential source. A range of currents were applied to the probe tip, from 1 pA to 100 nA to obtain different proton flux. This galvanostat was tested and showed a rise time of c.a. 1 ms for current of 20 nA (Figure 2.10). To ensure time correlation between CLSM and electrochemical application, the galvanostat was triggered by the CLSM (Leica Trigger Unit connected with a galvanostat DAQpad-6015, National Instruments).

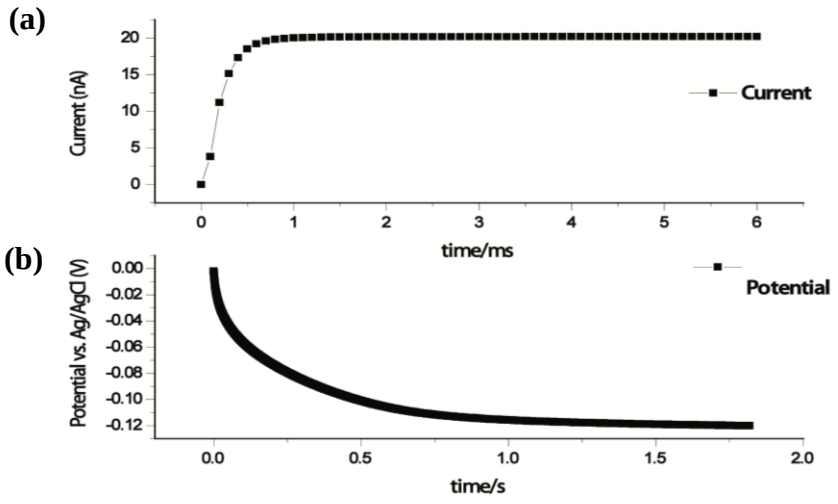

Figure 2.10: (a) Rise time for a current of 20 nA using homemade galvanostat and (b) corresponding change of the potential applied to the UME working electrode.

Visualisation of Enamel Dissolution

Figure 2.11 shows a schematic of the experimental set-up for visualisation of proton flux during enamel dissolution. A horizontal PTFE cell with two facing apertures, housing the ultra-micro electrode (UME) and the substrate holder, was fitted to the microscope stage. A cell (designed in house of size of 6 cm diameter) with 2 cm diameter hole in the centre equipped with a glass window on the bottom, allowed visualisation of the gap between the electrode tip surface and the enamel surface.

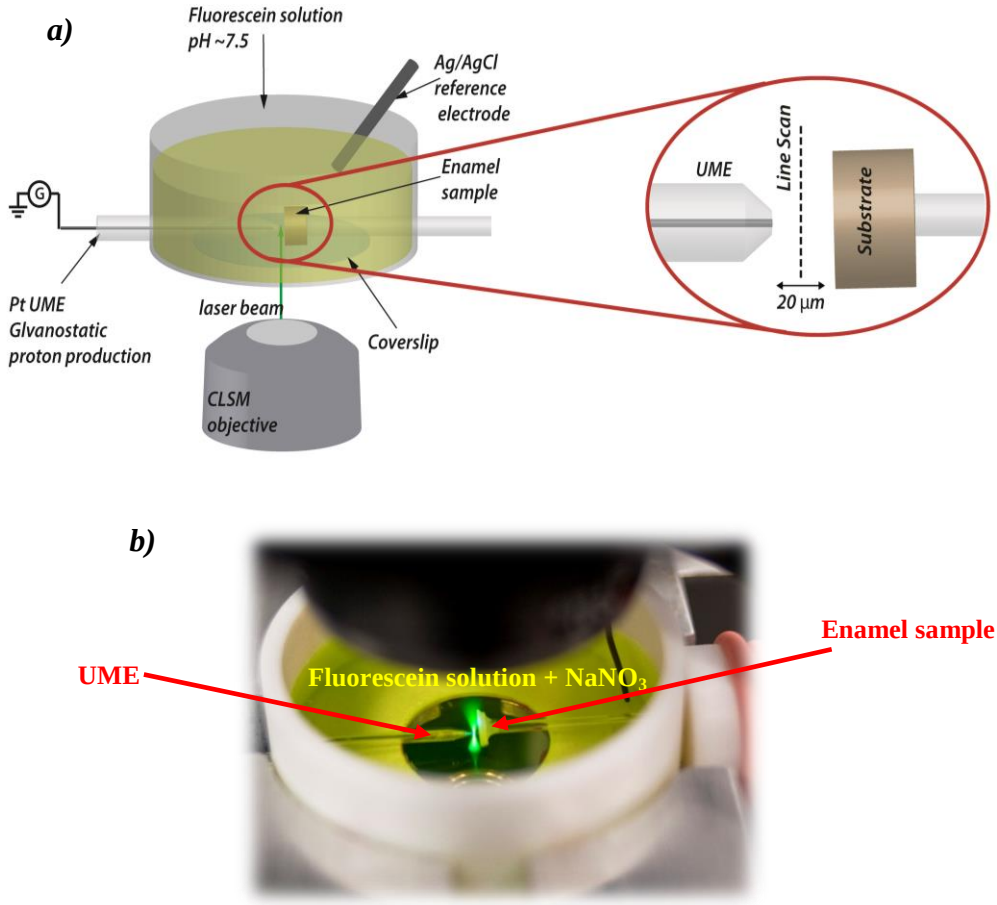

Figure 2.11: Describes the CLSM-SECM set-up where: (a) is a schematic detailing the components seen in (b); (b) is a photograph showing the UME and enamel sample inserted in the cell and immersed in solution.

CLSM visualization was performed by positioning the UME at a distance of 20 µm from the enamel surface. This distance allowed reaction products to escape rather than

accumulate in the gap between the UME and substrate. Time series images were produced by scanning in the *x-y* plane during application of currents of 10, 15 and 20 nA to the working electrode vs. Ag/AgCl for 5 seconds. The signal was line averaged over four lines to improve the signal to noise ratio and normalized at the maximum intensity. For higher time resolved experiments a transient *xyt* scan of the fluorescence intensity between the tip of the UME and the enamel surface was recorded by scanning a smaller area of 88 × 912 µm (with a 10x/0.3 HC PL Fluotar dry lens) between the electrode and the enamel surface with time (time interval between each image 70 ms, *t* = 5 s), as illustrated schematically in Figure 2.11(a), and the interface brought into focus. The gain and the offset of the channel were adjusted according to the experiment: (i) low initial intensity at the electrode and enamel surfaces, (ii) high initial intensity in solution inside the gap between the enamel and the electrode surface.

SECM Tip Positioning

The experimental setup for SECM tip positioning is shown in Figure 2.8. The UME tip as working electrode was mounted on a high-dynamic z-piezoelectric positioner (P-611.3S NanoCube), while the sample was mounted on an aluminium sample holder (designed in house of size of 20 cm x 10 cm x 2 cm) with 35 mm diameter hole in the centre for CLSM imaging. The entire assembly was installed in a Faraday cage on the *xyz* CLSM stage in Figure 2.8.

Tip and data acquisition were performed by using a FPGA card (NI.PCI-7852-R, National Instruments) with a LabVIEW 10 Development System written by Mr. Kim McKelvey. Prior to positioning the UME, a CV was recorded for oxygen reduction at a scan rate of 10 mV s^{-1}. The potential was swept from 0 V through to - 1 V and back

again, with the bulk limiting current typically attained at - 0.45 V. The limiting current was subsequently used to determine the tip-substrate distance using the hindered diffusion response.[6-7] Such approach curves provided a clear indication of the distance of closest approach of the tip to the surface.[6] Electrodes could be positioned at the surface within < 0.5 µm and were used to set a distance of 20 µm from the substrates.

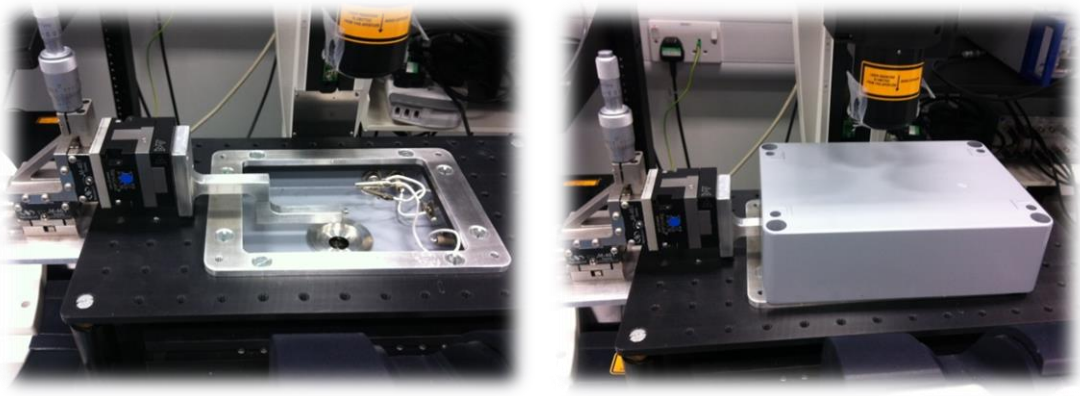

Figure 2.8: Experimental set up for SECM tip positioning and CLSM experiments.

Approach curve measurements employed a traditional SECM configuration which involved approaching the surface of interest from above using a 80 µm *z*-axis piezo (Model M-461, Newport) mounted on an *x*-*y* stage (Model M-461, Newport). Three axis movements were possible by virtue of *x*, *y* and *z* axis micrometers to allow the position of the electrode to be adjusted so that it approached the appropriate region of the surface. This involved positioning the electrode so that it lined up with the CLSM objective, by using the *x* and *y* micrometers. A potential of around -0.45 V (with respect to Ag/AgCl reference electrode was applied to the 25 µm platinum electrode (*RG* = 10) so that the oxygen reduction occurred at a diffusion-limited rate.

The electrode was then brought closer to the surface using the *z* micrometer. The current, monitored by a current follower system coupled to a triangular wave-pulse generator with a voltmeter displaying the current output, began to change when the electrode was within a distance of about 10 electrode radii from the substrate.[3] Approach curves for oxygen reduction (while the electrode was held a -0.45 V with respect to a silver/silver chloride reference electrode (Ag/AgCl RE) in fluorescein solution were obtained. Once the current was seen to alter, the *z*-axis piezo was used so that the distance moved by the electrode was accurately known. Once the tip-substrate distance had been set, the working electrode was connected to the galvanostat.

Visualization of Lateral Proton Diffusion at Modified Surfaces

A small dish (50 x 9 mm, WillCo-dishes) was used as the experimental cell with glass windows at the bottom of the dishes (0.15 or 0.17 mm thick). This was simply fixed to the microscope stage. The major advantage of this glass bottom is that the microscope light passes orthogonally through the glass bottom and there is no air-buffer between the warming-stage and the glass, which could seriously disrupt efforts to regulate the temperature of the cells in the dish.

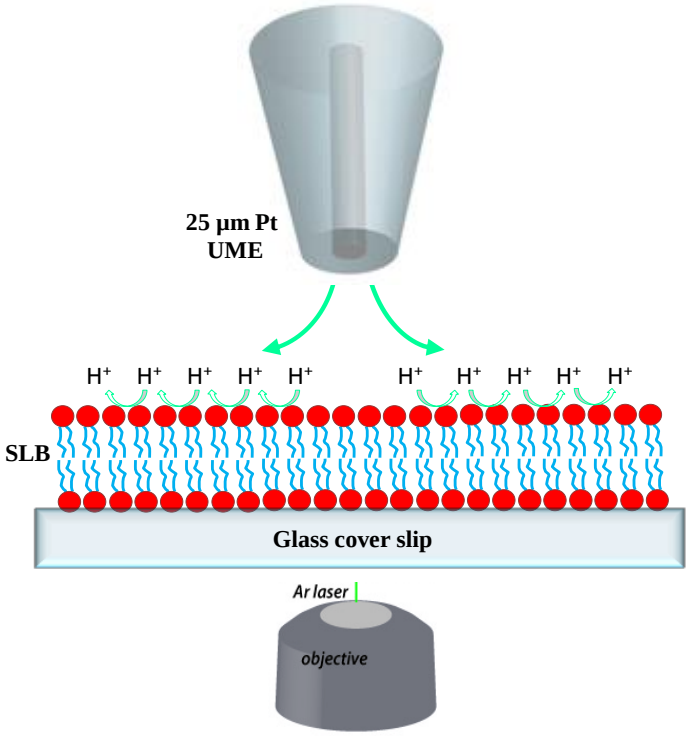

Figure 2.12: Schematic (not to scale) of experimental arrangement for studies of proton diffusion at a SLB.

This glass window on the bottom allowed visualisation proton dispersion at modified surfaces. CLSM imaging was carried out by positioning the UME at a distance of 20 µm from the modified surfaces and aligned above the objective lens (40× magnification, HCX PL FLUOTAR type for DRY) as shown in Figure 2.12. A line across the centre of the electrode surface was selected, as illustrated schematically in Figure 2.13, and the interface brought into focus. A series of 1024 scans were taken along the line, at 0.4 ms intervals, during which time a fixed current was applied to the working electrode vs. Pt as reference electrod to affect the oxidation of water. The signal was line averaged over sixteen lines to improve the signal to noise ratio.

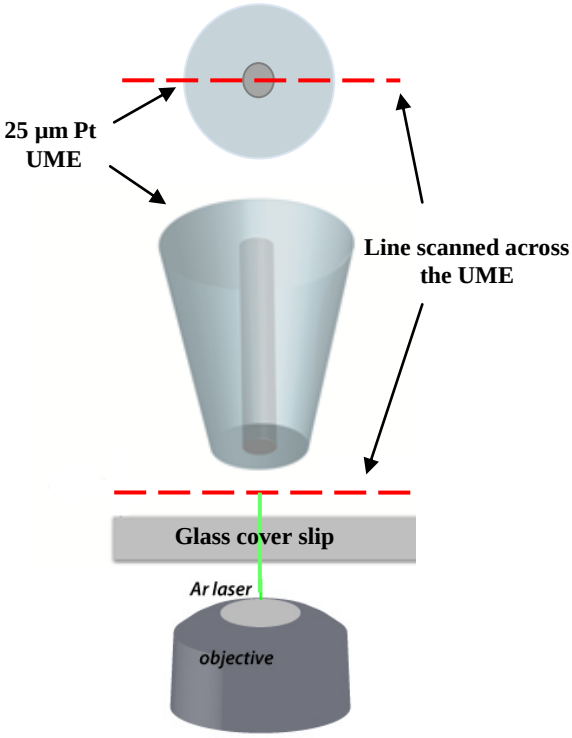

Figure 2.13: Schematic of experimental arrangement for studies of proton diffusion in a thin layer.

2.4 Additional Instrumentation

2.4.1. Inductively Coupled Plasma Mass Spectrometry (ICP-MS)

Experiments were performed by Dr. Lijiang Song, using ICP-MS (PerkinElmer 5300DV, equipped with S10 Autosampler) to determine the amount of zinc taken up by enamel treatment discussed in section 2.1. ICP was calibrated with $ZnCl_2$ solution 500 ppb, 200 ppb, 100ppb, 50 ppb, 20 ppb and 10 ppb. As the enamel discs have a diameter of 6.76 mm (equivalent to an area of 0.457 cm^2) a volume of 0.1 ml was chosen as this droplet covered the entire area of the sample without running off. The droplet was then pipetted off and diluted in 5ml for analysis.

2.4.2. Fluoride Ion Selective Electrode (FISE) Studies

To determine the amount of fluoride taken up by enamel, experiments were performed by Dr. Carrie-Anne McGeouch, using a solid state FISE (model ELIT 001N AgCl 58997), the working electrode (model Elit F^- 1230), and the reference electrode was Ag/AgCl. Samples to be analysed were treated with either 500 or 1000 ppm of NaF (0.026 and 0.053 molar equivalent) for two minutes then dissolved using 0.1 ml of 1 mM HNO_3, also for two minutes. The droplet was then pipetted off for FISE analysis. For calibration, a 0.1 M solution of NaF was prepared and subsequently diluted to give concentrations of 10^{-2}, 10^{-3} and 10^{-4} M.

2.5. Finite Element Modelling

Modeling was carried out using a commercial finite element method modelling package (COMSOL Multiphysics, version 3.2a), in conjunction with MATLABm (version 7.0, release 14). This was run on a Dell PC under Windows XP with an Intel Pentium 4 processor (2.50 GHz) and 1.5 GB of RAM.

2.6. Solution Preparation

All solutions were prepared using Milli-Q water (Millipore Corp, resistivity ≥ 18 MΩ cm), with the mass of material added determined with a four-figure analytical balance (Sartorius A2008). pH measurements were made using a pH meter (UltraBasic pH Meter, Denver Instruments), calibrated using buffer solutions at pH 4, 7 and 10 (“colourkey” buffer solutions, BDH).

Table 2.3: A detailed list of the chemicals used throughout this thesis, their grade and supplier.

CHEMICAL / SOLVENT	SUPPLIER & GRADE
Acetone	> 99 % Fisher Scientific
Propan-2-ol	> 99 % Fisher Scientific
Nitric Acid (HNO_3)	ARG Fisher Scientific
Potassium Hydroxide (KOH)	≥ 89.69 % Fisher Scientific
Potassium Nitrate (KNO_3)	> 99.995 % Sigma-Aldrich
Sodium Chloride (NaCl)	> 99.92 % Fisher
Sodium Fluoride (NaF)	> 99 % Aldrich
Tris(2,2′ bipyridine)ruthenium(II)	> 99 % Sigma Aldrich
Fluorescein	Sigma-Aldrich
$ZnCl_2$	> 99 % Sigma-Aldrich
(Ferrocenylmethyl)trimethylammonium iodide, FcTMA+I-	> 99 % Strem Chemicals
Argon gas	> 99 % BOC Gases
Egg phosphatidyl choline (EPC)	Avanti Polar Lipids
Distearoyl phosphatidylglycerol 1,2-ditetradecanoyl-sn-glycero-3-phospho-(1'-rac-glycerol) (DSPG),	Avanti Polar Lipids
Poly-*L*-Lysine (PLL)	> 99 % Sigma-Aldrish
Poly-*L*-glutamic acid (PGA)	> 99 % Sigma-Aldrish

2.7. References

(1) Demaille, C.; Brust, M.; Tsionsky, M.; Bard, A. J. *Analytical Chemistry* **1997**, *69*, 2323.
(2) Bard, A. J.; Fan, F. R. F.; Kwak, J.; Lev, O. *Analytical Chemistry* **1989**, *61*, 132.
(3) Kwak, J.; Bard, A. J. *Analytical Chemistry* **1989**, *61*, 1221.
(4) Rutkowska, A.; Bawazeer, T. M.; Macpherson, J. V.; Unwin, P. R. *Physical Chemistry Chemical Physics* **2011**, *13*, 5223.
(5) Rutkowska, A.; Walker, D.; Gorfman, S.; Thomas, P. A.; Macpherson, J. V. *Journal of Physical Chemistry C* **2009**, *113*, 17087.
(6) Kwak, J.; Bard, A. J. *Anal. Chem.* **1989**, *61*, 1221.
(7) Gonsalves, M.; Barker, A. L.; Macpherson, J. V.; Unwin, P. R.; O'Hare, D.; Winlove, C. *Biophys. J.* **2000**, 1578.

Visualisation of Electrochemical Processes at Optically Transparent Single-Walled Carbon Nanotube Ultramicroelectrodes (OT-SWNTs-UME)

Introduction

This chapter concerns the investigation of mass transport in microscale systems. A major focus is on Confocal Laser Scanning Microscopy (CLSM) as a means of visualising diffusion and reactions of fluorescently active species at optically transparent ultramicroelectrodes (OP-UMEs) comprising Carbon Nanotube (CNT) networks on quartz. The electrochemical activity of the UMEs is quantified with the temporal and spatial resolution in the millisecond and micrometer range, respectively. The methodology comprises of tracking the dynamic, reversible concentration profiles of electroactive and photoactive tris(2,2'-bipyridine)ruthenium(II) species in aqueous solutions during cyclic voltammetry experiments. Specifically a decrease of fluorescence intensity is recorded at and around the UME surface during the oxidation of luminescent $Ru(bpy)_3^{2+}$ *to non-luminescent* $Ru(bpy)_3^{3+}$*, followed by an increase of the intensity signal in the reverse scan direction as the oxidized* $Ru(bpy)_3^{3+}$ *is consumed at the electrode surface. A three dimensional map of the concentration gradients of* $Ru(bpy)_3^{2+}$ *is constructed by collecting sections of the object across the normal to the electrode plane in the steady state current regime. This configuration enables optical measurements of the solution, close to the electrode surface, without significant interference from absorption or scattering processes.*

3.1. Overview

Probing concentration profiles at electrode surfaces and other interfaces finds applications in many interfacial processes. A wide range of processes in biology (cellular and bacterial chemotaxis and synaptic transmission)[1-2] and chemistry (phase-transfer reactions,[3-4] corrosion,[5] crystal growth/dissolution and faradic currents)[6] are controlled by mass transport and thus by the concentration gradient[7-8] Consequently, a variety of analytical methods have been devised to monitor the development of such concentration profiles near an active surface. Visualisation of concentration gradients

near electrode surfaces is of interest as it provides details on the reaction mechanism, as well as the electrode activity and sensitivity to certain species involved in electrochemical processes.[9]

The current response at the electrode gives information on the concentration gradient directly adjacent to it, but complete concentration profiles over the whole diffusion layer give much more information. Because of this, much research, involving many different techniques, has been carried out into imaging various interfacial processes. The majority of reported approaches are devoted to adapting scanning electrochemical microscopy techniques[10-11] and the use of optical methods such as laser beam deflection,[12] absorption spectroscopy [13-14](UV-Vis, X ray, IR, EPR, Raman)[15-17], fluorescence microscopy[18-21] and scanning optical techniques (fluorescence confocal laser scanning microscopy[8,22] and confocal resonance Raman microspectroscopy[16-17,23]) to image concentration gradients at active surfaces.

Among the electrochemical techniques that have been used to investigate concentration profiles, both potentiometric and amperometric probes have been used at various interfaces.[1,24-28] For example potentiometric probes have been used to map the variation in the Nernst potential across diffusion layers.[25] In this study a 250 μm diameter platinum electrode was held at a fixed potential, chosen such that it induced the electrode reaction at a diffusion-limited rate, and the potential variation at a 5 μm diameter disc UME were measured as it approached the larger electrode. By applying the Nernst Equation, the concentration of the reactant and product (related by mass balance), assuming their diffusion coefficients are the same, were determined. Potentiometric probes also have been used by Amatore *et al.*[25] to determine the

concentration profile of ferrocyanide/ferricyanide and the tetracyanoquinodimethane (TCNQ) reduction reaction. However, despite their accuracy, potentiometric measurements usually can be performed only under equilibrium conditions preventing transient measurements.

Engstrom *et al.*[27-28] first demonstrated that an UME amperometry set up could be used to map concentration profiles adjacent to a large active surface, with micrometer spatial resolution, and millisecond time resolution. Using this method the concentration profile for intermediates of coupled solution reactions were obtained by altering the tip potential. Amperometric tips are generally preferred since absolute concentrations are obtained, instead of ratios of one species to another which are obtained with potentiometry. A similar concept has been used by Amatore *et al.*[26] to obtain transient concentration profiles of the same systems that had been studied potentiometrically (ferrocyanide/ferricyanide and the TCNQ reduction reaction).

Various studies have been carried out using scanning electrochemical microscopy (SECM) to determine many interfacial processes. Bard *et al.*[29] were the first to investigate sample surfaces with SECM. Unwin and co-workers used SECM extensively to directly observe reactions occurring at liquid/liquid, solid/liquid and liquid/gas interfaces.[4,30-33] All these electrochemical methods are very powerful as they provide spatial and temporal resolutions in the micrometer and millisecond range respectively, depending on the size of probe and technique used. SECM was reviewed in Chapter 1 section 1.3.6.

The combination of microscopic and spectroscopic techniques with electrochemical methods would constitute a very useful tool to investigate *in situ* the composition of the electrochemical diffusion layers. Various studies have been carried out using the absorption of electrogenerated species, as absorbance is directly proportional to concentration (Beer-Lambert law). Spectroelectrochemical techniques have been used to monitor multiple species, particularly if they absorb at different wavelength. This method provides better selectivity, sensitivity and resolution than those techniques involving refractive index measurement, allowing much more precise measurement of the concentration profile.[34] Spatially resolved spectroelectrochemistry has been used by McCreery and co-workers to investigate homogeneous electron transfer reactions with spatial resolution of less than 5 μm.[35]

Raman spectroscopy has also been used in order to examine concentration profiles as it allows precise chemical characterisation of the species present during an electrochemical reaction.[16-17] As the focal plane of the microscope is altered, the concentration at different distances from the electrode can be obtained since the intensity of the Raman signal is proportional to the concentration of the species. Confocal Raman microscopy allows more precise optical sectioning through a sample since only Raman spectra originating from the illuminated point in the sample plane of interest are detected. Thus, the out-of-focus contribution to the spectrum is minimised. Amatore *et al.* have used confocal resonance Raman microscopy to image the composition of a diffusion layer, focussed on investigating the effect of conproportionation reactions.[16-17,23]

Another method that has been used to map electrochemical activity is luminescence imaging.[36-37] With this technique the light emitted from a fluorescence reaction or electrogenerated chemiluminescence (ECL) is imaged. Engstrom and co-worker have extensively used this technique to visualize various interfacial processes. In ECL imaging, electrochemistry is used to generate a species at the electrode which reacts to produce light emitting species such as $Ru(bpy)_3^{2+}$ in the presence of $C_2O_2^-$. The ECL technique has been used to provide an image of the current density, illustrating the edge effect of highly oriented pyrolytic graphite (HOPG),[36-37] which was thought to be electrochemically active only on the edge[12], and locating sites of activity differences on composite electrodes.[36-37] However, there is a limited number of species that undergo electrochemiluminescence. Furthermore, the widespread application of this method is restricted by the complexity of some ECL reaction sequences.[18,20]

The use of fluorescence based methods as an alternative to ECL is most suitable as there are a wide range of substances that are themselves fluorescent or can react with an electrochemically-produced species to produce fluorescent molecules.[20] In electrochemistry,[9,19-21] so various attempts have used this process to establish concentration gradients (pH gradients). Besides, there are numerous reagents whose fluorescence is pH-dependent, such as quinine or Oregon green,[38] but the most common fluorescent acid-base indicator is fluorescein. It strongly emits at a wavelength of approximately 515 nm in basic solution, when it is excited at 470 nm. Engstrom *et al.* have applied the fluorescence technique to study different systems, including cathodic centers in Al/Cu corrosion cells,[18] local differences in the kinetics of composite electrodes,[19] and electrode activity for oxygen O_2 evolution.[18] Later, it was shown by Amatore[2] and co-workers, that real-time remote fluorescence imaging of two-

dimensional concentration profiles of Ru(II) reagent could be achieved using a multichannel fibre bundle. Recently, the fluorescence technique has been combined with SECM in order to observe the activity of a single molecule of enzyme adenosine triphosphate (ATP) synthase, which was labelled with a pH sensitive fluorophore, activated by the pH gradient across a membrane.[12]

Nevertheless, compared to conventional fluorescence microscopy, CLSM is superior in terms of image contrast, signal-to-noise ratio and spatial resolution. The use of fluorescence CLSM to monitor the concentration profile at an electrode surface during an electrochemical reaction was successfully introduced by Unwin[7-8,22] and co-workers. CLSM was used to image 3D pH gradients at and near to an electrode surface. The reduction of benzoquinone in unbuffered solution produced a local pH increase that caused fluorescein to become deprotonated and hence fluoresce. This technique has been used to image the diffusion field at UMEs of various geometries, so providing information on local mass transfer.[7,22] In particular, the technique has been used to visualise proton gradients at an electrode during water oxidation and reduction.[7,22] In order to obtain quantitative data from the fluorescence CLSM images, the finite element method has been used to simulate mass transport. Fluorescence microscopy had been used previously to identify active sites on a variety of electrode surfaces,[9,19-20] but without the advantage of *z*-axis scanning through the solution, normal to the electrode surface.

More recent works have been reported by Unwin[8] and co-workers for quantitative measurements of permeation through model biological membranes by using a combination of laser confocal microscopy (CLSM) and micro-electrochemistry. The

technique uses an ultramicroelectrode (UME) placed close to one side of the membrane boundary (roughly 20 microns away) to generate protons in the presence of weak acids anions and a trace amount of fluorescein (pH-sensitive fluorophore). The generation of protons by galvanostatic water oxidation reduced the local solution pH and thus produced a dark domain, which could be imaged using CLSM. This approach was supported by finite element modelling (FEM) to report the trend of decreasing permeation coefficient as the weak acid molecules increase in size.[8]

Fluorescein, a widely used fluorophore, exhibits a pH-sensitive fluorescence signal. In acidic media the fluorescence is weak, but as the pH rises the intensity of the fluorescence increases (Figure 1.3). By altering the pH electrochemically, the corresponding changes in light intensity provide information on pH gradients and diffusion close to the electrode surface. A simple way to locally change the pH in an aqueous solution is by oxidising or reducing the water to produce protons or hydroxide ions, respectively, as shown in Equations 3.1 and 3.2.

$$H_2O \longrightarrow 2H^+ + \tfrac{1}{2} O_2 + 2e^- \quad (3.1)$$

$$2H_2O + 2e^- \longrightarrow H_2 + 2OH^- \quad (3.2)$$

or by reducing dissolved oxygen, Equation 3.3 summarises the reaction in acidic medium.[39]

$$O_2 + 2H^+ + 2e^- \longrightarrow H_2O_2 \quad (3.3)$$

$$H_2O_2 + 2H^+ + 2e^- \longrightarrow 2H_2O \quad (3.4)$$

These redox reactions can be driven by applying the appropriate potential or current to the working electrode with respect to a reference and/or counter electrode. This reaction

was used to profile pH gradients at optically transparent single-walled carbon nanotubes ultramicroelectrodes (OT-SWNTs-UME) described herein.

The electrochemical activity of the OT-SWNTs-UMEs is quantified using tris(2,2-bipyridine)ruthenium(II) $Ru(bpy)_2^{3+}$ in two complementary roles: (i) as the redox active species and (ii) as the fluorophore in the CLSM set-up. This allows simultaneous tracking and visualising of the electrochemical processes at electrode surfaces. $Ru(bpy)_2^{2+}$ is a luminescent compound widely used in electrogenerated chemiluminescence techniques.[40-41] In contrast, oxidised form, $Ru(bpy)_3^{3+}$, is non-luminescent. Herein, the development of $Ru(bpy)_2^{3+}$ concentration gradients at the SWNTs electrode surface is visualised by monitoring the depletion of the luminescent $Ru(bpy)_2^{2+}$ at the OT-WSNTs-UME at the limiting current. 3D maps of concentration were recorded and assessed, including a discussion of optical effects that are encountered at OT-SWNTs-UMEs visualised by CLSM.

3.2. Introduction to Carbon Nanotubes

It is important to consider the properties of CNTs, compared with macroscopic carbon structures, as these may influence the characteristics of CNT-based electrodes. Their name is derived from their long, hollow structure with the walls formed by one-atom-thick sheets of carbon, called graphene. [42] These sheets are rolled at specific and discrete chirality, and the combination of the rolling angle and radius determines the nanotube properties; for example, whether the individual nanotube shell is a metal or semiconductor.[43] As well single-walled carbon nanotubes (SWNTs),[44-45] multi-walled carbon nanotubes (MWNTs) are also possible,[46] but are not consider herein. A single-

walled carbon nanotube can be described as a one-atom-thick layer of graphite sheet called graphene, rolled into a hollow seamless cylinder.[45]

Various techniques have been reported for nanotube growth, among which the most developed and widely used are: arc discharge, laser ablation, chemical vapour deposition (CVD) and high pressure carbon monoxide process based on the floating CVD approach.[47-49] This latter process is used for the bulk production of high-purity SWNTs by Unidym Inc., U.S.A. Random networks of SWNTs can be grown by catalysed chemical vapour deposition (cCVD) on silicon (Si) substrates[50] and silicon with an amorphous layer of silicon oxide (Si/SiO_2)[43,51-53]. An image of such a network, as used in the work herein, is shown in Figure 3.1, obtained by field emission scanning electron microscopy (FE-SEM).[43] In cCVD synthesis, an iron, nickel or cobalt catalyst (in the form of nanoparticles (NPs), whose size controls the diameter of the resulting SWNT[54] is placed on the substrate in an oven at 900 to 1000 °C. The carbon vapour source absorbs into the catalyst NPs, causing it to form a liquid eutectic (metal carbide [55-56]). Supersaturation of the catalyst results in solid precipitation forming SWNTs. If synthesised in this way, the SWNTs require no further purification.

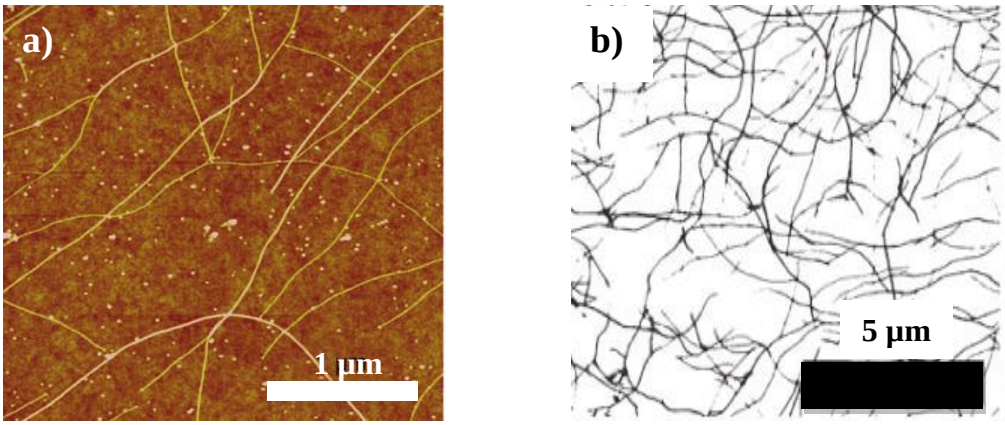

Figure 3.1: a) AFM (3 nm × 3 nm) AFM images (full height scale=5 nm) of a SiO_2 surface after cCVD growth of SWNTs. b) associated FE-SEM image of a SWNT network. The scale bar represents 5 µm. Taken from reference.[43]

The nanoscale size and unique electrical properties of SWNTs have prompted investigations into their electrochemical behaviour. Previous electrochemical studies of SWNTs have involved a variety of different electrode arrangements and pretreatments.[57-62] To create an electrode from pristine random SWNTs networks (see Figure 3.2), gold contact electrodes are evaporated onto the substrate. The substrate is then covered with a layer of electrically insulating photoresists which is exposed and removed in a defined region using photolithography to reveal the underlying SWNTs network while the contact electrodes remain insulated.[63]

CNTs have received enormous attention particularly in analytical electrochemistry, because CNTs are chemically relatively inert and exhibit remarkable electrochemical properties: good electrical conductivity,[64] low background current,[58,60,65] wide potential window and low capacitance in the pristine state.[65-66] Therefore, it can be stated that CNTs have the capability to make excellent electrode materials.[57] The amperometric and electrochemical characterisation of SWNT mats has demonstrated their superior

behaviour as disc UMEs, allowing applications in electroanalysis at concentrations well below the capabilities of other carbon electrodes (e.g., GC). These features made them very attractive electrode materials of high sensitivity. These SWNTs mats exhibit absolute transparencies in the UV-Vis range.[57]

Optically transparent electrodes (OTEs) currently have widespread application in modern electro-optical devices,[67-68] such as solar cells[69], liquid crystal displays (LCDs), thin film transistors (TFTs) or light-emitting diodes (LEDs), and are typically based on thin layers of indium-tin-oxide (ITO).[67] Although ITO exhibits high electrical conductivity, it has some limitation as it is considered a brittle, rough and costly material.[69-70] Alternatively, a wide range of OTEs have been introduced based on the deposition of other transparent conductive thin films. The most attractive among them are films of carbon nanostructures, However, designing a film-based OTE requires a thickness of typically tens of nanometers,[71] to be optically transparent. At such thickness, most electrode materials exhibit large internal resistances. So, there is a tradeoff between optical transparency and electrical resistivity when designing OTEs.[72] SWNTs exhibit superior flexibility in terms of conductivity and transparency, and have been successfully used as optically transparent flexible TFTs, solar cells, and in spectroelectrochemistry.[73]

Herein, the use of SWNTs mats are introduced as optically transparent UMEs by using single crystal quartz as a substrate and visualizing the electrochemical processes at the UME surface (from the back) with state-of-the-art fluorescence CLSM. The work herein, as well as demonstrating attractive opto-electrochemical properties of SWNTs electrodes, provides a platform for the extensive development and application of CLSM.

3.2.1. Characterisation of SWNTs ultrathin films

Networks of SWNTs on single crystal ST-cut quartz substrates were produced by optimising the sputter parameters for cobalt deposition.[57] A typical tapping mode AFM height image in Figure 3.2 shows a network of randomly oriented, interconnected SWNTs. Although each SWNT makes numerous contacts with neighbours, forming overlapping layers of SWNTs, this architecture is still very open and does not have a high surface area. As demonstrated with micro-Raman spectroscopy,[57,74] the network consists primarily of single-walled SWNTs with diameter 1–5 nm. Larger apparent diameters (10–20 nm as shown in Figure 3.2) indicate single-walled SWNTs bundled together or small diameter multi-walled SWNTs.[74] Some catalyst nanoparticles (most likely in unreacted cobalt and cobalt carbide form) are also visible in Figure 3.2, either encapsulated inside the SWNTs or adsorbed on their outer walls. The effect of cobalt on the electrochemistry of these electrodes, in particular with respect to the redox couple employed herein and the background signal, can be considered negligible.

The presence of SWNTs was confirmed with micro-Raman spectroscopy (Figure 2.6) by characteristic G^+ (1594.5 cm^{-1}) and G^- (1576.6 cm^{-1}) peaks and the small D peak at 1342.6 cm^{-1}.[57,59] The G-band is a characteristic peak for all graphite-like structures. It is related to the graphite tangential mode of two atoms in the graphene sp^2 unit cell vibrating against each other. The position of the G-band depends on the symmetry of the tangential vibration. The splitting of the band to G^+ and G^- peaks is related to the tangential vibration either along the Nanotube axis or its circumference, respectively where the first is independent of SWNT diameter, whilst the latter decreases with decreasing diameter. The disorder-induced D band is related to the presence of structural defects which locally change hybridisation of carbon to sp^3. The ratio between

the G and D bands provides insight into the purity of SWNTs grown. The Radial Breathing Mode (RBM) band, characteristic of SWNTs only, originates from the totally symmetric vibrations of carbon atoms in the SWNT structure, and can be used to determine the SWNT diameter. However in the particular case of SWNTs on ST-cut quartz the RBM signal was disturbed due to overlapping with the characteristic peaks of blank quartz in the region below 500 cm^{-1}.

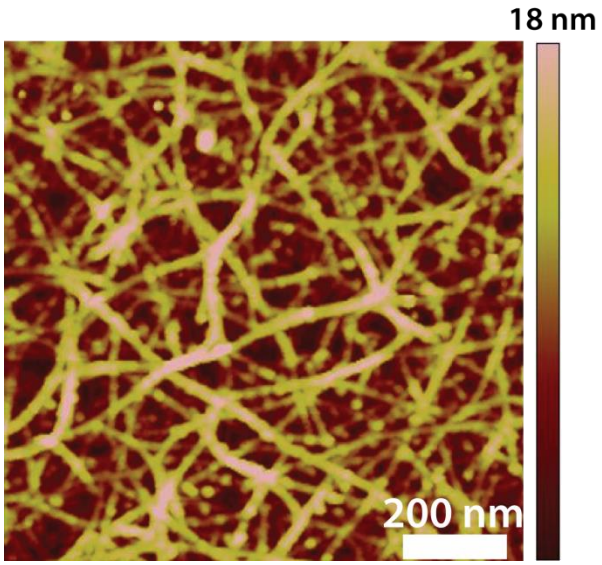

Figure 3.2: 1 µm x 1 µm tapping mode AFM height images of SWNTs networks and ultrathin mats grown on single crystal ST-cut quartz substrate, using Co as the catalyst, sputter-deposited on the substrate 20 s prior to growth.

3.2.2. Characterisation of SWNTs disc OT-UMEs

To validate the optical transparency of CNT networks, UV-visible absorption measurements were carried out in the wavelength range 200–800 nm. Absorption spectra were collected as shown in Figure 3.3 for: (i) blank ST-cut quartz substrate, and ST-cut quartz covered with either (ii) SWNTs networks, or (iii) S1818 photoresist. Full transparency of the blank ST-cut quartz, and ST-cut quartz covered with SWNTs was revealed in the entire UVvisible range studied. The spectrum of S1818 photoresist

showed strong absorption at wavelengths below 365 nm and weaker absorption at ca. 405 nm and ca. 436 nm, attributed to the photoactive component of the photoresist, diazonaphthoquinone (DNQ).[75] As this is in the CLSM detection range, thus it would be expected to have an effect on the light intensity signal from the area outside the UME surface. By focusing near the centre of the electrode surface for all of the electrochemical measurements, the influence of the photoresist was negated.

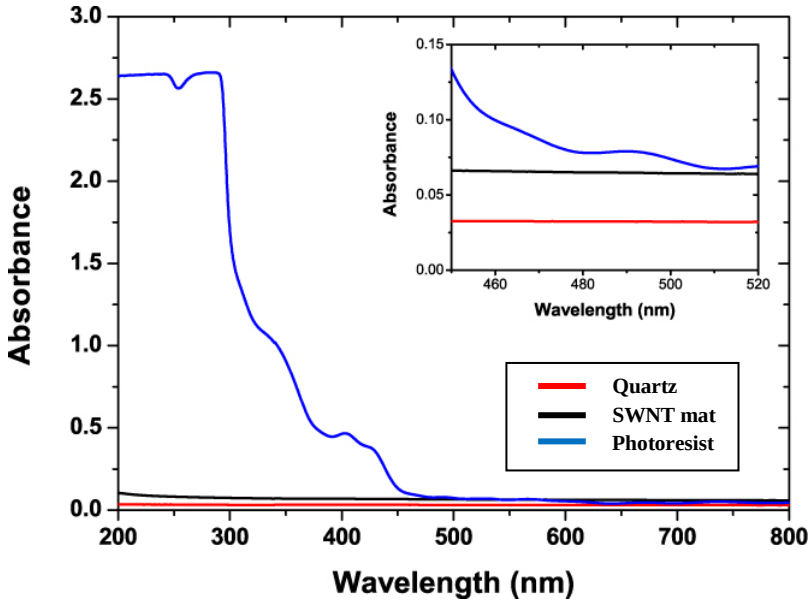

Figure 3.3: UV-Vis spectra of: blank ST-cut quartz; SWNTs mat grown on ST-cut quartz substrate; and ST-cut quartz coated with S1818 positive photoresist.

The strong fluorescent properties of DNQ [75-76] allow readily locating of the UME in the photoresist layer using CLSM fluorescence mode without the need of using any additional fluorophore. The CLSM bright field and fluorescence modes (Figure 3.4(a) and (b), respectively) reveal the shape of the 50 μm diameter disc OT-SWNTs-UME surrounded by photoresist (1.5 μm thickness) and separated from the gold band by *ca.* 250 μm. Only those SWNTs in the disc area are exposed to the solution of interest; the remaining portion is insulated with photoresist. The blurring at the UME/photoresist

interface (UME edges) is a consequence of the spatial resolution of the confocal imaging (1-2 µm) at the restricted (10x) operating magnification.

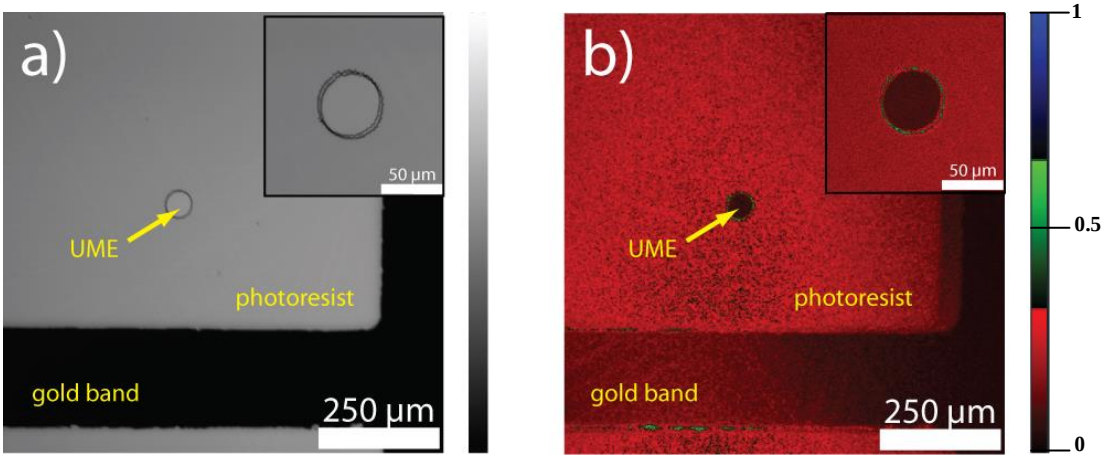

Figure 3.4: Brightfield mode (a) and fluorescence mode images (b) of an optically transparent carbon nanotube ultramicroelectrode (zoomed out and zoomed in). The images were recorded in the *x-y* plane parallel to the electrode.

3.3. Visualisation of the ORR at the SWNTs disc OT- UMEs

The formation of pH profiles at OT-SWNTs- UMEs was examined. Figure 3.5 shows a typical CV of oxygen reduction, and simultaneous light intensity change over the same potential range, recorded at disc OT-SWNTs-UMEs surface in an aqueous solution containing 0.1 M NaCl and 8 µM fluorescein at initial pH 5. The initial low fluorescence intensity increased in the forward scan direction due to fluorescein deprotonation due to production of hydroxide ions (OH^-) (pH > 5.5). It reached a plateau at a potential of the limiting current. The intensity decreases in the reverse scan direction due to fluorescein protonation as the electrode reaction is switched off. The pH profiles have a fairly homogeneous radial shape, characteristic of a disc UME, as shown in the insets of Figure 3.5. The diameter of the fluorescence profiles, over 400 µm (> 8

times larger than the size of the UME itself), corresponds well with the analogous pH profiles obtained at a solid Pt electrode.[7]

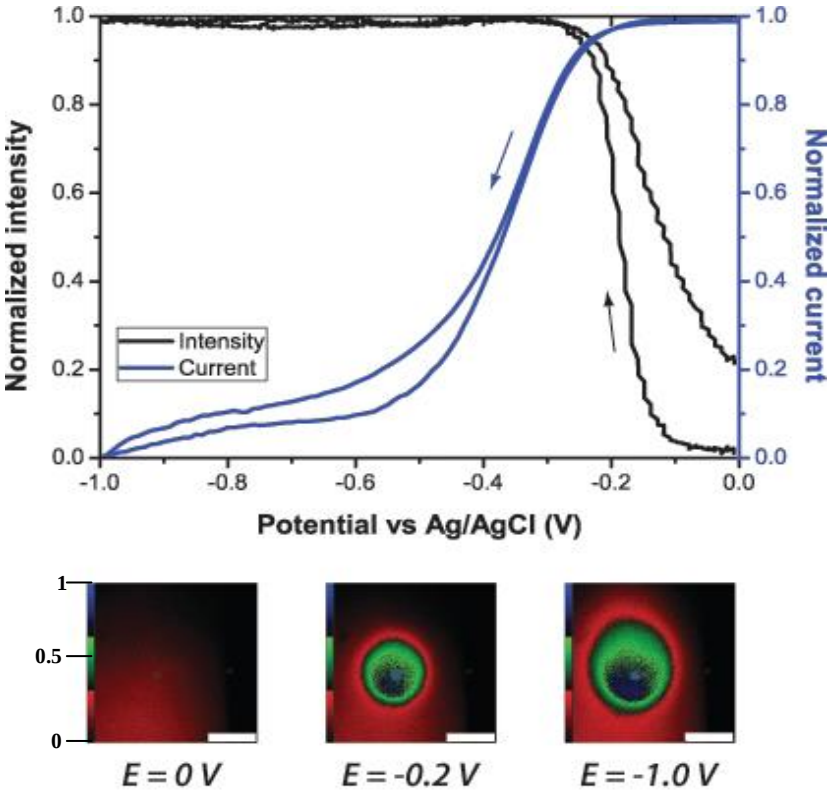

Figure 3.5: CV of ORR and simultaneous change of solution light intensity as a function of potential, at a SWNTs disc OT-UME (scan rate 10 mVs^{-1}) for 0.1 M NaCl aqueous solution with 8 µM fluorescein and an initial pH 5. The arrows indicate the initial scan direction. The intensity values were collected from the middle of the UME surface, from a 35 µm diameters region of interest (ROI). The fluorescence mode insets illustrate the development of pH gradients as a function of potential. The scale bars are 250 µm.

The CLSM technique also allows visualisation into the solution during which 3D maps of the concentration profile are constructed by collecting sections across the surface plane (*xyz* scan), for example when the electrode is held at the steady-state current. The intensity change after stepping the potential to a value of the steady state current, was recorded with CLSM by scanning the surface plane (*xy*) over a period of time required

for the redox couple to reach a steady-state. Figure 3.6(a) shows a typical 3D map of fluorescent intensity from fluorescein at, and near to, the OT-SWNTs-UME surface during the diffusion limited ORR.

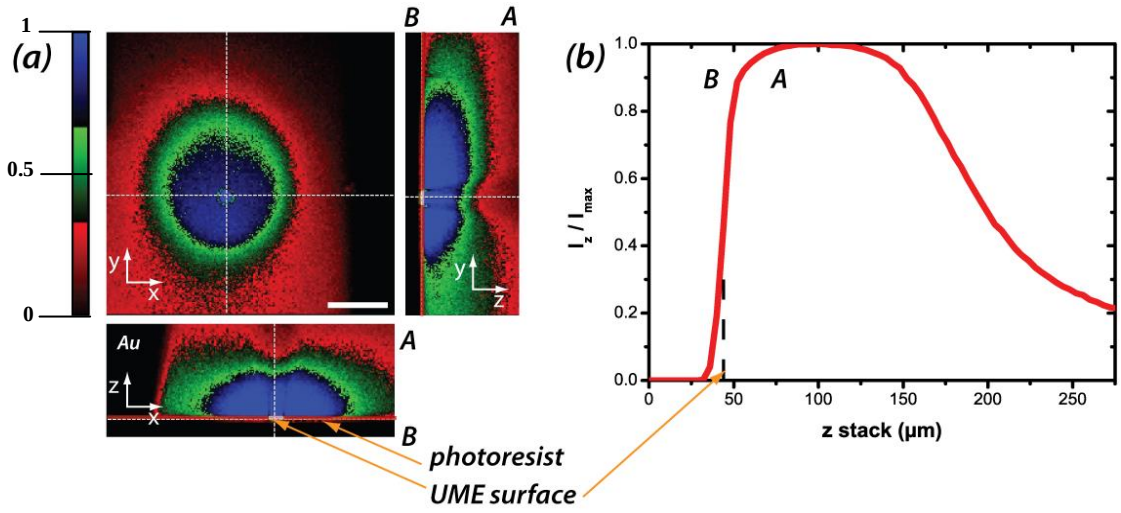

Figure 3.6: (a) Fluorescence intensity at a potential of -1.0 V in 0.1 M NaCl solution with 8 µM fluorescein in the *xy*, *xz* and *yz* planes. The scale bar in the xy image is 250 µm. The red and white lines in *xz* and *yz* cross sections indicate the photoresist and OT UME surface. (b) A graph of intensity below (B) and above (A) the OT-UME plane in 35 µm diameter ROI. The dashed line indicates the electrode surface.

Figure 3.6(b) shows a corresponding cross section of the profile through a 35 µm diameter ROI, located at the centre of the electrode. CLSM resolution and DNQ fluorescence impose limitations on the shape of the pH profile in the *z* direction (discussed in the following section), however the range of the solution maximum intensity (pH above 7.5) is ca. 100 µm. Gradual decrease of the intensity further above the electrode is distinguishable, indicating a decrease of solution pH away from the electrode area down to a pH value of the bulk solution (pH ca. 5). A dip in the profile directly above the electrode has been observed as result of excess DNQ fluorescence around the electrode as can be seen in Figure 3.6 (a).

3.3.1. Dynamic Visualisation of $Ru(bpy)_3^{2+}$ concentration during CV measurements at SWNTs disc OT- UME

Figure 3.7 (a) shows a typical CV (red line) for the oxidation of 10 mM $Ru(bpy)_3^{2+}$ in 0.1 M NaCl at a 50 µm diameter disc-shaped OT-SWNTs-UME and a corresponding solution intensity change (black line) at the electrode surface. The intensity was measured simultaneously from the centre of the electrode only (35 µm in diameter) to avoid the contribution of the photoresist luminescent properties coming from the photoactive component – diazonapthoquinone,[76] and the blurring of the UME edges, as discussed above. The shape of the curve corresponds to a reversible redox system (wave slope of 59 mV).[77] The process is electrochemically reversible; the difference between the quartile potentials, $E_{3/4} - E_{1/4}$, is 59 ± 1 mV and 58 ± 1 mV for forward and reverse scan directions, respectively.[77] The limiting steady-state current, i_{lim}, is ca. 55 nA, consistent with the value expected at an inlaid disc electrode,[77] assuming the diffusion coefficient, of $Ru(bpy)_3^{2+}$ is 5.6×10^{-6} cm^2 s^{-1}.[78] The electrochemical reversibility is clearly visible also in the intensity signal, which is changing in the opposite direction to the current change. The initially high intensity of the solution at the electrode surface is decreasing due to mass transfer of $Ru(bpy)_3^{2+}$ species from the bulk to the electrode surface and oxidation of highly luminescent $Ru(bpy)_3^{2+}$ to non-luminescence Ru(III) oxidation state.

It can clearly be seen that during the forward potential scan, the initial high intensity (I_t = 0) of the solution at the electrode surface decreases due to conversion of $Ru(bpy)_3^{2+}$ to $Ru(bpy)_3^{3+}$. The intensity value reaches a minimum plateau at the potential of the limiting current. In the reverse scan direction $Ru(bpy)_3^{3+}$ is converted back to $Ru(bpy)_3^{2+}$ and the intensity increases to the initial, maximum value. The

reversibility of $Ru(bpy)_3^{2+}$ oxidation is evidenced in Figure. 3.8(b) where a linear relationship between normalised intensity and current values in the range of the quartile potentials ($E_{1/4}$ and $E_{3/4}$) for the forward and reverse scan directions is seen. The nearly parallel lines in Figure 3.8(b) highlight the reliability of combined CLSM and electrochemical studies. Similar profiles to the ones shown in the insets of Figure. 3.7(a) were recorded for lower (1 mM and 5 mM) concentrations of $Ru(bpy)_3^{2+}$. In all cases, reversible CVs of $Ru(bpy)_3^{2+}$ oxidation were obtained, with currents proportional to the $Ru(bpy)_3^{2+}$ concentration.

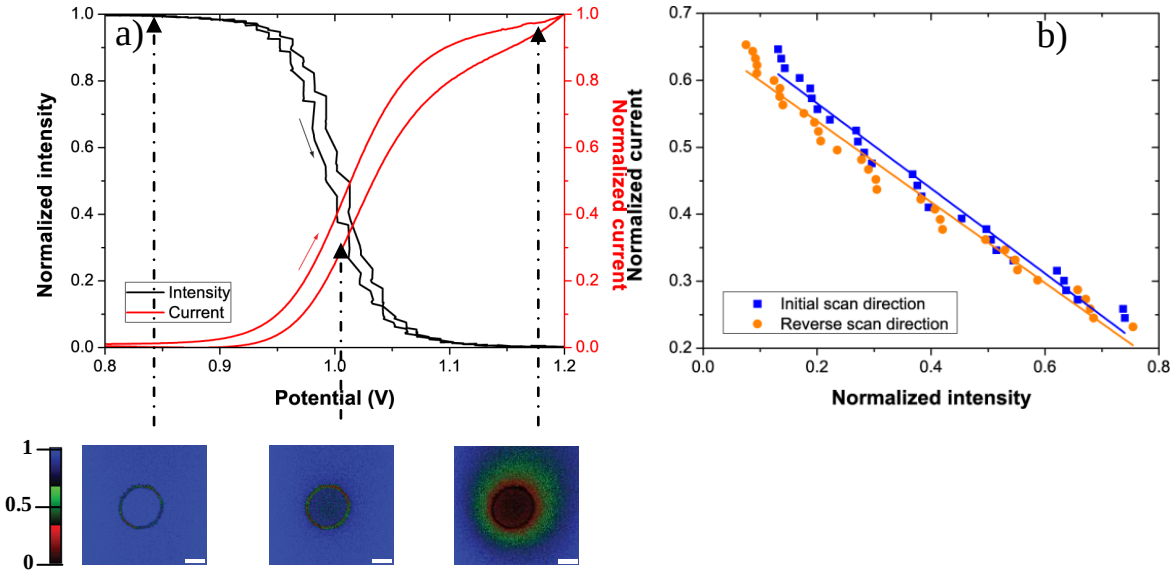

Figure 3.7: (a) CV (red) and simultaneous change of the fluorescence intensity (black: scan rate 5 mV/s) for the oxidation of 10 mM $Ru(bpy)_3^{2+}$ in aqueous solution in 0.1 M NaCl. The arrows indicate the forward scan direction. The intensity values were collected from the 35 µm diameter region of interest at the centre of the UME. Intensity values and current values were normalised by the initial intensity value at time = 0 s (It=0) and the steady-state limiting current value (i_{lim}), respectively. The insets show fluorescence profiles near the OT-SWNTs-UME surface during $Ru(bpy)_3^{2+}$ oxidation. The scale bars are 25 µm. (b) Relationship between normalised current and fluorescence intensity change for forward andreverse scan directions in the range of quartile potentials of the voltammetric signature.

The insets in Figure 3.7(a) show formation of radial fluorescence profiles that develop at the OT-SWNTs-UME surface at three potential values. The profiles are formed due to local depletion of luminescent $Ru(bpy)_3^{2+}$ at the electrode. The intensity decrease in the centre of the OT-CNT-UME at the steady state potential (1.2 V) is due to the conversion of $Ru(bpy)_3^{2+}$ to $Ru(bpy)_3^{3+}$, discussed above.

3.3.2. Three dimensional concentration profiles of $Ru(bpy)_3^{2+}$ at the steady-state current.

The CLSM technique also allows visualisation into the solution. A three dimensional map of the concentration profile is constructed by collecting sections across the surface plane (*xyz* scan) when the electrode is held at the steady-state current. The intensity change during stepping the potential to a potential of a steady state current, was recorded with CLSM by scanning the surface plane (*xy*) over a period of time required for the redox couple to reach a steady-state. Figure 3.8 illustrates the case for 10 mM $Ru(bpy)_3^{+2}$ during the initial 5 s quiet time, required for potentiostat stabilisation, the solution intensity is at its maximum, constant value. After this time, the potential is stepped to a value of $Ru(bpy)_3^{2+}$ oxidation at a diffusion-limited rate (see Figure 3.8). A simultaneous decrease in the intensity profile to a minimum, value was recorded over the next few seconds. This period corresponds to the time required for $Ru(bpy)_3^{2+}$ oxidation to reach a steady state. The radial concentration profile in the inset in Figure 3.8 depicts a dark domain confined to the electrode area; it illustrates accumulation of $Ru(bpy)_3^{+3}$ at the electrode surface.

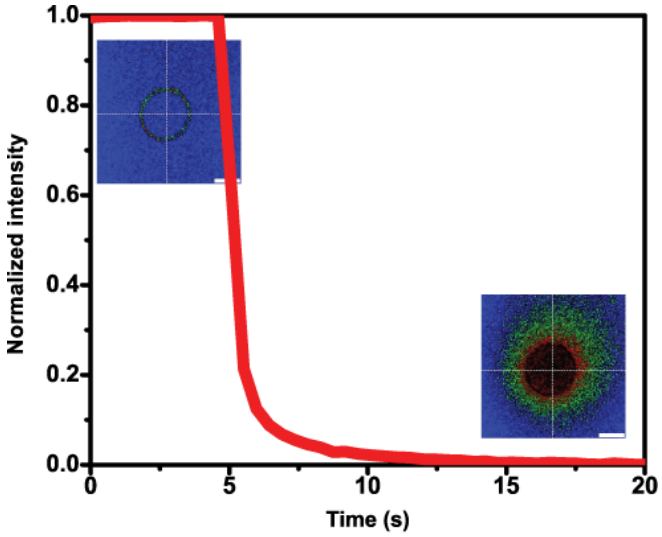

Figure 3.8: The change of solution intensity over time during stepping up the potential from 0 V to the potential of the mass transport limiting current (1.2 V), determined from the CV for 10 mM $Ru(bpy)_3^{2+}$ aqueous solution in 0.1 M NaCl. The inlets indicate the formation of the diffusion zone at the UME surface. The scale bar is 25 µm.

Figure 3.9 (a), (c) and (e) show the fluorescence intensity profiles at the cylindrical axis of symmetry along the co-ordinate normal to the electrode, starting at the back of the electrode and moving through it into the solution. With no potential applied, the intensity signal increases with increasing z-coordinate, until a maximum is reached. The transition from minimum to maximum intensity is not a step function, due to the magnification (10×) at the lens employed. After stepping the potential from 0 V, where no electrode reactions occur, to the diffusion- controlled limit, for 60 s, the intensity signal shifted significantly into the bulk solution and the transition from the minimum to maximum values is less steep, which can be attributed to depletion of $Ru(bpy)_3^{2+}$ in the diffusion layer of the OT-SWNT-UME.

The zone and the intensity change of the concentration layer was smaller for lower concentrations of $Ru(bpy)_3^{2+}$ (1 mM, 5 mM and 10 mM), as shown in Figure 3.9 (a), (c)

and (e), respectively . Figures 3.9 (b), (d) and (f) present a comparison of the intensity change during the period of the steady state current as a function of the distance from the electrode, together with the intensity change across the electrode before the potential step for comparison. In both cases (reaction on or off) no signal is detected far below the surface, as would obviously be expected. At the steady state current regime the low intensity of the solution is clearly visible above and just below the UME plane. The intensity increases less steeply than when no potential is applied (note the position of the surface in both plots). The maximum intensity value, corresponding to the bulk solution intensity, is followed by a sudden drop in intensity demonstrating the absorption of light away from the electrode by Ru(II) species in the bulk solution which depends on the concentration.

The fluorescence intensity profiles illustrated in Figure 3.9, after and before the potential step, are indicative of the concentration boundary layer, δ, formed at the OT-SWNTs-UME, which is of the expected thickness 9.8 μm based on $\delta=\pi a/4$ (where a is the electrode radius). Further into the solution, there is a decrease of intensity, in both profiles, due to light absorption by $Ru(bpy)_3^{2+}$ in the bulk solution.[2] This convolution of the response highlights the importance of measuring the concentration (fluorescence) profiles from the rear of electrode, as demonstrated here.

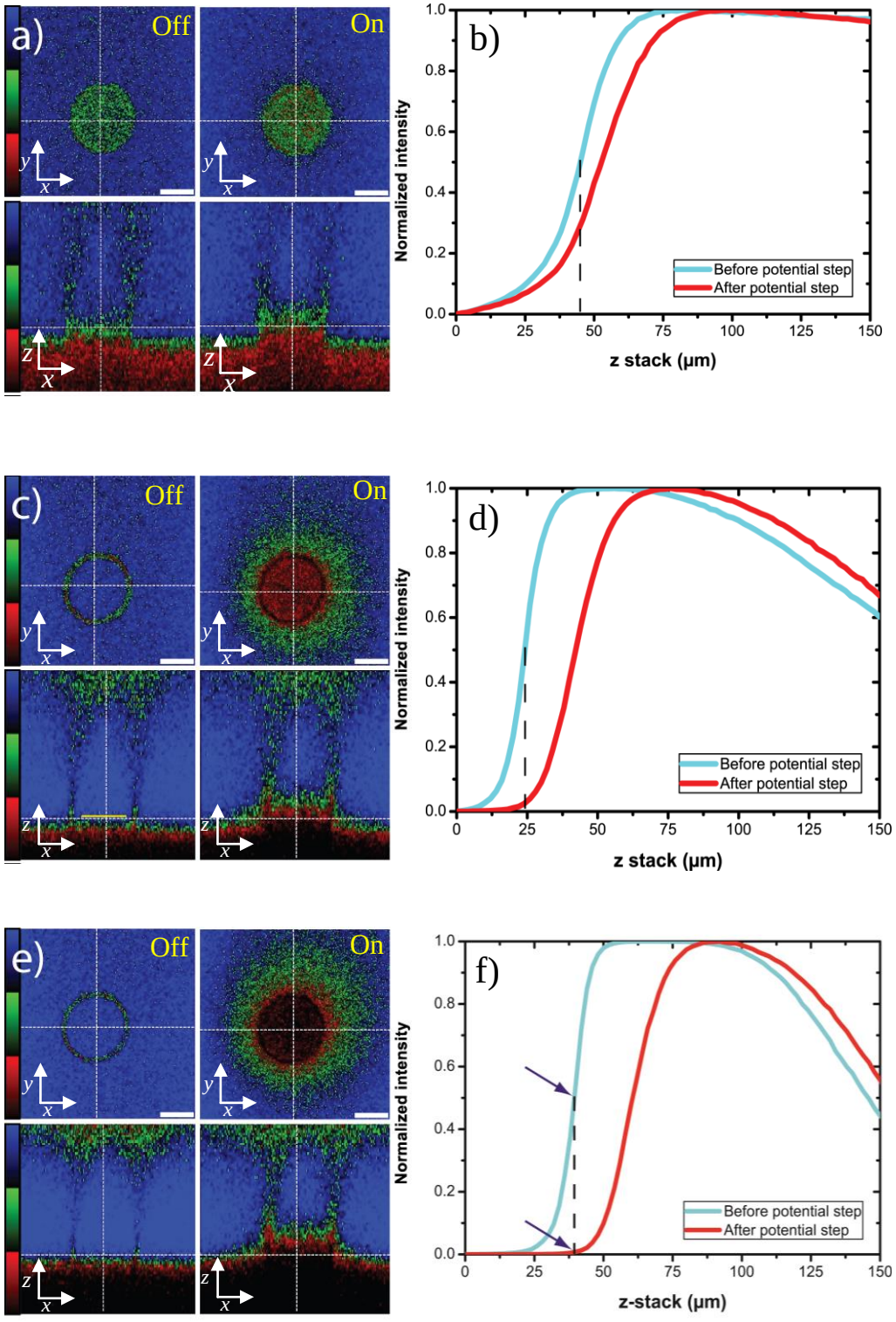

Figure 3.9: Cross sectional light intensity change below and above the UME surface before (left) and after (right) the potential step for the 1 mM (a), 5 mM (c), and 10 mM (e) $Ru(bpy)_3^{2+}$ in 0.1 M NaCl. All images were collected with the *z*-volume 150 µm (vertical white dashed line) and the *z*-step 2 µm. *Z*-stack before the potential step and during the steady state for the 1 mM (b), 5 mM (d), and 10 mM (f) $Ru(bpy)_3^{2+}$ in 0.1 M NaCl. The scale bars in (a, c) and (e) are 25 µm. Dark blue arrows indicate the position

of the electrode surface in both scans. The light intensity values were normalised taking into account the intensity signal from the 35 µm diameter region of interest only.

Notably, studies on $Ru(bpy)_3^{2+}$ oxidation (at 10 mM in 0.1 M NaCl) at 25 µm Pt disc UME revealed strong absorption of the excitation light in the bulk solution, precluding CLSM visualisation of the redox reaction. $Ru(bpy)_3^{2+}$ absorption of the excitation light, called the primary inner filter effect, was discussed by Amatore et al. in the studies on dynamics of $Ru(bpy)_3^{2+}$ concentration profiles imaged with coherent optical fibres [2]. The authors indicated the local absorbance of the excitation light by $Ru(bpy)_3^{2+}$ as the main factor limiting resolution of fluorescence imaging. Indeed, fluorescence efficiency of $Ru(bpy)_3^{2+}$ is much smaller than for example fluorescein [79]. In both examined cases, $Ru(bpy)_3^{2+}$ oxidation and ORR, a uniform activity of the OT-SWNTs-UMEs mat is evident. The chronoamperometry (CA) experiments validate the capabilities of CLSM in studying mass transfer of redox couples. The results thus demonstrate the unique merit of SWNTs mats as OT-UMEs in monitoring redox reactions which appear inaccessible with conventional electrochemical set-ups.

3.4. Conclusions

CLSM has proven very useful for quantifying the electrochemical activities of the SWNTs-UMEs by tracking the dynamic, reversible concentration profiles of electroactive and photoactive tris(2,2'-bipyridine)ruthenium(II) species during cyclic voltammetry. Disc-shaped OT-CNT-UMEs have been introduced, through a series of electrochemical and fluorescence experiments. The SWNTs networks showed both complete transparency and disc shaped UME characteristics. Visualisation of the mass transfer processes at the electrode has been achieved using state-of-the-art CLSM. Three dimensional diffusion profiles of the electroactive and photoactive $Ru(bpy)_3^{2+}$at the

SWNTs-mat UME were recorded and the optical effects on the imaging resolution were discussed.

These proof-of-concept experiments broaden the potential applications of the introduced SWNTs disc UMEs as reliable and effective sensors for broad optical and electrochemical applications. Further improvement in CLSM resolution and UME fabrication, for example by using thinner quartz substrates could allow the faithful measurement of the concentration profiles to be measured with even higher spatial resolution.

3.5. References

(1) Amatore, C.; Szunerits, S.; Thouin, L.; Warkocz, J. S. *Electroanalysis* **2001**, *13*, 646.
(2) Amatore, C.; Chovin, A.; Garrigue, P.; Servant, L.; Sojic, N.; Szunerits, S.; Thouint, L. *Analytical Chemistry* **2004**, *76*, 7202.
(3) Unwin, P. R.; Macpherson, J. V.; Beeston, M. A.; Evans, N. J.; Littlewood, D.; Hughes, N. P. *Adv Dent Res* **1997**, *11*, 548.
(4) Zhang, J.; Slevin, C. J.; Unwin, P. R. *Chemical Communications* **1999**, 1501.
(5) Fantini, J.; Fournier, D.; Boccara, A. C.; Plichon, V. *Electrochimica Acta* **1997**, *42*, 937.
(6) Unwin, P. R.; Macpherson, J. V. *Chemical Society Reviews* **1995**, *24*, 109.
(7) Rudd, N. C.; Cannan, S.; Bitziou, E.; Ciani, L.; Whitworth, A. L.; Unwin, P. R. *Analytical Chemistry* **2005**, *77*, 6205.
(8) Grime, J. M. A.; Edwards, M. A.; Rudd, N. C.; Unwin, P. R. *Proceedings of the National Academy of Sciences of the United States of America* **2008**, *105*, 14277.
(9) Engstrom, R. C.; Ghaffari, S.; Qu, H. W. *Analytical Chemistry* **1992**, *64*, 2525.
(10) Gabrielli, C.; Ostermann, E.; Perrot, H.; Vivier, V.; Beitone, L.; Mace, C. *Electrochemistry Communications* **2005**, *7*, 962.
(11) Bastos, A. C.; Simoes, A. M.; Gonzalez, S.; Gonzalez-Garcia, Y.; Souto, R. M. *Electrochemistry Communications* **2004**, *6*, 1212.
(12) Rudd, N. C., The University of Warwick, 2007.
(13) Pruiksma, R.; McCreery, R. L. *Analytical Chemistry* **1979**, *51*, 2253.
(14) Wu, H. P.; McCreery, R. L. *Analytical Chemistry* **1989**, *61*, 2347.
(15) Amatore, C.; Pebay, C.; Servant, L.; Sojic, N.; Szunerits, S.; Thouin, L. *Chemphyschem* **2006**, *7*, 1322.
(16) Texier, F.; Servant, L.; Bruneel, J. L.; Argoul, F. *Journal of Electroanalytical Chemistry* **1998**, *446*, 189.
(17) Amatore, C.; Bonhomme, F.; Bruneel, J. L.; Servant, L.; Thouin, L. *Electrochemistry Communications* **2000**, *2*, 235.
(18) Engstrom, R. C.; Ghaffari, S.; Qu, H. W. *Analytical Chemistry* **1992**, *64*, 2525.
(19) Bowyer, W. J.; Xie, J.; Engstrom, R. C. *Analytical Chemistry* **1996**, *68*, 2005.
(20) Vitt, J. E.; Engstrom, R. C. *Analytical Chemistry* **1997**, *69*, 1070.
(21) Fiedler, S.; Hagedom, R.; Schnelle, T.; Richter, E.; Wagner, B.; Fuhr, G. *Analytical Chemistry* **1995**, *67*, 820.
(22) Cannan, S.; Macklam, I. D.; Unwin, P. R. *Electrochemistry Communications* **2002**, *4*, 886.
(23) Amatore, C.; Bonhomme, F.; Bruneel, J. L.; Servant, L.; Thouin, L. *Journal of Electroanalytical Chemistry* **2000**, *484*, 1.
(24) Amatore, C.; Szunerits, S.; Thouin, L.; Warkocz, J. S. *Electrochemistry Communications* **2000**, *2*, 353.
(25) Amatore, C.; Szunerits, S.; Thouin, L. *Electrochemistry Communications* **2000**, *2*, 248.
(26) Baltes, N.; Thouin, L.; Amatore, C.; Heinze, J. *Angewandte Chemie-International Edition* **2004**, *43*, 1431.
(27) Engstrom, R. C.; Weber, M.; Wunder, D. J.; Burgess, R.; Winquist, S. *Analytical Chemistry* **1986**, *58*, 844.
(28) Engstrom, R. C.; Meaney, T.; Tople, R.; Wightman, R. M. *Analytical Chemistry* **1987**, *59*, 2005.

(29) Bard, A. J.; Fan, F. R. F.; Kwak, J.; Lev, O. *Analytical Chemistry* **1989**, *61*, 132.
(30) Barker, A. L.; Unwin, P. R.; Amemiya, S.; Zhou, J. F.; Bard, A. J. *Journal of Physical Chemistry B* **1999**, *103*, 7260.
(31) Barker, A. L.; Gonsalves, M.; Macpherson, J. V.; Slevin, C. J.; Unwin, P. R. *Analytica Chimica Acta* **1999**, *385*, 223.
(32) Slevin, C. J.; Macpherson, J. V.; Unwin, P. R. *Journal of Physical Chemistry B* **1997**, *101*, 10851.
(33) Slevin, C. J.; Unwin, P. R. *Langmuir* **1997**, *13*, 4799.
(34) Mayausky, J. S.; McCreery, R. L. *J. Electroanal. Chem.* **1983**, *145*, 117.
(35) Jan, C. C.; McCreery, R. L.; Gamble, F. T. *Analytical Chemistry* **1985**, *57*, 1763.
(36) Pharr, C. M.; Engstrom, R. C.; Tople, R. A.; Bee, T. K.; Unzelman, P. L. *Journal of Electroanalytical Chemistry* **1990**, *278*, 119.
(37) Engstrom, R. C.; Pharr, C. M.; Koppang, M. D. *Journal of Electroanalytical Chemistry* **1987**, *221*, 251.
(38) Haugland, R. P. *Molecular Probes Handbook of Fluorescent Probes and Research Products,*; 9 ed.; Molecular Probes: USA, 2002.
(39) C.M.A. Brett, A. M. O. B. *Electrochemistry Principles, Methods and Applications*; OUP: Oxford, 1993.
(40) Gerardi, R. D.; Barnett, N. W.; Lewis, S. W. *Analytica Chimica Acta* **1999**, *378*, 1.
(41) Forster, R. J.; Bertoncello, P.; Keyes, T. E. In *Annual Review of Analytical Chemistry* 2009; Vol. 2, p 359.
(42) Hiura, H.; Ebbesen, T. W.; Tanigaki, K. *Advanced Materials* **1995**, *7*, 275.
(43) Edgeworth, J. P.; Wilson, N. R.; Macpherson, J. V. *Small* **2007**, *3*, 860.
(44) Iijima, S. *Nature* **1991**, *354*, 56.
(45) Iijima, S.; Ichihashi, T. *Nature* **1993**, *363*, 603.
(46) Bethune, D. S.; Kiang, C. H.; Devries, M. S.; Gorman, G.; Savoy, R.; Vazquez, J.; Beyers, R. *Nature* **1993**, *363*, 605.
(47) Bronikowski, M. J.; Willis, P. A.; Colbert, D. T.; Smith, K. A.; Smalley, R. E. *Journal of Vacuum Science & Technology a-Vacuum Surfaces and Films* **2001**, *19*, 1800.
(48) Nikolaev, P.; Bronikowski, M. J.; Bradley, R. K.; Rohmund, F.; Colbert, D. T.; Smith, K. A.; Smalley, R. E. *Chemical Physics Letters* **1999**, *313*, 91.
(49) Scott, C. D.; Povitsky, A.; Dateo, C.; Gokcen, T.; Willis, P. A.; Smalley, R. E. *Journal of Nanoscience and Nanotechnology* **2003**, *3*, 63.
(50) Murakami, Y.; Chiashi, S.; Miyauchi, Y.; Maruyama, S. *Japanese Journal of Applied Physics Part 1-Regular Papers Brief Communications & Review Papers* **2004**, *43*, 1221.
(51) Kong, J.; Soh, H. T.; Cassell, A. M.; Quate, C. F.; Dai, H. J. *Nature* **1998**, *395*, 878.
(52) Christoffersen, J.; Christoffersen, M. R.; Arends, J.; Hook, M. *Journal of Crystal Growth* **1994**, *137*, 545.
(53) Snow, E. S.; Novak, J. P.; Campbell, P. M.; Park, D. *Applied Physics Letters* **2003**, *82*, 2145.
(54) Shim, Y. B.; Park, S. M. *Journal of Electroanalytical Chemistry* **1997**, *425*, 201.
(55) Yoshida, H.; Takeda, S.; Uchiyama, T.; Kohno, H.; Homma, Y. *Nano Letters* **2008**, *8*, 2082.
(56) Yoshida, H.; Takeda, S.; Uchiyama, T.; Kohno, H.; Homma, Y. In *Nanotubes, Nanowires, Nanobelts and Nanocoils - Promise, Expectations and Status*; Bandaru, P. R. G. S. K. I., Ed. 2009; Vol. 1142, p 3.

(57) Dumitrescu, I.; Edgeworth, J. P.; Unwin, P. R.; Macpherson, J. V. *Advanced Materials* **2009**, *21*, 3105.
(58) Dumitrescu, I.; Unwin, P. R.; Macpherson, J. V. *Chemical Communications* **2009**, 6886.
(59) Dumitrescu, I.; Unwin, P. R.; Macpherson, J. V. *Electrochemistry Communications* **2009**, *11*, 2081.
(60) Dumitrescu, I.; Unwin, P. R.; Wilson, N. R.; Macpherson, J. V. *Analytical Chemistry* **2008**, *80*, 3598.
(61) Rutkowska, A.; Bawazeer, T. M.; Macpherson, J. V.; Unwin, P. R. *Physical Chemistry Chemical Physics* **2011**, *13*, 5223.
(62) Rutkowska, A.; Walker, D.; Gorfman, S.; Thomas, P. A.; Macpherson, J. V. *Journal of Physical Chemistry C* **2009**, *113*, 17087.
(63) Day, T. M.; Wilson, N. R.; Macpherson, J. V. *Journal of the American Chemical Society* **2004**, *126*, 16724.
(64) Saito, R.; Fujita, M.; Dresselhaus, G.; Dresselhaus, M. S. *Physical Review B* **1992**, *46*, 1804.
(65) Bertoncello, P.; Edgeworth, J. P.; Macpherson, J. V.; Unwin, P. R. *Journal of the American Chemical Society* **2007**, *129*, 10982.
(66) Rosenblatt, S.; Yaish, Y.; Park, J.; Gore, J.; Sazonova, V.; McEuen, P. L. *Nano Letters* **2002**, *2*, 869.
(67) Harlev, E.; Gulakhmedova, T.; Rubinovich, I.; Aizenshtein, G. *Advanced Materials* **1996**, *8*, 994.
(68) Minami, T.; Miyata, T. *Thin Solid Films* **2008**, *517*, 1474.
(69) Minami, T. *Thin Solid Films* **2008**, *516*, 1314.
(70) Minami, T. *Thin Solid Films* **2008**, *516*, 5822.
(71) Shipway, A. N.; Katz, E.; Willner, I. *Chemphyschem* **2000**, *1*, 18.
(72) Donner, S.; Li, H. W.; Yeung, E. S.; Porter, M. D. *Analytical Chemistry* **2006**, *78*, 2816.
(73) Heras, A.; Colina, A.; Lopez-Palacios, J.; Kaskela, A.; Nasibulin, A. G.; Ruiz, V.; Kauppinen, E. I. *Electrochemistry Communications* **2009**, *11*, 442.
(74) Guell, A. G.; Meadows, K. E.; Unwin, P. R.; Macpherson, J. V. *Physical Chemistry Chemical Physics* **2010**, *12*, 10108.
(75) Vleggaar, J. J. M.; Huizer, A. H.; Varma, C.; Kraakman, P. A.; Nijssen, W. P. N.; Visser, R. J. *Journal of Vacuum Science & Technology B* **1993**, *11*, 688.
(76) Hui, E. E.; Bhatia, S. N. *Langmuir* **2007**, *23*, 4103.
(77) Bard, A. J.; Faulkner, L. R. *Electrochemical Methods. Fundamentals and Applications*; 2ed ed.; Wiley: India, 2006.
(78) Yan, X.; Li, H.; Xu, Z.; Li, W. *Bioelectrochemistry* **2009**, *74*, 310.
(79) Guilbault, G. G. *Practical fluorescence*; Second ed.; CRC, 1990.

Transient Interfacial Kinetics, from Confocal Fluorescence Visualisation: Application to Proton Attack the Treated Enamel Substrate

Introduction

In this chapter the first use of confocal laser scanning microscopy (CLSM) coupled with scanning electrochemical microscopy (SECM) is introduced as means of time dependant visualisation and measurement of proton dispersion on enamel surfaces and the effectiveness of dissolution inhibitors on enamel substrates. This new technique provides an analytical method with high spatial and temporal resolution allowing sub-second analysis of treatment effects on enamel substrates. A decrease of the fluorescein solution intensity was recorded using CLSM during the oxidation of water at an ultramicroelectrode (UME). Studies involved measuring pH profiles close to untreated and treated enamel surfaces. Fluoride and zinc were used as treatments for enamel surfaces to investigate the effect of inhibitors on proton distribution, since they are generally considered to impede the dissolution process.

4.1. Overview

Heterogeneous reactions at liquid/solid interfaces are probably one of the main topics in science and a vast variety of techniques have been applied, mainly focusing on probing the actual reactive sites.[1-2] A reaction at a surface often involves a flux of molecules/ions from a source (or bulk) towards the reactive sites where the reaction takes place. The ability to visualize and analyse such processes is crucial for obtaining a deeper insight into the reaction process. Understanding surface reaction rates is paramount in a number of fields, such as corrosion,[3-5] electrochemical sensors, electrochemical reactors[6] and fuel cells,[6-7] and minerals dissolution.[8-9]

Of particular interest in both medicinal and electrochemical fields is the mapping of concentration profiles within the diffusion layer of an active site,[10-11] as reviewed extensively in the preceding chapter. In order to understand dissolution, well-defined and quantifiable mass transport is the key.[12-15] To this extent, the channel flow cell (CFC) method has proven powerful for studying dissolution processes,[12,14] although one can only measure macroscopic rate over long time period.

Attempts to visualise dynamic proton fluxes have been performed using micro-electrode ion flux estimators (MIFE) where it is possible to simultaneously measure the flux of several different ion species,[16] but it also requires other *ex-situ* visualisation techniques such as SEM and interferometry or profilometry[17] and the main drawback of these methods is the relatively low temporal resolution of c.a. 5 seconds.[18] This is particularly slow in comparison to techniques such as confocal laser scanning microscopy (CLSM) which has a temporal resolution in the order of milliseconds.[19] As highlighted in the previous chapter, fluorescence CLSM to monitor the concentration profile at an electrode surface during an electrochemical reaction was successfully introduced by Unwin and co-workers.[20-22]

SECM is extensively used as a scanning probe technique for studying dissolution processes and kinetics [23-27] and visualization of concentration profiles has been probed down to the micron level. Previous work performed by this group using SECM coupled with finite element modelling on enamel dissolution, allow the rate of acid attack at steady-state condition to be quantified.[8,28] However, inhibitors can only provide a temporary barrier layer and it would be very useful to be able to investigate transient processes and access fast.

Enamel proton-induced dissolution has received extensive attention due to its wide implication in oral science, from caries to acid erosion.[8] CLSM has been applied to many aspects of oral health including dental erosion,[29-30] monitoring the differences between fluoridated and non-fluoridated permanent and deciduous enamel,[31] visualizing enamel rods[32] and even to monitor fluid flow through dentine tubules and substances which subsequently block the tubules.[33] Herein, it is shown that by combining CLSM with UMEs and SECM, greatly enhanced information can be obtained on proton-induced dissolution and the effect of temporary dissolution barriers from well-known treatements.

4.1.1. Enamel Structure

The structure of the tooth is shown in Figure 4.1. Enamel is the hardest and most highly mineralized substance of the body. It is one of the three major tissues which make up the tooth, along with dentin and dental pulp. It is normally visible and supported by underlying dentin.

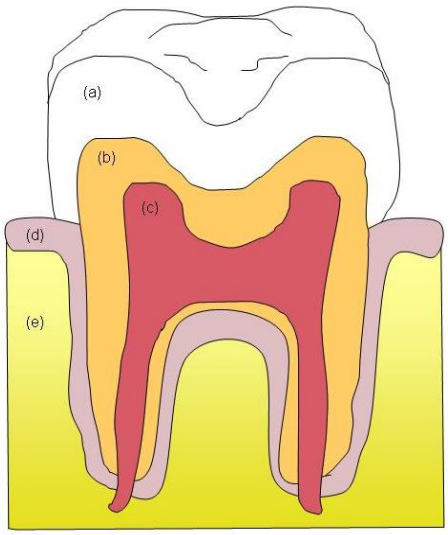

Figure 4.1: A cross sectional schematic of the structure of a tooth; (a) represents the dental hard tissue enamel, (b) represents the dental soft tissue dentine, (c) is the pulp

containing the nerves, (d) is the gum surrounding the tooth and (e) is the bone from which teeth grow.

Enamel has a prismatic macrostructure arising from its production from ameloblast cells. Enamel is essentially composed of 95 wt% impure calcium hydroxyapatite (HAP), $Ca_{10}(PO_4)_6(OH)_2$ and an the remaining being organic material and water.

4.1.2. Enamel Dissolution

An acidic medium can dissolve hydroxyapatite crystals as per equation 4.1, which is usually defined as surface demineralization.[34]

$$Ca_{10}(PO_4)_6(OH)_{2(s)} + 8H^+_{(aq)} \leftrightarrow \quad 10Ca^{2+} + 6HPO^{2-}_{4(aq)} + 2H_2O \qquad (4.1)$$

Enamel dissolution can be defined as the localized loss of dental hard tissue[35] from the tooth surface due to the chemical influence of extrinsic acids[36] (including acidic substances, beverages, foods, medication and environmental exposure to acidic agents) and intrinsic acids[36] (including recurrent vomiting as part of the eating disorder bulimia nervosa or due to the regurgitation of the gastric contents) without the involvement of microorganisms.[36-37] Frequent consumption of acid-containing foods is an important factor in enamel erosion, with many soft drinks are in the pH range between 2 and 3[38] being the most commonly consumed erosive acids.[37] Dental erosion does not only affect enamel but can also reach dentine, causing hypersensitivity, or in severe cases, pulp exposure and even tooth fracture.

Understanding dental erosion would help in the clinical treatment of tooth wear and aid in the development of new dental restorative materials.[33] It would also aid in providing

further insights into the chemical process of erosion, and ways in which erosion can be modified, reduced or prevented. Many techniques have been applied to monitor the dissolution and precipitation kinetics of enamel and hydroxyapatite and the closely related fluorapatite, $Ca_{10}(PO4)_6F_2$, including techniques of scanning electron microscopy (SEM)[39-41] of enamel surfaces atomic force microscopy (AFM)[39-41] profilometry and more recently nanoindentation.[39] There have been numerous and varied studies[39,42] quantifying and characterizing the rate, extent and chemical aspects of enamel erosion.

Typically, the majority of published methods involved subjecting slices of enamel to a collection of acid challenges,[42] ranging in pH from 2.3 to 6.3, or the effect of varying compositions of solution, and effectively changing the saturation level of the solution.[43] Further to this, many studies have included the effect of inhibitory agents and treatments upon the dissolution of enamel and HAP. However, there is still heated debate about the quantitative analysis of enamel dissolution, as much of the past work has involved acid challenges where mass transport is not particularly well-defined. On the contrary, the work described herein is underpinned by using SECM which is capable of delivering material to surfaces with well-defined mass transport and thus surface kinetic effects can readily be distinguished, making quantitative analysis more accurate.

4.1.3. Enamel Dissolution Inhibitors

One of the main objectives of this work is to understand the effect of inhibitors on the dissolution of enamel. An interesting property of HAP is the ability to exchange calcium ions by sodium, magnesium, zinc, strontium zinc, or lead ions. Additionally, hydroxyl and phosphate groups can be substituted by chloride, bicarbonate, and fluoride

ions at the apatite surfaces and incorporate in the surface layer in the form of (zincapatites, fluoroapatites, etc.).[44-45] Since the resistance of enamel to acids depends largely on its chemical composition, it is of interest to determine the composition that supports or prevents the process of erosion. Fluoride ions are known to be a good inhibitor of enamel dissolution as it is thought to incorporate into the enamel and increase the hardness and resistance to acid erosion of the enamel. This incorporation may involve loosely or firmly bound fluoride, and the extent to which the fluoride penetrates the enamel is a subject of much debate.[31,46-49]

4.2. Proton Distribution at Disc UME

The work herein use oxidation of water at the surface of a platinum electrode to produces protons as indicated in Equation 4.2. This decrease in pH can be monitored as it causes the disodium fluorescein solution to fluoresce with much less intensity near the electrode surface, as explained in Chapter 3.

$$H_2O \longrightarrow 2H^+ + \tfrac{1}{2} O_2 + 2e^- \qquad (4.2)$$

Figure 4.2 shows the steady-state fluorescence profile obtained at a 25 μm diameter platinum disc electrode upon application of anodic currents of 20 nA, 50 nA and 100 nA in an aqueous solution of 8 μM fluorescein with 0.1 M potassium nitrate, at an initial bulk solution pH of 7.5. A hemispherical fluorescence profile can clearly be seen that mirrors the diffusion profile at a disc UME.[21-22] The fluorescence profile is due to the generation of protons at the electrode surface and the transition from the light region to the dark region marks the change in pH from ca pH 7.5 or higher to ca pH 5.5 or lower, with the midpoint of the boundary at pH 6.1 (see the fluorescence-pH profile, Figure 1.6). The size of the fluorescence profile was found to increase as the applied current

was increased to 100 nA since the current controls the flux of protons away from the electrode surface.

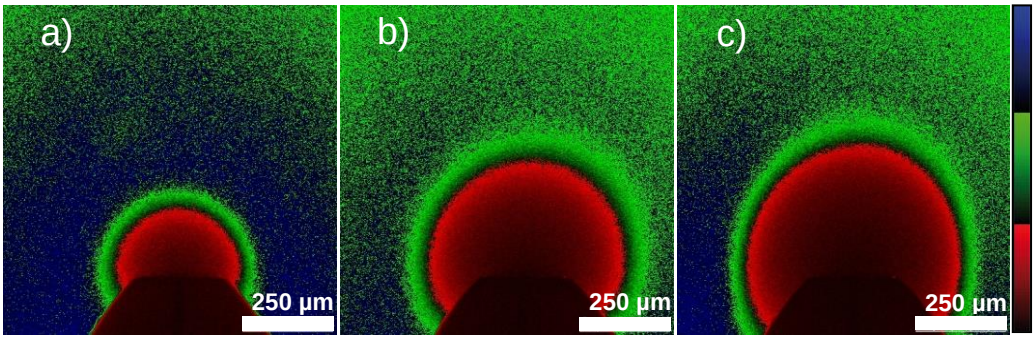

Figure 4.2: CLSM image of water oxidation in 8 µM fluorescein solution with 0.1 M potassium nitrate at a 25 µm diameter Pt disc electrode with applied currents of 10 nA (a), 50 nA (b) and 100 nA (c) at a bulk solution pH of 7.5. The images were recorded in the *x-y* plane parallel to the electrode.

4.3. CLSM Visualisation of Proton Flux during Enamel Dissolution

A UME positioned close to the enamel was used to oxidise water galvanostatically to produce protons, which could be imaged using CLSM. The bulk solution pH was altered to around 7.5 so that the background from the fluorescence of fluorescein was bright. The generation of protons by galvanostatic water oxidation reduced the local solution pH and thus produced a dark domain. The distribution of the pH profiles near the enamel surface was obtained by scanning the distance between the electrode and the enamel surface over time (*xyt* scan, *t*) during application of current of 20, 15, and 10 nA to the working electrode vs. Ag/AgCl for 2 seconds.

The outline of the UME, the platinum wire and the enamel surface can be seen clearly in the overlay image of bright field with fluorescence modes than the fluorescence image (Figure 4.3(a) and 4.3(b) respectively). Notice that the enamel surface is almost

flat relative to the electrode. The electrode was brought close to the enamel surface (20 µm). This distance was chosen to be close enough to the substrate to successfully promote dissolution without net proton loss, and far enough away from the substrate to minimise the effect of dissolution products on the flux of protons from the UME tip. Performing dissolution at a distance any closer than this would potentially promote back reactions.[23-26,50] Moreover, if the electrode was brought too close to the enamel surface, it was too difficult to observe the fluorescence (concentration) profiles.

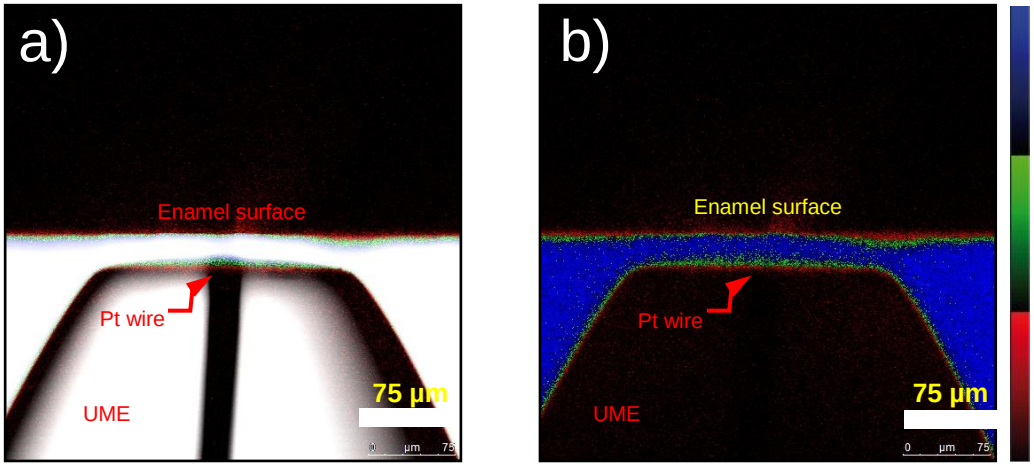

Figure 4.3: Overlay of a brightfield with fluorescence modes (a) and fluorescence mode images (b) of a UME close to enamel with a tip-substrate separation of 20 µm, in 8 µM fluorescein solution with 0.1 M potassium nitrate.

4.3.1. Experimental Results and Analysis

Two typical series CLSM images, captured during application of 20 nA next to glass and enamel surfaces are shown in Figure 4.4. The images clearly show a decrease in fluorescence near the interface, as the oxidation of water decreases the pH. More importantly, it can be seen that the spread of protons is much less for HAP than for glass, because H^+ ion attack the enamel surface and so does not spread as far.

Figure 4.4 illustrates how protons gradually spread along the glass surface, which forms a largely impermeable barrier, filling the gap between the UME and the glass substrate before diffusing into bulk solution. The second series of images, Figure 4.4 (b), in the case of the enamel shows that the overall spread of protons is more confined as consequence of the uptake of protons during the dissolution of an enamel sample.

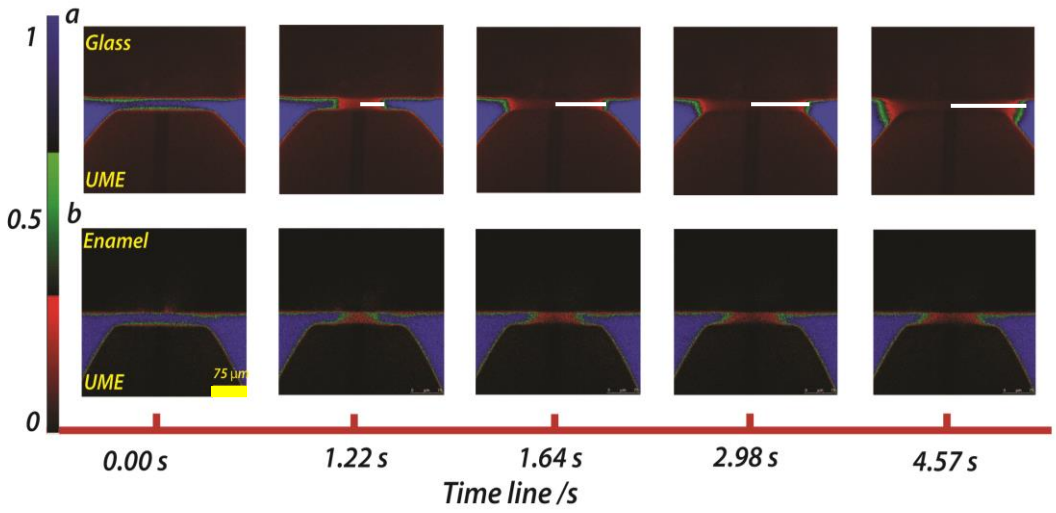

Figure 4.4: Shows a series of images captured from the CLSM at times of 0 sec, when no current has passed, 1.22 seconds, 1.64 seconds, 2.89 seconds and 4.57 seconds (a) The proton distribution next to glass substrate, (b) The proton dispersion near to an enamel substrate. The yellow scale bar represents 75 µm.

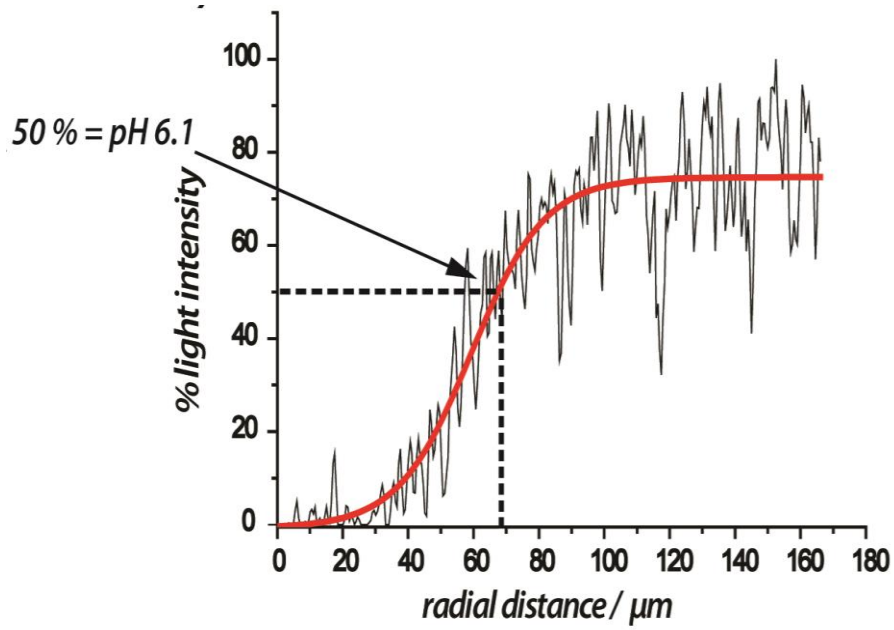

Figure 4.5: Typical sigmoid fit to the right hand side of the fluorescence intensity for water oxidation in 8 µl fluorescein aqueous solution in (0.1 M NaCl). The intensity values were collected from the area between the electrode and the surface of interest after the application of the current.

Figure 4.5 illustrates the change in light intensity along the region of interest (ROI) between the electrode and the glass after the application of the current as indicated with white lines in Figure 4.4 (a). The line extending from the centre of the electrode to the right hand side is shown. The fluorescence intensity rises steadily with radial distance, reflecting the pH profile that has been established in the small volume of solution between the electrode and the sample. The distance from the electrode centre corresponding to 50 % light intensity was determined by fitting a sigmoid curve to each time slice and recording the distance at 50 % light intensity. A typical example of this procedure is illustrated in Figure 4.5. This distance, characteristic of the spreading of protons, was generally plotted as function of time to analyse proton reactivity with the various substrates of interest.

A large spread of protons is indicative relatively of inert surface, whereas a small spread of protons represents significant proton flux towards the substrate due to a dissolution process as per Equation 4.1. The schematic in Figure 4.6 highlighting the impact on the shape of the pH profiles next to glass and enamel surfaces. This indicated that protons produced locally were taken up by the enamel surface, as per equation 4.1. This visualisation highlights clearly how CLSM can be used to distinguish between essentially inert and reactive interfaces.

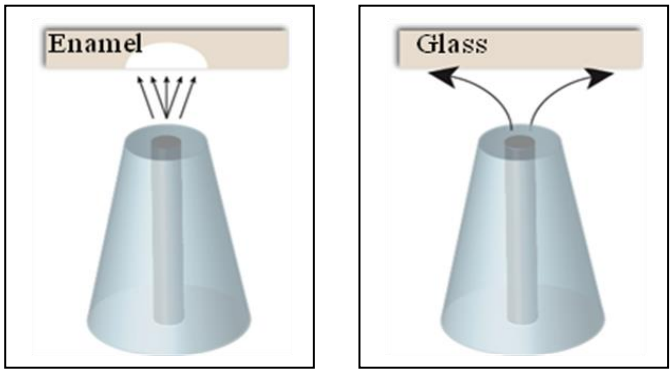

Figure 4.6: the impact upon the shape of the pH profiles next to glass and enamel surfaces.

To quantify the data, the intensity of the fluorescence signal was related to the hydrogen ion concentration using the calibration curve for disodium fluorescein shown in Chapter 1, Figure 4.5. The hydrogen ion concentration at 50 % light intensity was calculated by fitting this calibration data to a sigmoidal 3 parameter empirical equation:

$$y = \frac{a}{1 + e^{-\left(\frac{x - x_o}{b}\right)}} \tag{4.3}$$

and evaluating x, the pH, when y = 50 %. Since

$$\text{pH} = -\log a_{H^+} \tag{4.4}$$

where a_{H^+} is the activity of hydrogen ions and

$$a_{H^+} = \gamma_{H^+}[H^+] \quad (4.5)$$

Taking the activity coefficient of hydrogen ions (γ_{H+}) as 0.75 [51] in 0.1 mol dm^{-3} aqueous solutions, the hydrogen ion concentration corresponding to 50 % fluorescent light intensity is 7.9 x 10^{-7} mol dm^{-3} for disodium fluorescein solution, equivalent to pH 6.1. The plots of the radial distances at 50 % light intensity, as a function of time from the applied current, produced a spatio-temporal profile for a hydrogen ion concentration of 7.9 x 10^{-7} mol dm^{-3}.

Shown in Figure 4.7 (a) are the variation of proton diffusion front (and hence pH) as a function of time for a 20 nA current showing the inherent differences between an untreated surface, a surface treated with 1000 ppm (0.053 M equivalent) NaF or 0.01 M $ZnCl_2$ (1363 ppm equivalent). In particular, it can be seen that the proton diffusion expands more in case of the treated samples (at least initially) than untreated. This indicates that fluoride and zinc treated enamel provides more resistance to acid attack (less uptake of protons) than untreated enamel alone (more uptake of protons).

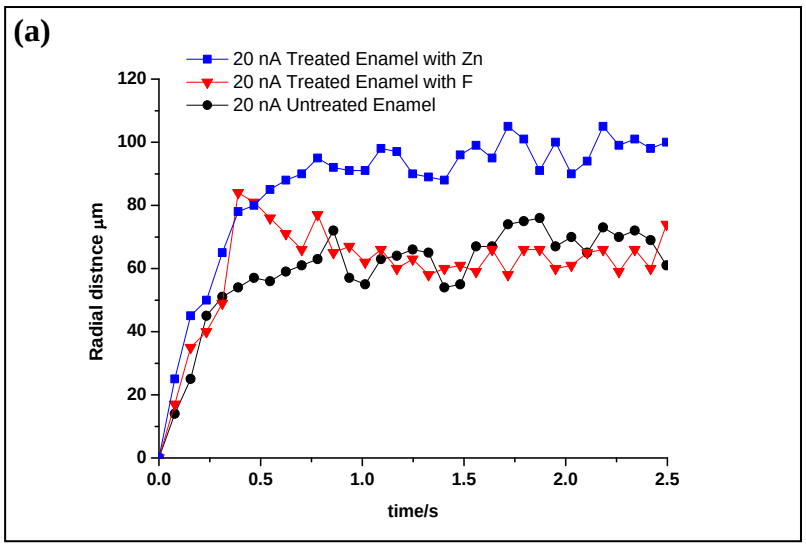

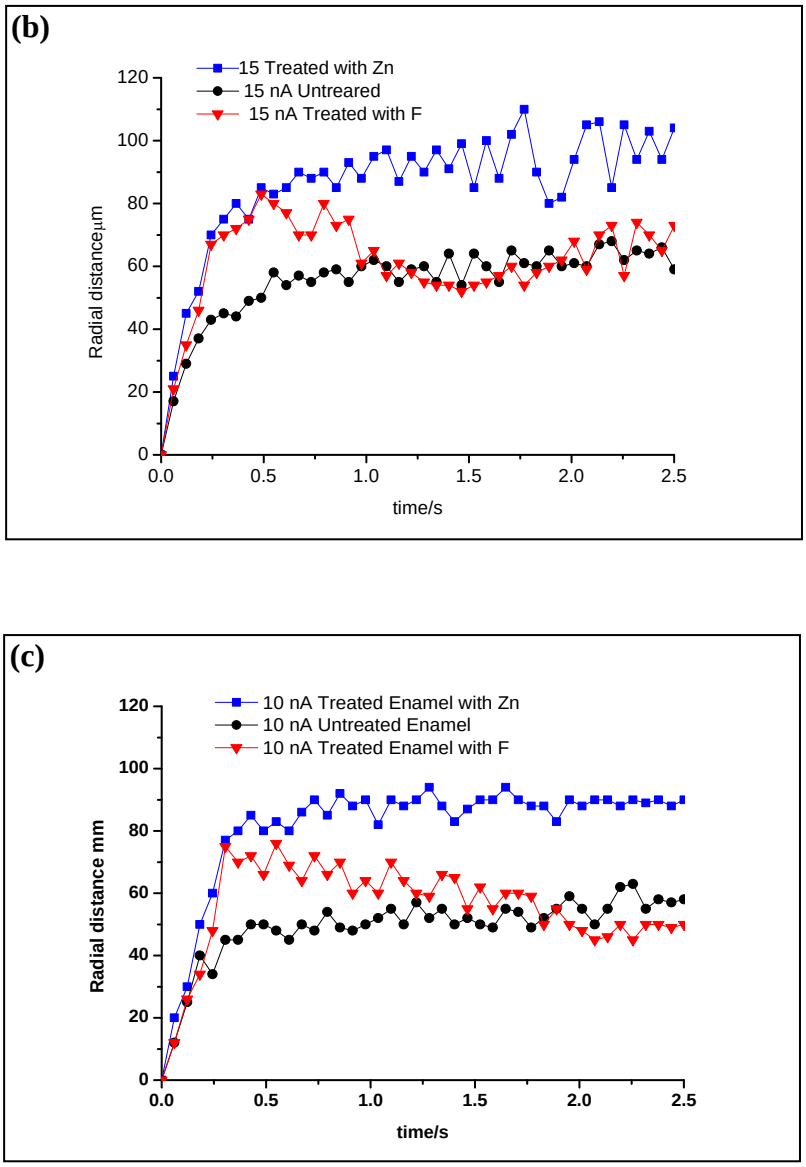

Figure 4.7: Radial distance-time profile of the distance dependence of the pH 6.1 front in a thin layer of aqueous solution following the oxidation of water at a 25 μm diameter Pt UME, positioned 20 μm away from untreated enamel (black squares, black line), fluoride-treated enamel (red circles, red line) and zinc-treated enamel (blue triangles, blue line). Current applied: Current applied: (a) 20 nA , (b) 15 nA and (c) 10 nA.

The proton profile with fluoride is interesting because spreads initially to 85 which last for only ca. 1 s then the profile is less extensive. This indicates the fluoride barrier is only temporary and is eroded quickly with proton uptake becoming comparable to that

of untreated enamel. Thus fluoride provides only a temporary protection toward acid attack. Further evidence for this action of fluoride as protective is evident in Figure 4.7 (b) and (c) where lower proton fluxes are used. It can be seen that for decreasing current (proton flux) the fluoride barrier lasts longer. Interestingly, one of the significant outcomes of the studies reported here is that F^- is able to provide only a very temporary barrier, whereas in case of zinc the spread of proton traveled a larges radial distance and lasts longer time, indicating the surface is considerably less active and less susceptible to interaction with protons.

4.4. Finite Element Model

The geometry for the finite element model developed, which included a moving boundary (etch pit, but this was not used) is shown in Figure 4.8. The model was run under specific conditions corresponding to those used experimentally. The simulation domain is shown in Figure 4.8. The boundary conditions are listed in Table 4.1 and the numbers represent the boundaries referred to in Figure 4.8 when defining boundary conditions. Edge 2 represents the shape of the substrate geometry at the initial time and after simulation of acid etching for some time. The labels used to characterize the geometry are: *a*, the radius of the metallic portion of the disk electrode; *RG* is the ratio of the radius of the entire probe to that of the wire; and *h* is the distance between tip and substrate prior to etching.

Numerical simulations were performed on a Dell Intel Core 2 Duo 2.53 GHz computer equipped with 8 GB of RAM and running Windows XP Professional 64 Bit 2002 edition. Modeling was performed using the commercial finite element package Comsol Multiphysics 3.5a (Comsol AB, Sweden), using the Matlab interface (Release 2009a)

(MathWorks Inc., Cambridge, UK). Simulations were typically carried out with ca. 13,000 triangular mesh elements, with a finer mesh in the vicinity of the electrode and etch pit. Simulations were performed with finer meshes (not reported) to confirm the mesh was sufficiently fine as to not adversely affect the accuracy of the calculations.

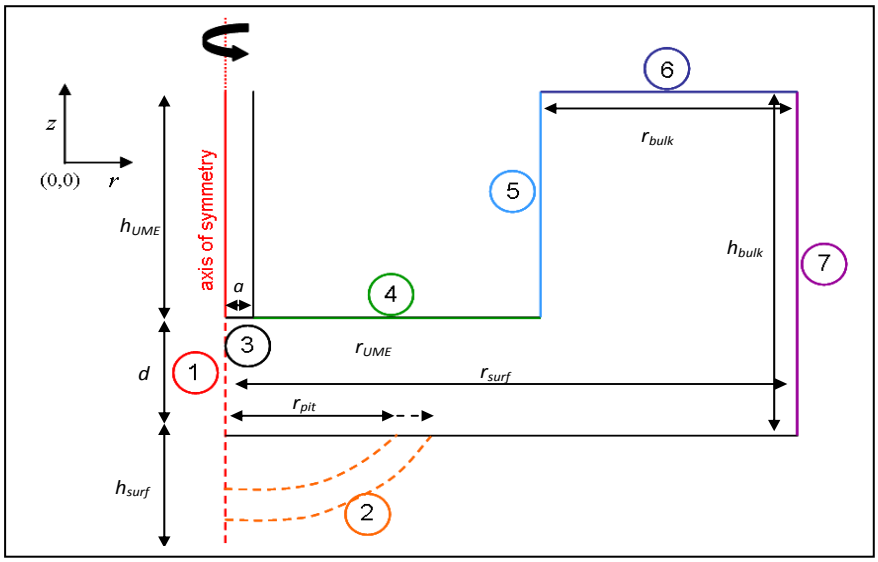

Figure 4.8: Simulation domain for the axisymmetric cylindrical geometry used to model the formation of etch pits in dental enamel.

The finite element model produces a concentration map of all the relevant species as a function of time based upon a moving boundary approach in which dissolution rate constants (supply by the user) describe the first-order heterogeneous attack of protons (equation 4.1.) The following system is considered: the initially flat surface of the enamel sample is dissolved by protons generated from the UME positioned directly above the surface, with the axis of the probe normal to the surface (Figure 4.8). The surface is dissolved following the overall reaction, equation 4.1.

The model assumes that there is a uniform flux, *j*, of protons at the electrode surface,

$$j = \frac{I}{nFA} \tag{4.6}$$

where *I* is the applied current, *n* the number of electrons transferred, *F* is Faraday's constant and *A* the area of the electrode. This has been shown to be reasonable in many previous studies. [21]

The equation solved on the interior of the domain illustrated in Figure 4.8 is the time-dependent reaction diffusion equation cast in axisymmetric coordinates (equation 4.7):

$$\frac{\partial C_i}{\partial t} = D_i \nabla^2 C_i + R_i \tag{4.7}$$

where *i* is the species under consideration (H^+, $H_nPO_4^{3-n}$), and C_i represents the concentration of species *i*, Ca^{2+}, H^+, OH^-, HPO_4^{2-}, $H_2PO_4^-$, H_3PO_4, Ca^{2+}, or the ion pairs and [Ca^{2+} $H_2PO_4^-$]. D_i represents the diffusion coefficient of species *i*, and R_i is the net production of species *i* via equilibrium reactions (ie amount of *i* produced – amount of *i* used up).

In Table 4.1, the geometric quantities h_{surf}, d, h_{UME}, r_{UME}, a, r_{pit}, and r_{surf} represent the height of the surface, the UME-surface separation, the height of the UME, the radius of the active UME microwire, the radius of the etch pit and the radius of the surface respectively. Boundaries 6 and 7 were set at a sufficient distance from the region of interest so as to obtain a good solution.

Table 4.1: Boundary conditions for finite element modeling.

Boundary Description	Number in Figure 4.8	Coordinates	Equation
Axis of symmetry (fixed in *r* but free in *z*)	1	$r=0$ $(h_{surf}+d+h_{UME})>z>0$	$0=\nabla C\cdot \underline{n}$
Solution/enamel interface (moving)	2	$r = r_{pit}$ $z = h_{surf}$	For H^+: $kC_{H^+} = D_{H^+}\nabla C_{H^+}\cdot \underline{n}$ For $H_2PO_4^-$: $k\frac{6}{8}C_{H^+} = -D_{H_2PO_4^-}\nabla C_{H_2PO_4^-}$ For HPO_4^{2-} and H_3PO_4: $0=\nabla C\cdot \underline{n}$
Solution/active electrode interface (fixed)	3	$r=a$ $z = h_{surf} + d$	For H^+: $D_{H^+}\frac{\partial C_{H^+}}{\partial z} = \frac{i}{F\cdot area}$ For $H_nPO_4^{3-n}$: $0=\nabla C_i\cdot \underline{n}$
Solution/insulator interface (fixed)	4 & 5	$r = r_{UME}$ **For 4**: $z = h_{surf} + d$ **For 5**: $z = h_{surf} + d + h_{UME}$	$0=\nabla C_i\cdot \underline{n}$
Bulk solution (fixed)	6	$r = r_{surf}$ $z = h_{surf} + d + h_{UME}$	For H^+: $C^{H+} = 10^{-pHbulk}$ For $H_nPO_4^{3-n}$: $C_i = 0$
Bulk solution (fixed in *r* but free in *z*)	**7**	$\boldsymbol{r = r_{surf}}$ $\boldsymbol{z = h_{surf} + d + h_{UME}}$	For H^+: $C^{H+} = 10^{-pHbulk}$ For $H_nPO_4^{3-n}$: $C_i = 0$

4.4.1 Diffusion Coefficients

The following set of equations describes all possible equilibria for the numerical model:[52]

$$HPO_4^{2-} \rightleftharpoons PO_4^{3-} + H^+ \qquad pK_a = 12.32 \qquad (4.8)$$

$$H_2PO_4^- \rightleftharpoons HPO_4^{2-} + H^+ \qquad pK_a = 7.21 \qquad (4.9)$$

$$H_3PO_4 \rightleftharpoons H_2PO_4^- + H^+ \qquad pK_a = 2.16 \qquad (4.10)$$

$$[Ca^{2+}OH^-] \rightleftharpoons Ca^{2+} + OH^- \qquad pK_{eq} = 1.29 \qquad (4.11)$$

$$H_2O \rightleftharpoons OH^- + H^+ \qquad pK_w = 14 \qquad (4.12)$$

$$[Ca^{2+}PO_4^{3-}] \rightleftharpoons Ca^{2+} + PO_4^{3-} \qquad pK_{eq} = 6.42 \qquad (4.13)$$

$$[Ca^{2+}HPO_4^{2-}] \rightleftharpoons Ca^{2+} + HPO_4^{2-} \qquad pK_{eq} = 2.64 \qquad (4.14)$$

$$[Ca^{2+}HPO_4^-] \rightleftharpoons Ca^{2+} + H_2PO_4^- \qquad pK_{eq} = 1.34 \qquad (4.15)$$

The pK_a of equation 4.8 is so high that at the pH range we are working within (pH < 7) there is no need to consider this reaction, thus the fully deprotonated PO_4^{3-} species was not modelled. Similarly, the pH range of interest and pK_{eq} value of equation 4.11 dictates that the equilibrium will be all the way to the right and thus the ion pair [Ca^{2+} OH^-] is not considered. Equation 4.13 was also disregarded as PO_4^{3-} need not be considered (*vide supra).* The pKa values of all species were corrected for ionic activity with the Davies equation [53-54] given the presence of 0.1 M $NaNO_3$. The influence of the protonation / deprotonation state of fluorescein was found to have no significant effect on the results due to the very low concentration of that species (µm) and was therefore ignored in the calculations. The diffusion coefficients used in the model are given in Table 4.2.[55]

Table 4.2: Diffusion coefficients of all species considered in the model in units of cm^2 s^{-1}.

Species	Diffusion Coefficeint / cm^2 s^{-1}
D_{H^+}	7.60 x 10^{-5}
D_{OH^-}	5.00 x 10^{-5}
$D_{Ca^{2+}}$	7.92 x 10^{-6}
$D_{\{Ca^{2+}HPO_4^{2-}\}}$	1.00 x 10^{-5}
$D_{\{Ca^{2+}H_2PO_4^{-}\}}$	1.00 x 10^{-5}
$D_{H_3PO_4}$	8.24 x 10^{-6}
$D_{H_2PO_4^-}$	8.24 x 10^{-6}
$D_{HPO_4^{2-}}$	8.24 x 10^{-6}

We set the diffusion coefficients of any ion pairs to 1.0 x 10^{-5} cm^2 s^{-1}, which is a typical value for entities of this size,[55-56] because such species play a minor role the simulations were relatively insensitive to the magnitude of these diffusion coefficients. The most important diffusion coefficient is that for H^+ which drives the dissolution process and for which we have highly accurate values.

4.4.2. Insights from Simulations

The finite element model produces pH profiles as a function of time for rate constants of dissolution for untreated and treated enamel. The fluorescence intensity (I) map was calculated from the model output (pH profile) via the calibration curve discussed above. Time resolved dissolution kinetics rates were extracted by matching the experimental intensity data to the numerical solutions. The model produces pH profiles as a function of time for rate constants of dissolution for untreated and treated enamel. These theoretical data were also used to plot radial distance from the electrode centre, against time, for a specific proton concentration.

Figures 4.9 shows the displacements of 50% intensity profiles measured experimentally at untreated, fluoride treated and zinc treated enamel respectively for a current of 20 nA, fitted by the modelled displacement for the 50 % light intensity described earlier with rate constant (in the range 0.001-1 cm s^{-1}). It can be seen that the 50% intensity expands with time, as expected for a proton induced dissolution process, such that these profiles travel less radial distance with increasing K_{vert}. This is because a larger rate constant leads to greater consumption of protons at the substrate surface. Therefore, as can be seen in cases of treated samples, the presence of the inhibitors significantly retards the rate of enamel dissolution. This has slowed considerably from 0.2 cm s^{-1} for untreated enamel, down to 0.03 cm s^{-1} for Zn treated enamel and between 0.02 cm s^{-1} cm s^{-1} and 0.05 cm s^{-1} for 1000 ppm NaF treated enamel at short time.

Figure 4.9 (a) shows indicative results from the matching of experimental and simulated fluorescence profiles next to untreated enamel with a rate constant of dissolution between 0.08 and 1 cm s^{-1}, averaging at 0.2 cm s^{-1} with an averaged proton spread of 66

µm for untreated enamel. It can be seen that the experimental 50% intensity profiles and the simulation are generally in good agreement. A minor discrepancy is that the profile of the experimental is slightly lower than predicted by theory at short time, before 0.2 s. The consistency of this behaviour across a number of profiles and for a range of currents gives confidence that the factor that could influence this is the possible surface processes which are not related to dissolution. This can be related due to polishing the surface before performing the experiment, as this is consistent with all experiment performed herein.

Figure 4.9 (b) shows the initial layer of fluoride protecting the surface by allowing the protons to spread out to 84 µm, equivalent to the closest match for the vertical rate constant k_{vert} between 0.02 cm s^{-1} and 0.05 cm s^{-1}. Treating the surface with fluoride increases the proton spread on the surface and considerably slows the rate of dissolution, however this protection only lasts up to c.a. 1 second after which the proton spread averages 67 µm and a rate constant match comparable to untreated enamel of 0.2 cm s^{-1}. Figure 4.9 (c) details the rate constant of dissolution for zinc treated enamel to be 0.03 cm s^{-1}, interestingly this rate is in the range of the initial protection from fluoride treatment however the overall proton spread for zinc treatment averages at 103 µm. That is the largest proton spread we have encountered and is suggestive of a surface that is considerably less active.

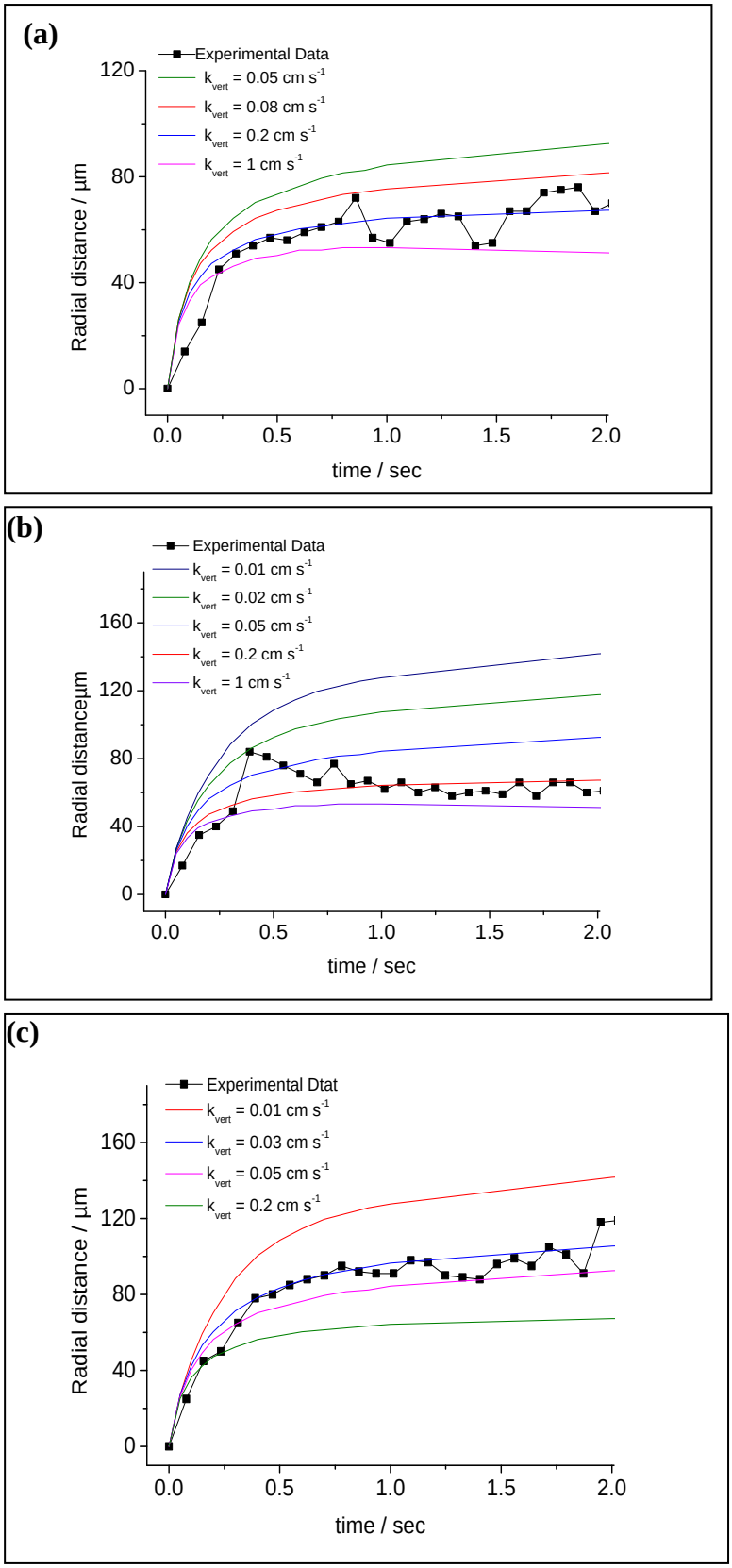

Figure 4.9: Radial distance-time profile of the distance dependence of the pH 6.1 front in a thin layer of aqueous solution following the oxidation of water at a 25 µm diameter Pt UME, matched to their respective rate constants were the experimental data is shown

as black squares and (a) is untreated enamel (b) is the fluoride treated enamel (c) is the zinc treated enamel. Current applied: 20 nA.

As mentioned previously, all experiments were carried out at three currents, 20 nA, 15 nA and 10 nA. For all currents applied, the rate of lateral diffusion was faster at an untreated, than at fluoride treated and zinc treated enamel. The details of the averaged rate constant and distance that the protons spread at 50 % intensity (pH 6.1) is given in Table 4.3 for the three different surfaces at the three different rate constants. The rate constant data for fluoride is expressed as the slowest rate at the peak to the average rate after 1 second, this is also true of the distance of proton spread data. It is clear from the table that the lower the current is, the higher the pH which leads to longer protection time of fluoride.

Table 4.3: Proton distribution (50 % intensity; pH 6.1) and rate constant match for each of the three currents, 10, 15 and 20 nA over the three different surfaces and after 4 s.

Current used nA	Surface Treatment	Proton Spread / µm	Rate Constant / cm s^{-1}
10	Untreated	57	0.3
10	Fluoride	75 - 60	0.02 - 0.08
10	Zinc	87	0.03
15	Untreated	61	0.3
15	Fluoride	83 - 65	0.03 - 1
15	Zinc	96	0.03
20	Untreated	66	0.2
20	Fluoride	84 - 67	0.02 - 0.2
20	Zinc	103	0.03

4.5. Amount of Zinc and Fluoride Uptake on Treated Enamel

It was shown above that fluoride provided only a very temporary barrier, whereas Zn^{2+} treatment results in a more permanent barrier. It is thus important to elucidate why there is this difference and elucidate how much Zn^{2+} and F^- is taken up by enamel due to these treatments. When treating the enamel sample with 5 ml of 10 mM $ZnCl_2$, 0.183 ppm (2.798×10^{-6} mol L^{-1}) of Zn^{2+} was found absorbed (measured using inductively coupled plasma mass spectrometry, ICP-MS). Thus, the total amount of Zn^{2+} absorbed by the enamel sample in the area exposed to the solution of 4.57×10^{-4} m^2 was calculated to be 1.4×10^{-8} mol. In order to equate the amount of zinc take up to an overall depth of penetration, the molar volume *MV* was calculated:

$$MV = \frac{MM}{\rho} \qquad (4.14)$$

where *MM* is the molar mass of enamel (1004 g mol^{-1}) [57] and ρ is the density of enamel (28000 g m^{-3}). This gave the molar volume as $3.58 \times 10^{-4} m^{-3} mol^{-1}$. Taking account of 10 Ca^{2+} in each HA can be exchanged with zinc, as per equation 1.1. The molar volume is multiplied by the total amount absorbed on enamel sample 1.4×10^{-8} mol and divided by the surface area 0.00457 m^2 to give an overall depth of penetration of 1.1×10^{-5} m for pre-treatment with 10 mM.

Interestingly when treating an enamel sample with 26 mM NaF, only 92 ppm (4.843×10^{-3} mol L^{-1}) is actually absorbed (measured using a fluoride ion selective electrode (FISE)). The overall depth of penetration of 1.8×10^{-3} m was calculated for pre-treatment with 26 mM for enamel disc sample of diameter of ca. 6.76×10^{-3} m as detailed in previous work.[56] Even though the overall depth of penetration of zinc is less than fluoride, this suggests that the zinc substitution forms a more stable molecule which is better at resisting acid attack, in comparison to untreated or fluoride treated

enamel. Zinc is known to be readily taken up by HA and competes with calcium ion (facilitated by the similarities in ionic size between zinc and calcium) for surface positions on the crystals surface. Zinc can substitute in for calcium in the apatite lattice and form zinc hydroxyapatite matrix and this formation of zinc apatite is proving to be more resistant to acid attack than the fluoride substituted hydroxides in the enamel matrix, commonly known as fluroapatite.[57]

4.6. Conclusions

SECM has been successfully combined with CLSM to image proton diffusion in a thin layer of solution at the surface of enamel. This new technique provides an analytical method with high spatial and temporal resolution permitting sub-second analysis of treatment effects on enamel substrates. It permits direct visualisation of the surface reaction and presents itself as a new technique for assessing the proton dispersion on surfaces and indeed for assessing the effectiveness of inhibitors on substrates. The method developed uses microelectrode generated pH challenges combined with CLSM to image proton diffusion and dissolution at the surface of enamel. Specially, localised dissolution of dental enamel has been achieved by the application of a proton flux to the enamel surface from a UME positioned in close proximity to the enamel surface. It has been shown that fluoride and zinc change the morphology of the fluorescent profile that forms compared to untreated enamel, due to their barrier effect, in which they protect enamel to same extent.

Modelling of the data using the theoretical finite element model Comsol has indicated that acid erosion does occur at both untreated and treated enamel surfaces, but in the treated cases this is slower than the rate of dissolution at untreated enamel. Rate

constants of dissolution were assigned for each of the three different surface treatments at the three different currents of 10, 15 and 20 nA. Zinc treated enamel proved itself to provide a more resistant barrier to proton attack than the fluoride treatment, even though the surface concentration and depth of penetration of fluoride in enamel was much more extensive than that of Zn^{2+}. Fluoride showed itself to be an initial barrier to proton with rate constant similar to zinc, however this barrier only lasted for approximately one second for the range of quite high proton fluxes applied, before returning to a rate comparable to that of untreated enamel. This suggests that zinc substitution into the HA matrix creates a strong material, presumably zinc apatite, which is more resistive to proton attack than fluoride treated enamel. These experiments broaden the potential applications of CLSM in assessing the proton dispersion on surfaces and indeed for assessing the effectiveness of inhibitors on substrates.

4.7. References

(1) Hulsken, B.; Van Hameren, R.; Gerritsen, J. W.; Khoury, T.; Thordarson, P.; Crossley, M. J.; Rowan, A. E.; Nolte, R. J. M.; Elemans, J. A. A. W.; Speller, S. *Nature Nanotechnology* **2007**, *2*, 285.
(2) Elemans, J. A. A. W. *Materials Today* **2009**, *12*, 34.
(3) Pidaparti, R.; Neblett, E.; Miller, S.; Alvarez, J. *Smart. Mater. Struct.* **2008**, *17*.
(4) Lillard, R. S.; Willcutt, G. J.; Pile, D. L.; Butt, D. P. *Journal of Nuclear Materials* **2000**, *277*, 250.
(5) Lillard, S.; Gac, F.; Paciotti, M.; Ferguson, P.; Willcutt, G.; Chandler, G.; Daemen, L. In *Effects of Radiation on Materials: 20th International Symposium*; Rosinski, S. T. G. M. L. A. T. R. K. A. S., Ed. 2001; Vol. 1045, p 631.
(6) Kreuer, K. D. *Chemistry of Materials* **1996**, *8*, 610.
(7) Wu, H. P.; McCreery, R. L. *Analytical Chemistry* **1989**, *61*, 2347.
(8) McGeouch, C.-A.; Edwards, M. A.; Mbogoro, M. M.; Parkinson, C.; Unwin, P. R. *Analytical Chemistry* **2010**, *82*, 9322.
(9) Bengtsson, A.; Sjoberg, S. *Pure and Applied Chemistry* **2009**, *81*, 1569.
(10) Abou-Hassan, A.; Dufreche, J. F.; Sandre, O.; Meriguet, G.; Bernard, O.; Cabuil, V. *Journal of Physical Chemistry C* **2009**, *113*, 18097.
(11) Amatore, C.; Pebay, C.; Servant, L.; Sojic, N.; Szunerits, S.; Thouin, L. *Chemphyschem* **2006**, *7*, 1322.
(12) Compton, R. G.; Unwin, P. R. *Journal of Electroanalytical Chemistry* **1986**, *205*, 1.
(13) Snowden, M. E.; Unwin, P. R.; Macpherson, J. V. *Electrochemistry Communications* **2011**, *13*, 186.
(14) Mbogoro, M. M.; Snowden, M. E.; Edwards, M. A.; Peruffo, M.; Unwin, P. R. *Journal of Physical Chemistry C* **2011**, *115*, 10147.
(15) Snowden, M. E.; King, P. H.; Covington, J. A.; Macpherson, J. V.; Unwin, P. R. *Analytical Chemistry* **2010**, *82*, 3124.
(16) Newman, I. A. *Plant. Cell. Environ.* **2001**, *24*, 1.
(17) Shellis, R. P.; Finke, M.; Eisenburger, M.; Parker, D. M.; Addy, M. *European Journal of Oral Sciences* **2005**, *113*, 232.
(18) Shabala, L.; Roos, T.; McMeekin, T. *Microbiol. Aus.* **2004**.
(19) Pawley, J. *Handbook of Biological Confocal Microscopy*; 3rd ed.; Springer: Winconsin, 2006.
(20) Grime, J. M. A.; Edwards, M. A.; Rudd, N. C.; Unwin, P. R. *Proceedings of the National Academy of Sciences of the United States of America* **2008**, *105*, 14277.
(21) Rudd, N. C.; Cannan, S.; Bitziou, E.; Ciani, L.; Whitworth, A. L.; Unwin, P. R. *Analytical Chemistry* **2005**, *77*, 6205.
(22) Cannan, S.; Macklam, I. D.; Unwin, P. R. *Electrochemistry Communications* **2002**, *4*, 886.
(23) Macpherson, J. V.; Unwin, P. R. *Journal of Physical Chemistry* **1994**, *98*, 11764.
(24) Macpherson, J. V.; Unwin, P. R. *Journal of Physical Chemistry* **1994**, *98*, 1704.
(25) Macpherson, J. V.; Unwin, P. R. *Journal of Physical Chemistry* **1995**, *99*, 14824.
(26) Macpherson, J. V.; Unwin, P. R. *Progress in Reaction Kinetics and Mechanism* **1995**, *20*, 185.
(27) Macpherson, J. V.; Unwin, P. R. *Journal of Physical Chemistry* **1996**, *100*, 19475.
(28) McKelvey, K.; Edwards, M. A.; Unwin, P. R. *Analytical Chemistry* **2010**, *82*, 6334.

(29) Hjortsjo, C.; Jonski, G.; Thrane, P. S.; Saxegaard, E.; Young, A. *Caries Research* **2009**, *43*, 449.
(30) Heurich, E.; Beyer, M.; Jandt, K. D.; Reichert, J.; Herold, V.; Schnabelrauch, M.; Sigusch, B. W. *Dental Materials* **2010**, *26*, 326.
(31) Sonju Clasen, A. B.; Ogaard, B.; Duschner, H.; Ruben, J.; Arends, J.; Sonju, T. *Advances in dental research* **1997**, *11*, 442.
(32) Radlanski, R. J.; Renz, H.; Willersinn, U.; Cordis, C. A.; Duschner, H. *European Journal of Oral Sciences* **2001**, *109*, 409.
(33) Williams, C. G.; Macpherson, J. V.; Unwin, P. R.; Parkinson, C. *Analytical Sciences* **2008**, *24*, 437.
(34) Margolis, H. C.; Zhang, Y. P.; Lee, C. Y.; Kent, R. L.; Moreno, E. C. *Journal of Dental Research* **1999**, *78*, 1326.
(35) Mahoney, E. K.; Kilpatrick, N. M. *New Zealand Dental Journal* **2003**, *99*, 33.
(36) Davis, R. E.; Marshall, T. A.; Qian, F.; Warren, J. J.; Wefel, J. S. *Journal of the American Dental Association* **2007**, *138*, 1593.
(37) Wongkhantee, S.; Patanapiradej, V.; Maneenut, C.; Tantbirojn, D. *Journal of Dentistry* **2006**, *34*, 214.
(38) Rubinstein, E.; Hauge, C.; Sommer, P.; Mortensen, T. *Pharmacology & Toxicology* **1993**, *72*, 61.
(39) Cheng, Z. J.; Wang, X. M.; Cui, F. Z.; Ge, J.; Yan, J. X. *Biomedical Materials* **2009**, *4*.
(40) Attin, T.; Becker, K.; Hannig, C.; Buchalla, W.; Hilgers, R. *Caries Research* **2005**, *39*, 432.
(41) Wang, L. J.; Tang, R. K.; Bonstein, T.; Orme, C. A.; Bush, P. J.; Nancollas, G. H. *Journal of Physical Chemistry B* **2005**, *109*, 999.
(42) Barbour, M. E.; Parker, D. M.; Allen, G. C.; Jandt, K. D. *European Journal of Oral Sciences* **2003**, *111*, 428.
(43) Barbour, M. E.; Parker, D. M.; Jandt, K. D. *Journal of Colloid and Interface Science* **2003**, *265*, 9.
(44) Amjad, Z.; Koutsoukos, P. G.; Nancollas, G. H. *Journal of Dental Research* **1981**, *60*, 450.
(45) LeGeros, R. Z. *Journal of Dental Research* **1990**, *69 Spec No*, 567.
(46) Hannig, C.; Hamkens, A.; Becker, K.; Attin, R.; Attin, T. *Archives of Oral Biology* **2005**, *50*, 541.
(47) Duschner, H.; Gotz, H.; Ogaard, B. *European Journal of Oral Sciences* **1997**, *105*, 466.
(48) Tanaka, M.; Moreno, E. C.; Margolis, H. C. *Archives of Oral Biology* **1993**, *38*, 863.
(49) Ten Cate, J. M. *Acta Odontologica Scandinavica* **1999**, *57*, 325.
(50) Unwin, P. R.; Macpherson, J. V.; Martin, R. D.; McConville, C. F. *Electrochem. Soc.* **2000**, *99*, 104.
(51) Harnad, H. S. O., W. *The Physical Chemistry of Electrolytic Solutions*; Reinhold Publishing Corp: New York, 1950.
(52) Bjerrum, J.; Schwarzenbach, G.; Siller, L. G. In *The Chemical Society* London, 1957.
(53) Grime, J. M. A.; Edwards, M. A.; Rudd, N. C.; Unwin, P. R. *P. Natl. Acad. Sci. USA.* **2008**, *105*, 14277.
(54) Davies, C. W. *Ion Association*; Butterworths, London.
(55) *CRC Handbook of Chemistry and Physics, 89th ed.*; CRC Press, 2008.

(56) Medvedev, E. S.; Stuchebrukhov, A. A. *Journal of Physics-Condensed Matter* **2011**, *23*.
(57) Weidmann, S. M.; Weatherell, J. A.; Hamm, S. M. *Arch. Oral. Biol.* **1967**, *12*, 85.

Combined Confocal Laser Scanning Microscopy - Electrochemical Techniques for the Investigation of Lateral Diffusion of Protons at Surfaces

Introduction

In this chapter a new method combining SECM and CLSM has been developed to study the lateral diffusion of protons at modified surfaces. A Pt UME positioned close to an interface, has been used to locally change the pH, via the oxidation of water, building on the studies in Chapter 4. The interfacial proton diffusion has been imaged by CLSM at interfaces different compositions of phospholipid bilayers. A comparison is made of bilayers comprising either zwitterionic phosphatidyl choline (EPC) and mixtures with different ratios of EPC and acidic distearoyl phosphatidylglycerol 1,2-ditetradecanoyl-sn-glycero-3-phospho-(1'-rac-glycerol) (DSPG). A range of different currents have been applied at the SECM tip to generate different local proton fluxes. The technique proved very useful method for studying lateral proton diffusion at these model biological membranes systems with high spatial and temporal resolution allowing sub-second analysis of the effect of ionisable groups on the membrane.

5.1. Biological Membranes

The cell membrane plays a critical role in many biological processes like protein folding,[1] cell-cell communication and interaction,[2] cell signaling,[3-4] enzymatic reactions occurring at the cell surface[5] and energy transduction[6]. Biological membranes form the boundary between cells and their environment. They form a selectively permeable barrier due to the presence of specific channels, gates and pumps and thus regulate the contents of the cell.[7-8] They also enclose cell organelles (such as mitochondria and chloroplasts) and many important reactions, including respiration and photosynthesis, take place on such membranes.[9] It is an essential function of the membrane that it is not just an encapsulating permeability barrier, but makes up a dynamic boundary through which e.g. signals can be transmitted, nutrients imported and water/harmful product

exported. It took nearly 100 years to uncover the structure of the cell membrane as it is now understood. In 1972, the fluid mosaic model was proposed and it is now accepted as the basis of our understanding of cell membranes.[10] It suggests that the lipids form a viscous, two-dimensional solvent into which proteins are inserted and integrated.[10] The phospholipid molecules constantly diffuse laterally within the membrane and membrane proteins are free to diffuse laterally too, assuming that no specific interactions hold them in place, such as attachment to the cell's cytoskeleton. It is important to note that the composition of a lipid bilayer is typically heterogeneous in biological systems; many different lipids are present.[11-13]

Membrane lipids are amphipathic molecules with hydrophilic head groups and hydrophobic acyl chains (Figure 5.1) that self-assemble in aqueous environments due to the hydrophobic effect.[10] In bilayers the hydrophilic parts make up an interface towards the aqueous environment, shielding off the hydrophobic part. The thickness of the hydrophobic part of the membrane is usually 25-30 Å. There is a considerable structural variation in the hydrophobic part of bilayers, such as the acyl chain length, degree of saturation, branching of chains and linkage between the chain and head group, features that all affect the fluidity in the bilayer. The fatty chains in phospholipids and glycolipids usually contain an even number of carbon atoms, typically between 16 and 20. Fatty acids may be saturated or unsaturated, with the configuration of the double bonds nearly always cis. The length and the degree of unsaturation of fatty acid chains have a profound effect on membranes fluidity.[7-8] It is not only the acyl chain region that influences the bilayer. Lipid head groups have different net charges at physiological pH and different ability to form hydrogen bonds.

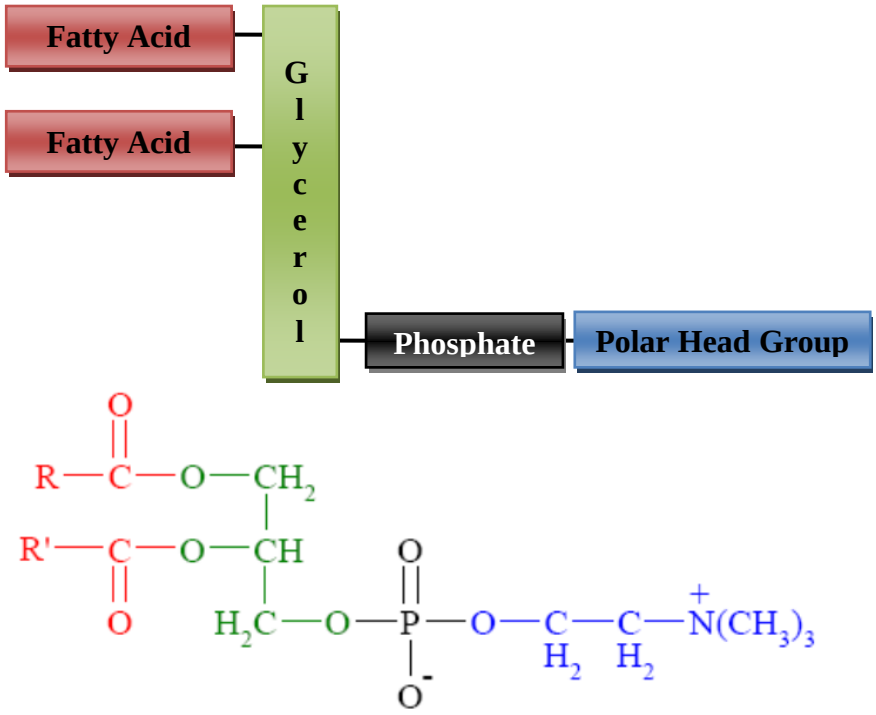

Figure 5.1: (a) A schematic representation of a phosphoglyceride (b) The molecular structures of (b) phosphatidylcholine where R and R' are fatty acid chains.[7]

As the name suggests, the lipid bilayer is two layers of lipid molecules sandwiched together as shown in Figure 5.2. When lipid molecules are placed in aqueous solution they self-assemble into structures that minimise the repulsive interactions between the hydrophobic tails and the aqueous phase, as shown in Figure 5.3. For example, bilayers form in aqueous solution when the phospholipids arrange themselves so that the polar head groups form two layers, with the alkyl tails associating only with other alkyl chains between these layers.[14-15] These are often in the form of vesicles, known as liposomes, where the bilayer curves round in a sphere, preventing the interaction of water molecules with the hydrophobic tails. Monolayers is another lipid aggregation, form when these molecules align at an air/water interface or an oil/water interface.[14] The hydrophilic heads remain in the aqueous phase and the hydrophobic tails are oriented away from the aqueous medium into the gaseous or organic phase.

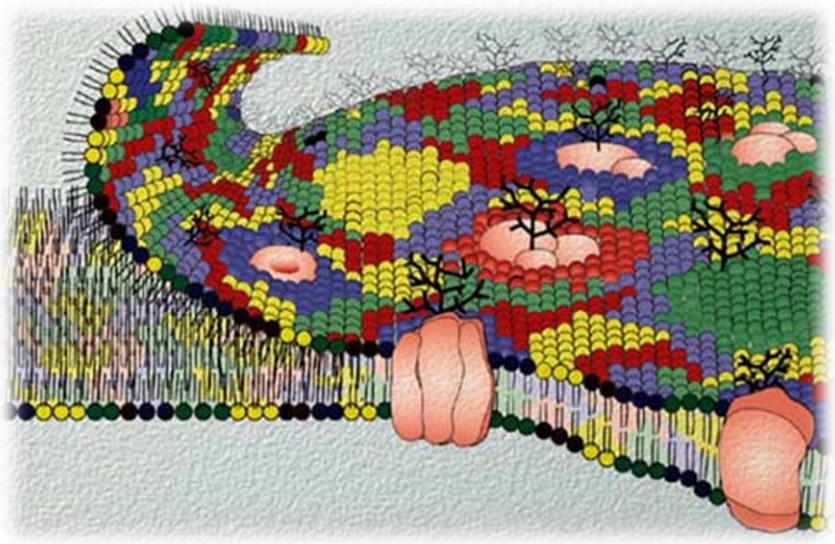

Figure 5.2: A molecular view of the cell membrane, Different phospholipids are indicated by different coloured head groups. Picture taken from [13]

The arrangement of hydrophilic heads and hydrophopic tails of the lipid bilayer prevents polar solutes (e.g. amino acids, nucleic acids, carbohydrates, proteins, and ions) from diffusing across the membrane, but generally allows for the passive diffusion of hydrophobic molecules[15-16] The head group is also variable. Since the phosphate group is negatively charged, the addition of a polar moiety can either produce a neutral, zwitterionic head group (as in the case of phosphatidylcholine and phosphatidylethanolamine), or a charged head group (as in the case of phosphatidylserine, which is anionic). A wide variety of phospholipids form part of cell membranes, as can be seen in Figure 5.2

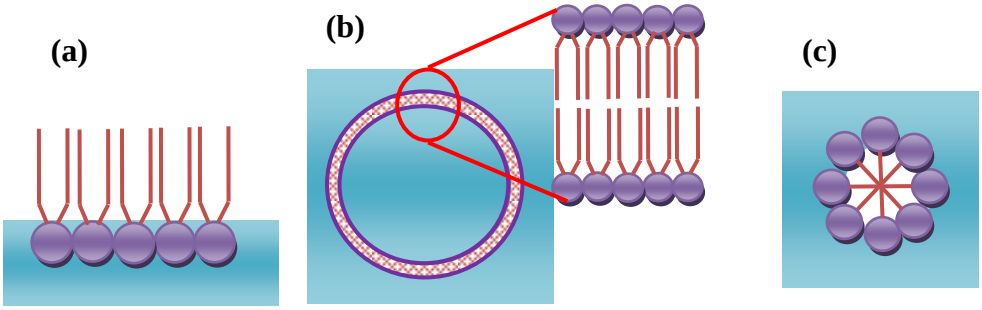

Figure 5.3: Lipid aggregation: (a) monolayer formed at the air/water or oil/water interface; (b) vesicle formed in aqueous solution (spherical bilayer); (c) micelle formed by single-tailed lipids.[8]

Due to the complex nature and variable composition of biological membranes, simplified models such as pure phospholipid monolayers or bilayers (both planar and in the form of vesicles) are used to investigate the physical and chemical properties. Clearly, these will not exhibit exactly the same characteristics as cell membranes since the presence of proteins and the asymmetric nature of the cell membrane will not be taken into account. However, these systems can be much more easily regulated and controlled and form a good starting point from which more complex studies, perhaps including the incorporation of protein molecules or cholesterol, can be based. The studies described in this chapter focuse on the use of supported planar bilayer lipid membranes with different head groups to investigate their influence on proton lateral diffusion.

5.2. Supported Lipid Bilayer (SLB) Synthesis and Characterisation

Investigations of vesicle formation and the properties of supported lipid bilayer is gaining increased attention and importance, as they represent the simplest model for

studying biological processes and characteristics of cell membranes. Studies carried out on planar bilayer formation have established many procedures to obtain either mono- or bilayers assemblies. These procedures involve the "brush" technique, the "dipping" technique[17] and the "patch clamp" method[18] for unsupported bilayer formation. The most popular methods used for supported lipid bilayer formation are Langmuir-Blodgett/Langmuir-Schaeffer[19-20] and the vesicles fusion techniques. The fluidity of the solid supported system is maintained by trapping a water layer (10-20 Å) between the substrate and the SLB.[5,21]

The principal method forming SLBs is the vesicle fusion method (which this study focuses on). Under certain conditions, small unilamellar vesicles (SUVs) of phospholipids in solution may adsorb on the surface of a solid substrate and subsequently rupture (either spontaneously or after reaching a critical surface coverage). The interest in this method arises from its simplicity and because it is fairly straightforward to integrate membrane proteins into the bilayers by preparing proteoliposomes.[3,6,22] However, the drawback of this method is its high delicacy, since the size and charge of the vesicles, as well as the charge and morphology of the surface, has great influence on this process due to the electrostatic interactions.[23-24] The pH of the buffer and the temperature also has a huge effect on the process.[22] If the conditions are not correct, the vesicles may adsorb but not rupture leaving a layer of intact vesicles.[25] Considering electrolyte effects, and the ionic strength of the solution, it has been established that the presence of divalent cations in the buffer solution such as calcium or magnesium in very low concentration (ca 2 mM) has an enormous importance and can effectively induce bilayer formation. There are a number of ways to form solutions of SUV including multilaminar extrusion through porous polycarbonate

membrane at high pressure,[26-27] as well as the sonication and ultracentrifugation of aqueous lipids suspensions.[28-29]

Other commonly used methods of forming SLBs include the Langmuir-Blodgett (LB) and Langmuir-Schaeffer (LS) techniques.[30] In *LB* technique, a monolayer is formed at the air/water interface of a Langmuir Trough, by spreading a lipid solution on it. The deposition of the multilayer (or even bilayers) on the substrate is carried out by successively pulling and immersing the substrate up and down vertically through the monolayer.[31] It is also possible to adsorb vesicles to a monolayer created using the Langmuir-Blodgett technique.[32] In the *LS* technique, the solid substrate is lowered parallel to the liquid surface to touch the monolayer. These two techniques (*LB and LS*) allow the formation of asymmetric bilayers and thus the investigation of the lipid structure in the top and bottom leaflets; as well as examination of the complex behaviour of the excess surface area as a function of the composition in two-component bilayers. Less commonly used bilayer formation techniques include spin coating[33-34]and air bubble collapse.

Various techniques have been used to study and follow SLB formation, and a combination of more than one method in the study gives better understanding of the formation mechanism, such as surface plasmon resonance (SPR)[35-36], ellipsometry,[37] fluorescence,[23,25,38] attenuated total reflectance infrared spectroscopy,[30] and quartz crystal microbalance with dissipation (QCM-D).[39-41] One method of forming a lipid bilayer on a flat support, such as silica, is to apply lipid vesicles to the surface. When the lipid vesicles come in contact with the SiO_2-coated QCM-D or SPR quartz sensor crystal surface or the silica prism, they first adsorb to the surface as intact vesicles.

Once a sufficiently high surface coverage is reached they spontaneously transform into a bilayer.[42] Many techniques have been used to investigate bilayers after their formation. Fluorescence recovery after photobleaching (FRAP) has been used extensively to study the mobility and fluidity of the bilayers;[32,36] spatially resolved mass spectrometry to determine lipid distribution in the bilayers;[33] AFM to investigate the topology of the bilayers as well as identifying specific domains in the lipids patches;[34,43] spectroscopic methods are also used such as neutron reflectivity,[44] X-ray scattering[45] and Raman spectroscopy.[46] Herein, tapping mode AFM was used to visualize supported bilayers formed on coverslips.[47]

5.3. Modification of Surfaces by Ultrathin Films

Ultrathin organic films have gained a lot of interest due to their use in many application areas, such as composites, catalysis, microelectronics,[48] integrated optics, sensors, friction reducing coating and surface orientation layers.[49] Three common methods are used in the formation of supported thin films on a solid substrate: the Langmuir-Blodgett technique (see section 5.2 above), chemisorption and self-assembly processes. Chemisorption implements an adsorption method driven by a chemical reaction at the surface of interest: the interaction between the surface, and the generated species creates either ionic or covalent bonds between. While powerful, this shows various drawbacks, such as the need of the reaction to achieve 100% yield to maintain full coverage in each layer. Some species do not permit the assembly of high numbered multilayers and so this method is restricted to limited numbers of organics.[49-50]

The self-assembly process which was firstly developed by Decher et al,[49] this technique has gained increasing attention and interest due to its simplicity and straightforward

formation of the layer with no need for covalent bonds formation or monolayers transfer, as it only involves adsorption from solution. Multilayers are fabricated by sequential anionic-cationic polyelectrolyte addition to the substrate, the mechanism depending on the electrostatic interaction between the species and the substrate surface, which provides the driving force for the build-up of the multilayer, and guarantees full coverage of the required compound as the repulsive force between similar charges prevents any contamination in the layer;[51] another advantage is the ability to insert different materials in the assembled layers such as proteins, biopolymers, virus particles or inorganic colloids.[48]

The two polymers studied in this work, poly-l-lysine (PLL) and poly-l-glutamic acids (PGA) (Figure 5.4), have a lot of applications in various areas such as pharmaceutical therapy, fuel cells, and biosensors. As well as finding applications in the aforementioned technologies, polypeptide multilayer films have found a wealth of applications in medicine for example as polypeptide microcapsules for drug delivery[52] or for anti-microbial protection.[53] Thus, many studies have been carried out to understand their properties and characteristics, especially their immobilization and interaction with protons in aqueous solutions[54-55].

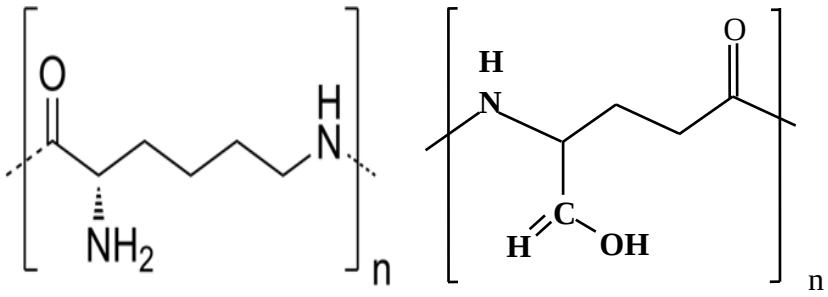

Figure 5.4 General molecular formula of PLL (left) and PGA (right).

5.4. Proton Lateral Diffusion

The movement of protons from source to sink sites is receiving increasing interest due to its crucial role in bioenergetic processes in the cell membrane, as well as photosynthesis in green plants, production of electricity in a fuel cell, electrochemical sensors, and electrochemical reactors[56]. In biological systems, the processes of proton transfer in membranes attract much attention, since hydrogen ions are involved directly in the processes of energy transformation in membrane in mitochondria, chloroplasts and bacteria. Proton translocation causes a pH-gradient that controls bioenergetic processes which couples electron transfer and synthesis of most common free-energy carrier in the biosphere adenosine triphosphate (ATP), as first suggested by Mitchell's chemiosmotic[57-61] or other energy requiring processes.[62] ATP, which provides the energy for most chemical reactions in the cells, is generated when an electrochemical proton gradient exists across the inner membrane. The gradient consists of two components: a difference in hydrogen ion concentration, or pH, and a difference in electric potential; the two together form 'protonmotive force'. A membrane-bound enzyme, ATP synthesis, provides a channel for protons to move down this gradient, generating an electrical potential which drives the synthesis of ATP in another part of the enzyme. This is carried out by trans-membrane proteins e.g. bacteriorhodopsin and cytochrome oxidase, which function as highly efficient proton pumps.[63]

Since the proposal of the chemiosmotic theory,[63-65] there has been a continuing debate about how protons that have been pumped across membrane reach another membrane protein that utilizes the established of pH gradient. Also, how do protons produced by proton generators get to proton consumers, both located on the same side of the membrane? Two competing modes for proton transfer have been proposed, one pathway

is delocalised diffusion,[66] based on the chemiosmotic theory, involves desorption and diffusion through intracellular bulk phase. Thus, the pumped protons equilibrate with the aqueous bulk phase before being consumed.[64,66-67] This mode has been challenge and another mode assigning a more active role of the membrane has emerged. The more efficient mechanism is localised lateral proton diffusion along the surface of an organised membrane,[62,65-70] which is thought to be facilitated through the hydrogen-bond network that forms between the polar lipids head groups and the water molecules at their surface, via a "hop and turn" mechanism.[71-73]

Protons and hydroxide ions diffuse much more rapidly through aqueous solution than say sodium, potassium and chloride, which was attributed to mediated transport via a Grotthuss mechanism, illustrated in Figure 5.5, by causing a rearrangement in and the hydrogen bonds-covalent bonds around the solvated proton propagates the protonic charge.[72-75]

Figure 5.5: The movement of protons through aqueous solution via a Grotthuss mechanism.[74]

In spite of many years of hard research and heated discussions, the exact details of this fundamental process remain obscure. Two opposing limits of solvent involvement in prototropic mobility have been proposed. The complete disorder mode pictured a proton hopping from a H_3O^+ to a freely rotating water molecule in the H_2OH^+....HOH complex. The opposite extreme is 'the relay mechanism' where the proton hops in large, static water cluster within an ordered hydrogen-bonded network. Proton diffusion according to the Grotthuss mechanism (via structural diffusion) occurs much faster than molecular

diffusion of an acidic carrier (e.g. H_3O^+) because it is uncoupled from the self-diffusion of its mass.[75] Measuring the rate of such process proved to be difficult with conventional techniques,[76] in addition different experimental techniques did not provide consistent results. This variation has caused great debate about the insufficiencies of the methods used[77] with criticism being aimed mainly at deficiencies in the methods used to obtain the data.

Several studies of lateral proton diffusion have been conducted at phospholipid monolayers spread at the air/water interface, purple membrane, bilayer lipid membrane and small unilaminar vesicles.[72-73] Initial studies by Teissié have reported high values for the lateral proton diffusion coefficient (at least 20 times that in aqueous solution),[67,78-79] by measuring fluorescence intensity changes of pH-sensitive fluorophores within Langmuir monolayer at distances over centimetre length scales from a mechanically stirred compartment where acid was injected. While further studies reported that the diffusion was simply facilitated; arguments about these results claimed that convection may contribute to the high rates obtained.[75] Using this method, it was suggested that protons are conducted predominantly by lateral diffusion in mixed phospholipid, monolayers,[80] and at protein films.[81-82] The methodology was the subject of strong criticism, not least because of the long distances and time over which measurements were made, with arguments of using a magnetic stirrer, introducing additional convective effects. Many theoretical and experimental investigations both supported and refuted this result. Indeed, contradictory data were obtained in laser pulse studies in vesicles and flash spectrophotometry on thylakoids, identify a retardation of severalfold comparing to bulk aqueous solution.[83-84]

Nevertheless, fast migration of protons along membranes has been observed in purple membrane compared to transfer into the bulk.[69,85] Long-range proton diffusion has also been observed along lipids [86]and in more recent studies employing the SECM technique in the induced desorption and feedback modes to study lateral proton diffusion in monolayers (Langmuir monolayers at water/air interface).[87] This approach allows interfacial dynamics and diffusion to be examined on small distance (micrometers) and time scale (milliseconds), and the well defined mass transport conditions in the SECM configuration permits the use of models to interpret the UME response. By the reduction of protons[87] or weak acids[88-89] (producing hydrogen) at an UME placed close to a Langmuir monolayer, deprotonation of the monolayer occurs locally that induces a proton diffusion gradient in the solution as well as the interface.[87-89]. This method illustrated that the in-plane lateral proton diffusion coefficient depends on the physical state and acid/base nature of the monolayer and was at most 15% of the magnitude in bulk solution at acidic monolayers (stearic acid),[87] and an order of magnitude lower than in aqueous bulk solution at (DPPS),[88] while it was so small that it could not be detected at zwitterionic monolayers (DPPC).[88] Thus, the proton transfer pathway along the membrane can be critically dependent on the distance between the source and the sink, the composition of the solution and the composition of the membrane.

This chapter introduces a new technique directly monitoring lateral proton diffusion at both surfaces modified with polyelectrolyte films and phospholipid bilayers with different head group. The technique combines the successful aspects of SECM with the use of fluorescence CLSM to measure pH changes at the bilayer surface in real time.

5.5. Result and Discussion

5.5.1. Characterisation of SLB-Modified Surfaces by AFM

In order to determine the extent of the surface on which bilayer had formed upon adsorption of 1 mg/ml solution of a pure egg phosphatidylcholine (EPC); or a mixture EPC: distearoyl phosphatidylglycerol1,2-ditetradecanoyl-sn-glycero-3-phospho-(1'-rac-glycerol)(DSPG) (in two molar ratios 80:20 and 60:40, respectively) in phosphate buffer to glass cover slip, *in situ* ScanAsyst-atomic force microscopy (SA-AFM) experiments were performed. The glass substrates were incubated for 4, 64, 94 and 128 min respectively in a 1 mg/mL SUV solution (filtered by 100 nm polycarbonate membrane). Representative *in situ* SA-AFM images of the surface of EPC: DSPG (molar ratios 80:20) are shown in Figure 5.6. They show a typical self-assembly process for formation of a lipid bilayer by small unilamellar vesicles (SUVs).

Incubation for 4 min (Figure 5.6 (a)) led to a complete coverage of SUVs on the wafer surface. After 46 min incubation (Figure 5.6 (b)), the surface became much rougher because the small unilamellar vesicles were fused into larger vesicles and to form a continuous planar lipid bilayer, the larger vesicles would collapse to form lipid bilayers. The lateral movement of lipid material associated with the coalescence of many patches (Figure 5.6 (b)) can trigger a cascade of subsequent events of coalescence with other neighbouring patches (Figure 5.6 (c)), leading to substantial modifications in the organization of the surface-bound lipid material. It is easily conceivable that also intact adsorbed vesicles can be ruptured by contact with the approaching active edge of a neighboring bilayer patch.

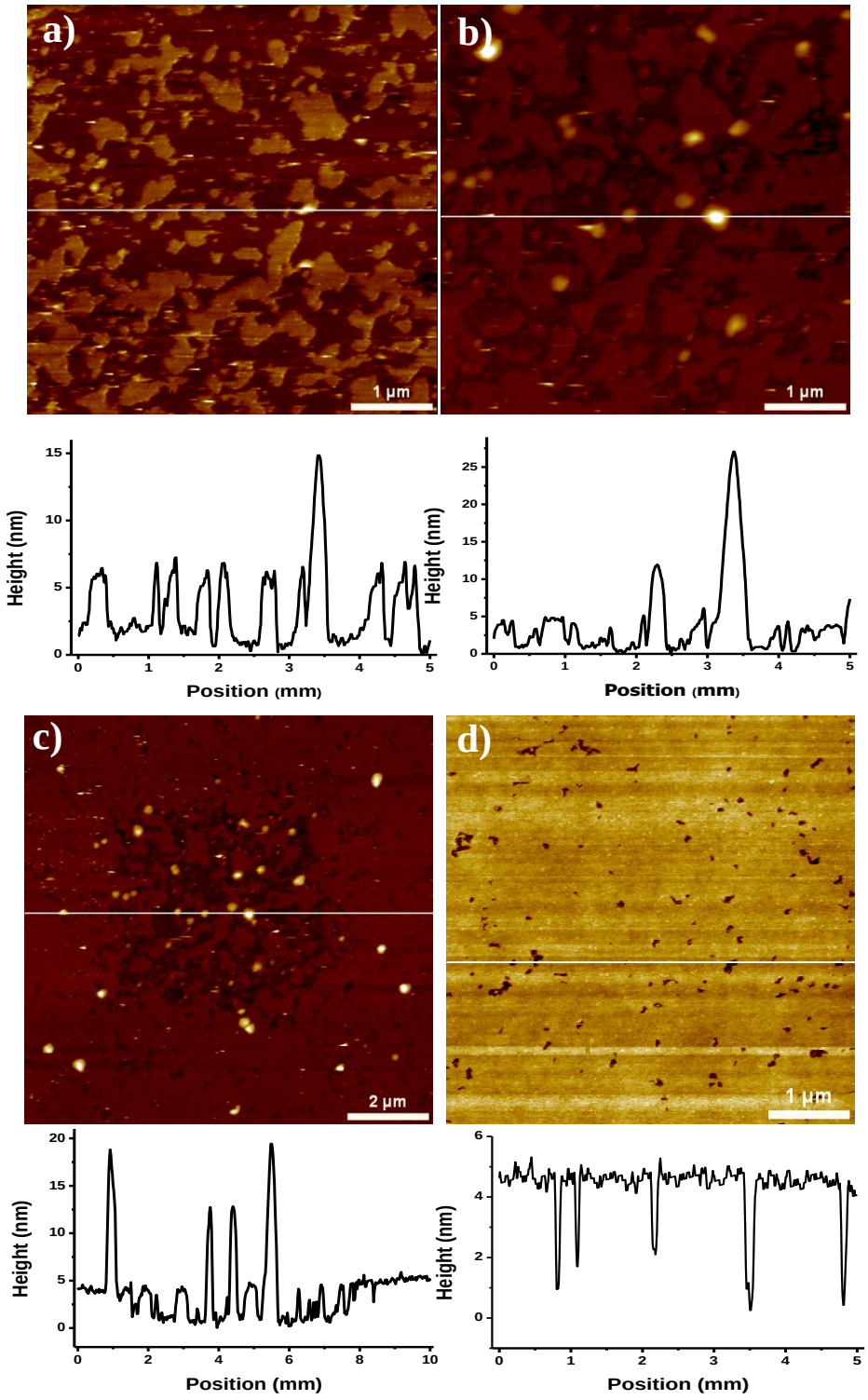

Figure 5.6: AFM height images (image size 5 × 5 µm^2) of small unilamellar vesicles (SUVs, filtered by 100 nm polycarbonate membrane) and their corresponding section analyses after incubation of a silicon wafer in a vesicle solution (1 mg/mL) for (a) 4 min, (b) 64 min, (c) 94, and (d) 128 min respectively. The height data through the cross-section shown.

The corresponding cross section profile presents a larger vesicle and also vesicles' rupturing to form bilayer patches. Due to the fusion of adjacent vesicles or bilayer patches, the bilayer area became bigger and the constant height of 5 nm[90] indicated they were extended flat bilayers. Bilayer patches coalesced with increasing vesicle exposure time as shown in Figure 5.7 (b), (c) and (d). Finally, after 128 min a continuous planar film was formed in Figure 5.7(d), and it entirely covered the substrate surface. From these AFM images, a conclusion can be drawn for the formation of SLBs: first the small unilamellar vesicles were adsorbed intact onto the substrate, and then they fused together into bigger vesicles and finally the bigger vesicles ruptured to a planar continuous bilayer.

5.5.2. Measurement of proton diffusion at modified surfaces

The studies herein on proton lateral diffusion used an extension of the method employed in chapters 4. The experimental details are outlined in Chapter 2, section 2.3.2. A UME was positioned close to the modified surfaces and used to alter the pH of the sub phase, via galvanostatically oxidising water to produce protons (Chapter 4, Equation 4.2). The resulting lateral flux of protons along the surface was monitored in real time, by imaging the change in light intensity by CLSM. A spatio-temporal fluorescence map showing interfacial proton dispersion was produced, allowing surface effect on diffusion to be identified. A schematic representation of the method is shown in Figure 5.7.

To validate the method qualitatively, CLSM imaging of proton dispersion in an aqueous solution of disodium fluorescein was carried out, close to PLL as inert surface and PLG as proton sink surface. In effect the electrostatic properties of the surface were charged

facilitating, the study of electrostatic interactions at positively and negatively charge surfaces. In this situation, the flux of protons produced at PLL by the electrode reaction could be used as controlled substrate, as described later, and compared to different active surfaces.

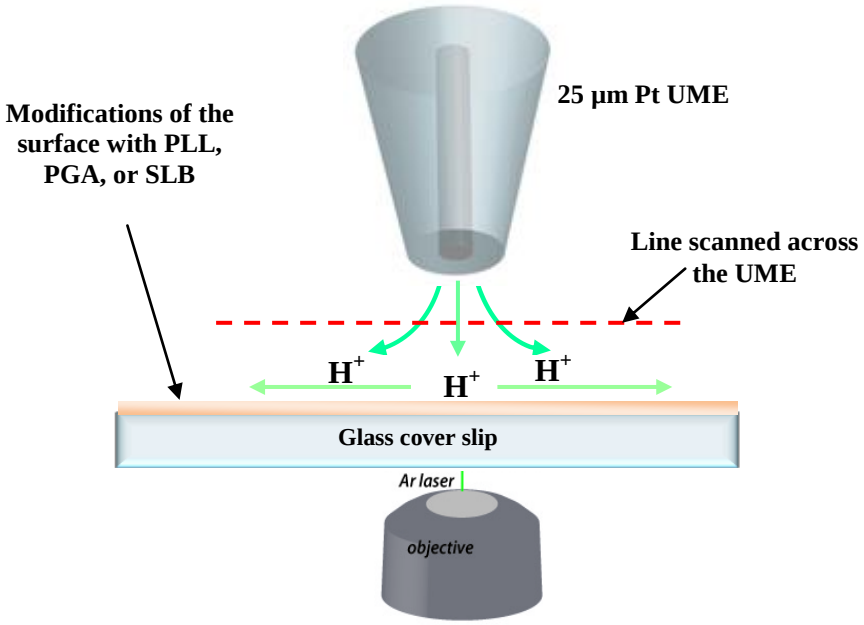

Figure 5.7: Schematic of the arrangement for SECM-CLSM studies of lateral proton diffusion, using the electrolysis of water for proton generation.

A range of small currents from 0.5 nA to 2 nA was applied to the UME and the resulting spatio-temporal images collected. Three typical images, captured during application of 0.5 nA, 1 nA and 2 nA next to PLL surfaces, are shown in Figure 5.8. The images clearly show the time at which the current was applied and the decrease in fluorescence at the interface, as the oxidation of water causes the proton concentration to rise. Each CLSM image was constructed from the numerical data, light intensity in arbitrary units (1 – 250) and distance (µm), collected from every line scanned. The time for a single line scan of length 228 µm (was selected across the centre of the electrode surface, as illustrated schematically in Chapter 2 Figure 2.13), was 2 ms and 2048 lines

were recorded. Plots of light intensity as a function of distance along the interface could be studied.

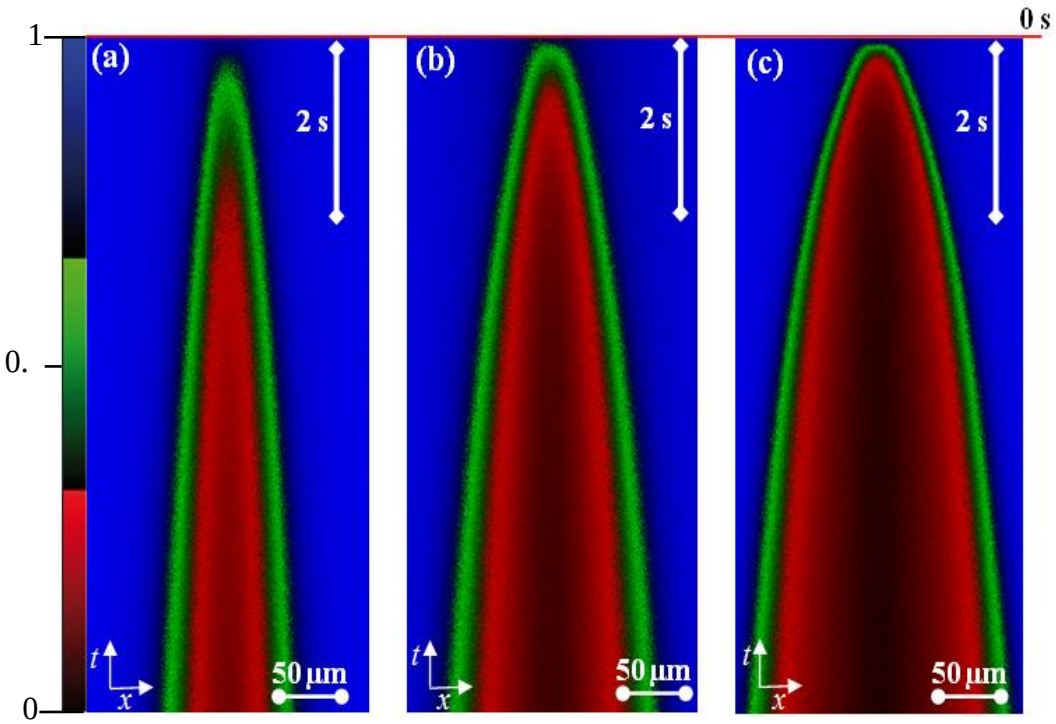

Figure 5.8: Spatio-temporal fluorescence CLSM images of proton dispersion at a PLL layer. Current applied: (a) 0.5 nA, (b) 1 nA and (c) 2 nA.

The sharp drop in light intensity, following the applied current, occurs at the electrode edge where the pH is suddenly decreased when protons are produced from the oxidation of water. The fluorescence intensity then rises steadily with distance away from the electrode, reflecting the pH profile that has been established in the small volume of solution between the electrode and the PLL interface. At the longer times following the applied current, the region of lower light intensity extends further away from the edge of the electrode indicating the diffusion of protons through the solution. The radius of the fluorescence profile was found to increase as the applied current was increased to 2 nA since the current controls the flux of protons away from the electrode surface. For relatively small currents (for example, 0.5 nA in Figure 5.8(a)), the fluorescence did not spread to the edge of the UME, rather it was localized around the centre. Clearly,

images can be compared qualitatively by observing the differences in both the rate at which the darker region spreads and the radial distance that is affected at the various currents used.

As described earlier (see Chapter 4, section 4.3.1), the radial distance from the electrode centre, corresponding to 50 % (pH 6.1) light intensity was determined by fitting a sigmoid curve to each time slice and recording the distance at 50 % light intensity. These distances were then plotted as a function of time following the application of the current, to produce a spatio-temporal profile for a concentration of protons corresponding to 50 % light intensity.

Figure 5.9 shows profiles at a PLL (as control surface) for four different applied currents. It is clear from the graphs that over the limited range of applied currents used in these experiments the profiles have similar trend that increased with time and exhibit exquisite spectral sensitivity and excellent temporal resolution illustrating the quality of the CLSM imaging system with a high signal-to-noise ratio. The variation in proton concentration and hence pH, along the PLL interface as a function of time, changes noticabley between applied currents of 0.5 to 2 nA.

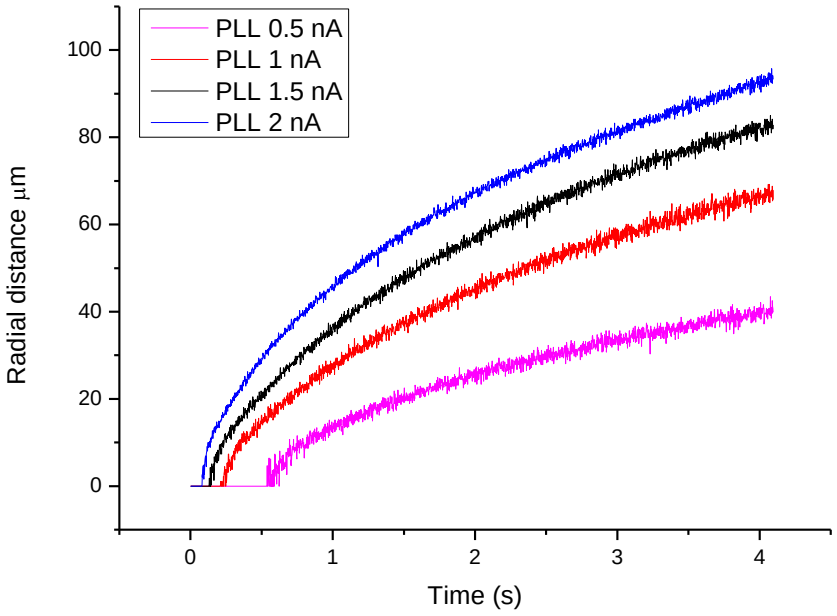

Figure 5.9: : Radial distance-time profile of the distance dependence of the pH 6.1 front in a thin layer of aqueous solution following the oxidation of water at a 25 µm diameter Pt UME, positioned 20 µm away from the PLL modified surfaces. Current applied: 2 nA, 1.5 nA , 1 nA and 0.5 nA.

Figure 5.10 shows the experimental profiles measured at PLL modified surface (positively charged) and PLL/PGA (negatively charged) bilayer respectively. PGA significantly retards the rate of proton diffusion compared to PLL. The proton field expands more in case of PLL due to the lower proton uptake. A time delay is also noticed for the PGA comparing to the PLL surface due to effect of the sink sites in the negatively charged on the PGA surface (carboxylate groups).

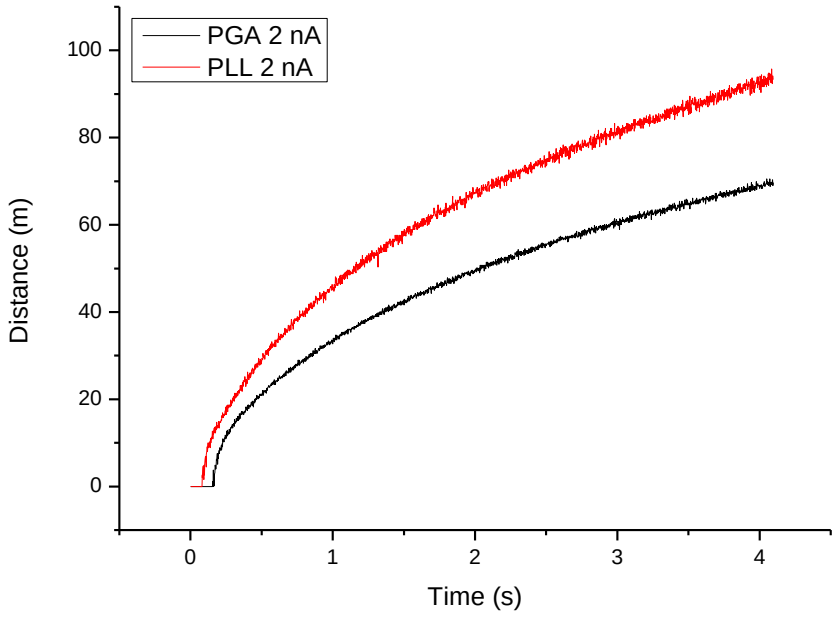

Figure 5.10: Radial distance-time profile dependence of the pH 6.1 front in a thin layer of aqueous solution following the oxidation of water at a 25 µm diameter Pt UME, positioned 20 µm above the PLL (red line), PGA (black line). Current applied: 2 nA.

Proton diffusion at Phospholipids bilayer

Lateral proton diffusion at phospholipid bilayers was explored by changing the lipid composition. Three different phospholipid systems were investigated: the zwitterionic, egg phosphatidylcholine (EPC); and a mixture of the acidic, distearoyl phosphatidylglycerol1,2-ditetradecanoyl-sn-glycero-3-phospho-(1'-rac-glycerol)(DSPG) with EPC in different molar ratios (20:80 and 40:60, respectively). The natural lipid extract Egg EPC has a zwitterionic headgroup where a negative charge (from the O^- in a phosphate group) and a positive charge (from the N^+ in an amino group) giving the head an overall neutral charge.[91] The lateral protons diffusion along planar bilayers investigation was carried by applying a range of anodic currents from 0.5 nA to 2 nA to the UME positioned close to the bilayer, and the resulting spatio-temporal images collected. A schematic representation of the method is shown in Figure 5.11.

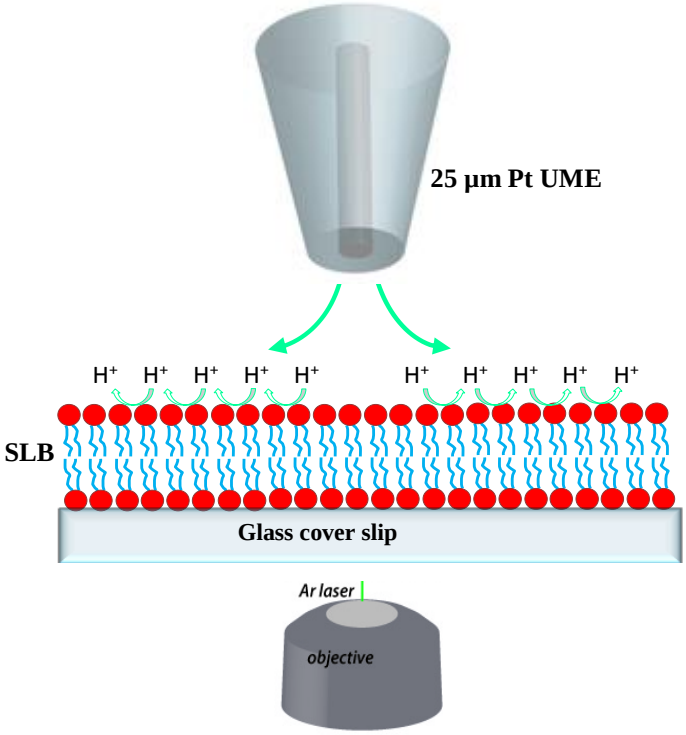

Figure 5.11 Schematic of the arrangement for SECM-CLSM studies of lateral proton diffusion at SLB, using the electrolysis of water for proton generation.

Typical CLSM images, captured during the application of 2 nA next each bilayer EPC, EPC:20%DSPG and EPC:40%DSPG bilayer respectively are shown in Figure 5.12, allowing visual comparisons to be made of the differnt bilayer of intersit. The dispersion of protons is clearly visible from the pattern of low light intensity that results from the protonation of the fluorophore in solution, as the oxidation of water takes place at the electrode directly above the bilayer.

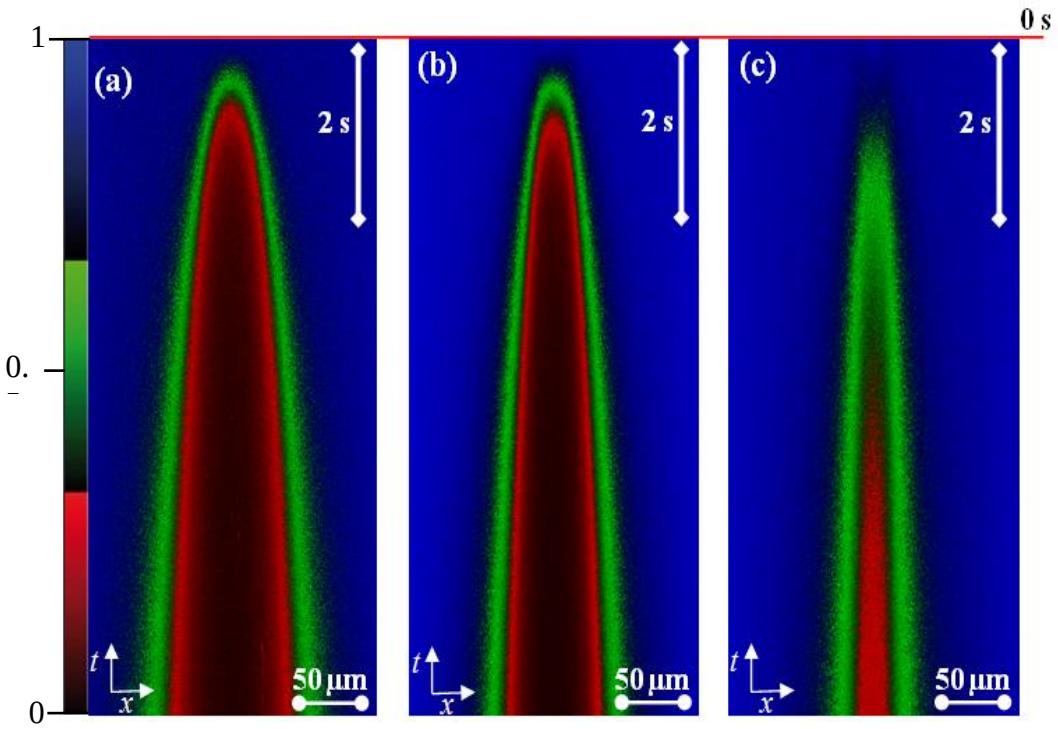

Figure 5.12: Spatio-temporal fluorescence CLSM images of proton dispersion at (a) EPC, (b) EPC:20%DSPG and (c) EPC:40%DSPG bilayer. Current applied 2 nA. The scale bar represents 50 µm.

Figure 5.13 shows the experimental profiles measured at a EPC and EPC:20%DSPG and EPC:40%DSPG bilayers respectively, at different currents, compared to the controls PLL, which assumes that proton dispersion is simply by hindered diffusion through solution and PGA as proton sink surface. Shown in Figure 5.13 (a) are the variation of proton diffusion front at pH 6.1 (and hence pH) as a function of time for a 2 nA current showing the inherent differences between the different surfaces with different chemical and electrostatic properties. The consistency of the data across these modified surfaces and for a range of currents provides further evidence of the sensitivity (in terms of both spatial and temporal resolution) of CLSM as a technique for probing proton diffusion, which allowed the study of these exceptionally fast processes *in situ* and in real time.

(a)

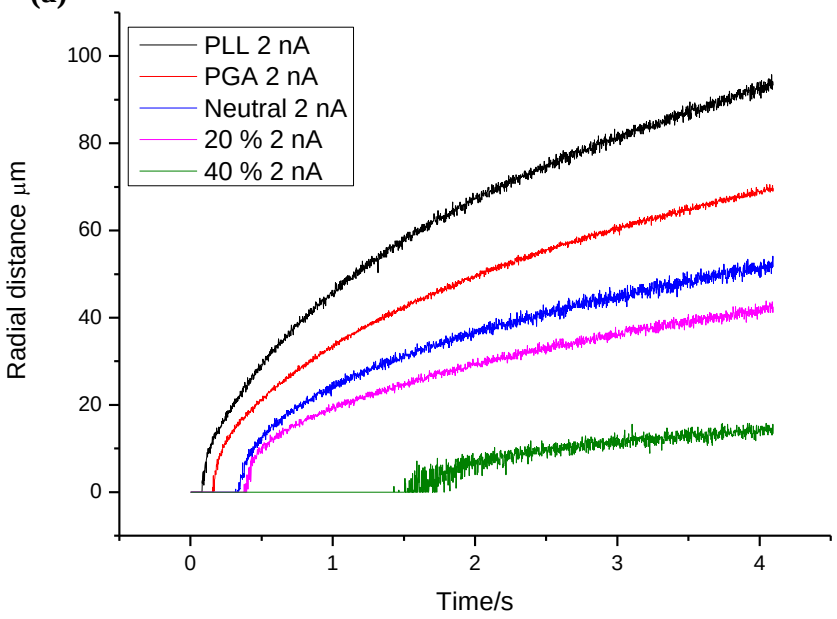
PLL 2 nA
PGA 2 nA
Neutral 2 nA
20 % 2 nA
40 % 2 nA
Radial distance µm
Time/s
0
20
40
60
80
100
0
1
2
3
4

(b)

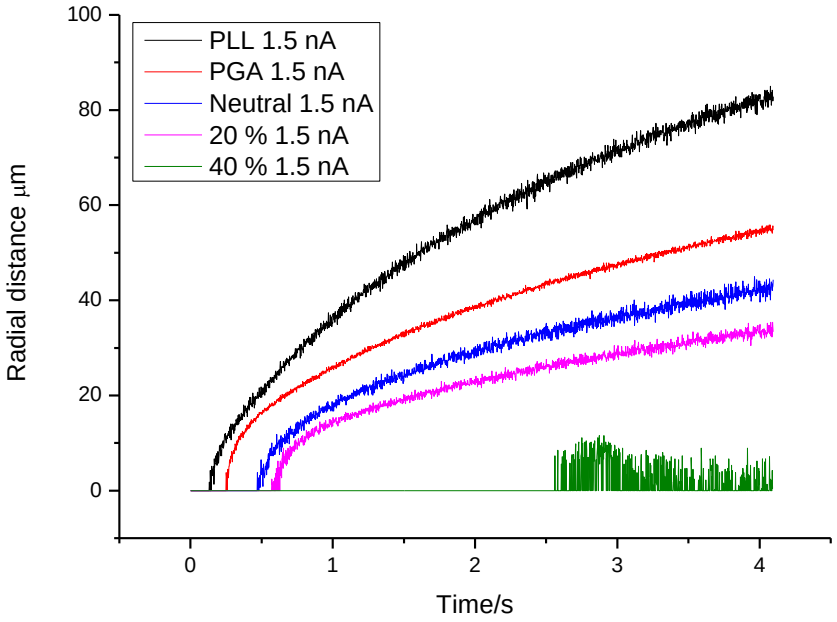
PLL 1.5 nA
PGA 1.5 nA
Neutral 1.5 nA
20 % 1.5 nA
40 % 1.5 nA
Radial distance µm
Time/s
0
20
40
60
80
100
0
1
2
3
4

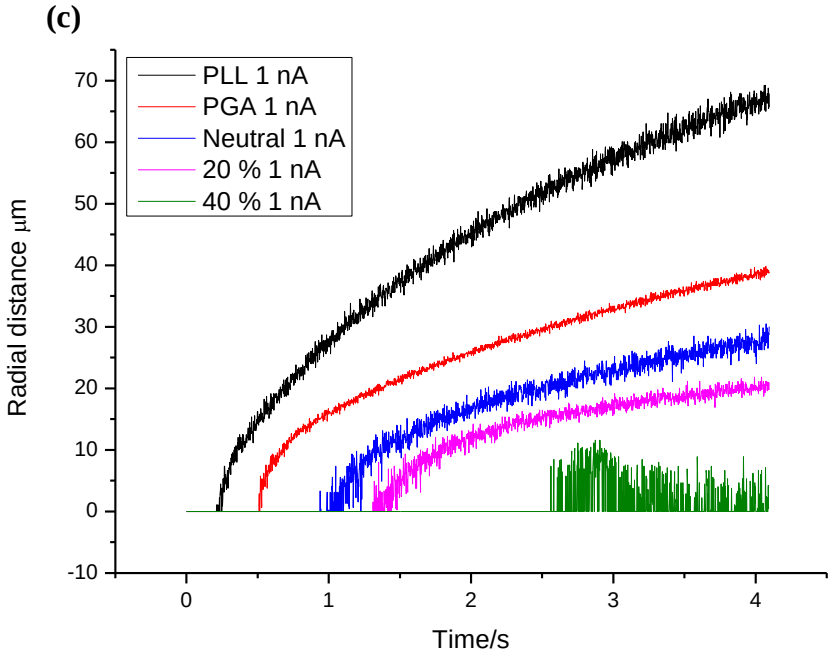

Figure 5.13: Radial distance-time profiles of the distance dependence of the pH 6.1 front in a thin layer of aqueous solution following the oxidation of water at a 25 µm diameter Pt UME, positioned 20 µm above PLL (black line), PLG (pink line), EPC(blue line), EPC:20%DSPG (red line) and EPC:40%DSPG (green line). Current applied: (a) 2 nA , (b) 1.5 nA and (c) 1 nA.

As can be seen, the nature of the surface strongly modulated the proton dispersion profiles obtained. For the PLL modified surface the proton is the most rapid and extensive: PLL thus behaves as an inert surface as discussed earlier. In all others cases, the presence of active surfaces in the front of PLG and the phospholipid bilayers with different head group significantly retards the rate and extent of proton diffusion. This is most apparent for all of the lipid bilayers, where the final distance (at 4 s) is less than half of that observed for the PLL surface.

Interestingly, at short times, within 2 s, for all applied current, there is a time delay that increase with increasing concentration of the negatively charged sites in the surface. This is diagnostic of these sites acting as sink sites towards the flux of proton generated.

The concentration of these sites has similar influence on the rate and extent of the proton dispersion. The rate of diffusion slows down and the distance that the concentration profile reaches is dependent on the composition of the surface. The rate of proton diffusion was slower at EPC:20%DSPG and EPC:40%DSPG respectively than at EPC bilayer; however, when currents below 2 nA were applied to the UME above EPC:40%DSPG bilayer, the light intensity dropped over a distance was not seen to spread in a radial direction; thus no proton profile was observed.

It can be seen also from the graphs that the proton diffusion expands more in case of lower proton uptake as in case of zwitterionic EPC than EPC:20%DSPG and EPC:40%DSPG bilayer respectively, as expected for proton at more negative charge surfaces. Interestingly, proton diffusion expands more in case of PLG more than both bilayers, DSPG and EPC. The consistency of the data across different modified surfaces and for a range of currents provides further evidence of the sensitivity (in terms of both spatial and temporal resolution) of CLSM as a technique for probing proton diffusion, which allowed the study of these exceptionally fast processes *in situ* and in real time.

The head groups of PGA, DSPG and EPC, indicating their charges (Figure 5.14); PGA has 2 carboxyl groups with an apparent *pK*a = of 4.4, both lipid DSPG and EPC have a phosphate group with a pK_a of ca. 2.2 However, DSPG has a negative charge due to the deprotonated phosphate group but EPC has no net charge due to the presence of an amino group with a pK_a of ca. 9.7. As protons are produced at the electrode close to the bilayer surface, the phosphate group on the DSPG bilayer will protonate more rapidly than the phosphate group on EPC because it is less acidic (larger pK_a value). It is

suggested that the greater availability of protonation sites at the membrane will retain protons at the surface and prevent spreading in solution.

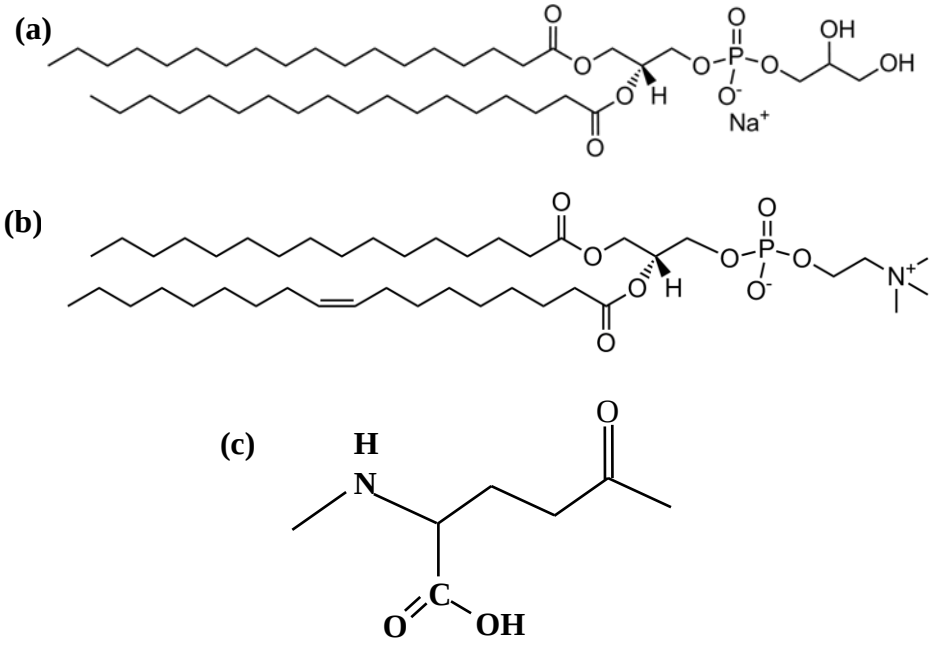

Figure 5.14: Structures of the head groups of (a) DSPG, (b) EPC and (c) PLG.

5.7. Conclusions

This chapter has described a new approach for studying proton diffusion at modified surfaces. In the experiments described herein, electrochemical methods were used as a means to induce surface processes which could then be followed in real-time and *in situ* using CLSM. The ability to form a supported lipid bilayer on the glass surface was demonstrated, and more importantly, the possibility of studying proton diffusion at modified surfaces was investigated. SECM has been successfully combined with CLSM to image proton diffusion at the surface of phospholipid bilayers using a Pt UME for local water oxidation, at the surface of thin films (PLL, PLL/PGA, EPC and DSPG) deposited on a solid substrate surface (glass). This powerful technique has established

well that proton diffusion near the PLL modified surface (positively charged) has a higher rate compared to the PGA surface (negatively charged); this was explained by the ability of the carboxylic groups to protonate at the beginning of this process, which would cause a time delay for the progress of the 50% intensity front (pH 6.1). EPC was also found to have a lower rate of proton diffusion than DSPG (negatively charged) that can be explained by the acid-base character of the phospholipids.

There are a number of factors can control the rate of lateral proton diffusion, which include the nature of the lipid, membrane fluidity and the buffering capacity and ionic strength of the solution. The value of the anodic current applied to the UME is another critical factor that controls the experimental observations. Due to the saturation of the substrate surface (active sites), there is a delay in the time to reach the steady-state current which increases as the current became lower. This has been well notified at active surface in comparison to inert surface. The ability to form a SLB on glass substrate and to monitor the proton diffusion on modified surfaces *in situ* and in real time, expands the applicability of CLSM to the study lateral proton diffusion in a biologically relevant environment. Thus, the well-defined delivery methods employed in these experiments described now need to be quantitatively modelled to further understand the reaction mechanisms and to resolve what is happening.

5.7. Conclusions

This chapter has described a new approach for studying proton diffusion at modified surfaces. In the experiments described herein, electrochemical methods were used as a means to induce surface processes which could then be followed in real-time and *in situ* using CLSM. The ability to form a supported lipid bilayer on the glass surface was demonstrated, and more importantly, the possibility of studying proton diffusion at modified surfaces was investigated. SECM has been successfully combined with CLSM to image proton diffusion at the surface of phospholipid bilayers using a Pt UME for local water oxidation, at the surface of thin films (PLL, PLL/PGA, EPC and DSPG) deposited on a solid substrate surface (glass). This powerful technique has established well that proton diffusion near the PLL modified surface (positively charged) has a higher rate compared to the PGA surface (negatively charged); this was explained by the ability of the carboxylic groups to protonate at the beginning of this process, which would cause a time delay for the progress of the 50% intensity front (pH 6.1). EPC was also found to have a lower rate of proton diffusion than DSPG (negatively charged) that can be explained by the acid-base character of the phospholipids.

There are a number of factors that can control the rate of lateral proton diffusion, which include the nature of the lipid, membrane fluidity and the buffering capacity and ionic strength of the solution. The value of the anodic current applied to the UME is another critical factor that controls the experimental observations. Due to the saturation of the substrate surface (active sites), there is a delay in the time to reach the steady-state current which increases as the current became lower. This has been well notified at active surface in comparison to inert surface. The ability to form a SLB on glass substrate and to monitor the proton diffusion on modified surfaces *in situ* and in real

time, expands the applicability of CLSM to the study lateral proton diffusion in a biologically relevant environment. Thus, the well-defined delivery methods employed in these experiments described now need to be quantitatively modelled to further understand the reaction mechanisms and to resolve what is happening.

5.8. References

(1) Fiedler, S.; Broecker, J.; Keller, S. *Cellular and Molecular Life Sciences* **2010**, *67*, 1779.
(2) McConnell, H. M.; Watts, T. H.; Weis, R. M.; Brian, A. A. *Biochimica Et Biophysica Acta* **1986**, *864*, 95.
(3) Perez, T. D.; Nelson, W. J.; Boxer, S. G.; Kam, L. *Langmuir* **2005**, *21*, 11963.
(4) Kam, L. C. *Journal of Structural Biology* **2009**, *168*, 3.
(5) Castellana, E. T.; Cremer, P. S. *Surface Science Reports* **2006**, *61*, 429.
(6) O'Rourke, B. In *Annual Review of Physiology* 2007; Vol. 69, p 19.
(7) Jain, M., K. *Introduction to Biological Membranes*; 1ed ed.; John Wiley & Sons: USA, 1938.
(8) Jain, M., K., *The Bimolecular Lipid Membranes*; 1ed ed.; Van Nostrand Reinhold Company,: USA, 1972.
(9) Stryer, L. *Biochemistry*; 4th ed.; W. H. Freeman and Company: New York, USA, 1995.
(10) Karnovsky, M. J.; Kleinfeld, A. M.; Hoover, R. L.; Klausner, R. D. *Journal of Cell Biology* **1982**, *94*, 1.
(11) Cullis, P. R.; Dekruijff, B. *Current Contents/Life Sciences* **1992**, 11.
(12) Cullis, P. R.; Dekruijff, B. *Biochimica Et Biophysica Acta* **1979**, *559*, 399.
(13) Edidin, M. *Nature Reviews Molecular Cell Biology* **2003**, *4*, 414.
(14) Gunstone, F. D. H., J. L.; Padley, F. B. *The Lipid Handbook;*; Chapman and Hall:: London, 1986.
(15) Orbach, E.; Finkelstein, A. *Journal of General Physiology* **1980**, *75*, 427.
(16) Grime, J. M. A.; Edwards, M. A.; Rudd, N. C.; Unwin, P. R. *Proceedings of the National Academy of Sciences of the United States of America* **2008**, *105*, 14277.
(17) Tien, H. T. *Bilayer Lipid Membranes (BLM). Theory and Practice*; Marcel Dekker: New York, 1974.
(18) Suarezisla, B. A.; Wan, K.; Lindstrom, J.; Montal, M. *Biochemistry* **1983**, *22*, 2319.
(19) Dominska, M.; Krysinski, P.; Blanchard, G. J. *Langmuir* **2008**, *24*, 8785.
(20) Nikolov, V.; Lin, J.; Merzlyakov, M.; Hristova, K.; Searson, P. C. *Langmuir* **2007**, *23*, 13040.
(21) Cho, N.-J.; Frank, C. W.; Kasemo, B.; Hook, F. *Nature Protocols* **2010**, *5*, 1096.
(22) Seantier, B.; Breffa, C.; Felix, O.; Decher, G. *Journal of Physical Chemistry B* **2005**, *109*, 21755.
(23) Nollert, P.; Kiefer, H.; Jahnig, F. *Biophysical Journal* **1995**, *69*, 1447.
(24) Radler, J.; Strey, H.; Sackmann, E. *Langmuir* **1995**, *11*, 4539.
(25) Reuter, M.; Schwieger, C.; Meister, A.; Karlsson, G.; Blume, A. *Biophysical Chemistry* **2009**, *144*, 27.
(26) Lapinski, M. M.; Castro-Forero, A.; Greiner, A. J.; Ofoli, R. Y.; Blanchard, G. J. *Langmuir* **2007**, *23*, 11677.
(27) Frisken, B. J.; Asman, C.; Patty, P. J. *Langmuir* **2000**, *16*, 928.
(28) Maulucci, G.; De Spirito, M.; Arcovito, G.; Boffi, F.; Castellano, A. C.; Briganti, G. *Biophysical Journal* **2005**, *88*, 3545.
(29) Barenholz, Y.; Gibbes, D.; Litman, B. J.; Goll, J.; Thompson, T. E.; Carlson, F. D. *Biochemistry* **1977**, *16*, 2806.
(30) Olivieri, M. P.; Wollman, R. M.; Hurley, M. I.; Swartz, M. F. *Journal of Adhesion* **2010**, *86*, 111.
(31) Binks, B. P. *Advances in Colloid and Interface Science* **1991**, *34*, 343.

(32) Ma, C.; Srinivasan, M. P.; Waring, A. J.; Lehrer, R. I.; Longo, M. L.; Stroeve, P. *Colloids and Surfaces B-Biointerfaces* **2003**, *28*, 319.
(33) Kraft, M. L.; Weber, P. K.; Longo, M. L.; Hutcheon, I. D.; Boxer, S. G. *Science* **2006**, *313*, 1948.
(34) Zhang, L. F.; Spurlin, T. A.; Gewirth, A. A.; Granick, S. *Journal of Physical Chemistry B* **2006**, *110*, 33.
(35) Papo, N.; Shai, Y. *Biochemistry* **2003**, *42*, 458.
(36) Munro, J. C.; Frank, C. W. *Langmuir* **2004**, *20*, 10567.
(37) Benes, M.; Billy, D.; Benda, A.; Speijer, H.; Hof, M.; Hermens, W. T. *Langmuir* **2004**, *20*, 10129.
(38) Barman, H.; Walch, M.; Latinovic-Golic, S.; Dumrese, C.; Dolder, M.; Groscurth, P.; Ziegler, U. *Journal of Membrane Biology* **2006**, *212*, 29.
(39) Richter, R.; Mukhopadhyay, A.; Brisson, A. *Biophysical Journal* **2003**, *85*, 3035.
(40) Richter, R. P.; Brisson, A. R. *Biophysical Journal* **2005**, *88*, 3422.
(41) Roberts, G. G. *Langmuir-Blodgett films*; illustrated ed.; Plenum Press: New York, 1990.
(42) Keller, C. A.; Kasemo, B. *Biophysical Journal* **1998**, *75*, 1397.
(43) Burns, A. R. *Langmuir* **2003**, *19*, 8358.
(44) Kucerka, N.; Nagle, J. F.; Sachs, J. N.; Feller, S. E.; Pencer, J.; Jackson, A.; Katsaras, J. *Biophysical Journal* **2008**, *95*, 2356.
(45) Generosi, J.; Margaritondo, G.; Sanghera, J. S.; Aggarwal, I. D.; Tolk, N. H.; Piston, D. W.; Castellano, A. C.; Cricenti, A. *Applied Physics Letters* **2006**, *89*.
(46) Lee, C. S.; Bain, C. D. *Biochimica Et Biophysica Acta-Biomembranes* **2005**, *1711*, 59.
(47) Mager, M. D.; Almquist, B.; Melosh, N. A. *Langmuir* **2008**, *24*, 12734.
(48) Schmitt, J.; Decher, G.; Dressick, W. J.; Brandow, S. L.; Geer, R. E.; Shashidhar, R.; Calvert, J. M. *Advanced Materials* **1997**, *9*, 61.
(49) Decher, G.; Hong, J. D.; Schmitt, J. *Thin Solid Films* **1992**, *210*, 831.
(50) Lee, H.; Kepley, L. J.; Hong, H. G.; Akhter, S.; Mallouk, T. E. *Journal of Physical Chemistry* **1988**, *92*, 2597.
(51) Bertrand, P.; Jonas, A.; Laschewsky, A.; Legras, R. *Macromolecular Rapid Communications* **2000**, *21*, 319.
(52) Leguen, E.; Chassepot, A.; Decher, G.; Schaaf, P.; Voegel, J.-C.; Jessel, N. *Biomolecular Engineering* **2007**, *24*, 33.
(53) Boulmedais, F.; Frisch, B.; Etienne, O.; Lavalle, P.; Picart, C.; Ogier, J.; Voegel, J. C.; Schaaf, P.; Egles, C. *Biomaterials* **2004**, *25*, 2003.
(54) Hamano, Y.; Nicchu, I.; Shimizu, T.; Onji, Y.; Hiraki, J.; Takagi, H. *Applied Microbiology and Biotechnology* **2007**, *76*, 873.
(55) Pasut, G.; Veronese, F. M. *Progress in Polymer Science* **2007**, *32*, 933.
(56) Kreuer, K.-D. *Chemistry of Materials* **1996**, *8*, 610.
(57) Gennis, R. B. *Biomembranes: Molecular Structure and Function* New York, 1989.
(58) Medvedev, E. S.; Stuchebrukhov, A. A. *Journal of Physics-Condensed Matter* **2011**, *23*.
(59) Mulkidjanian, A. Y.; Heberle, J.; Cherepanov, D. A. *Biochimica Et Biophysica Acta-Bioenergetics* **2006**, *1757*, 913.
(60) Agmon, N.; Gutman, M. *Nat Chem* **2011**, *3*, 840.
(61) Serowy, S.; Saparov, S. M.; Antonenko, Y. N.; Kozlovsky, W.; Hagen, V.; Pohl, P. *Biophysical Journal* **2003**, *84*, 1031.

(62) Georgievskii, Y.; Medvedev, E. S.; Stuchebrukhov, A. A. *Biophysical Journal* **2002**, *82*, 2833.
(63) Ferguson, S. J. *Current Biology* **1995**, *5*, 25.
(64) Mitchell, P. *Nature* **1961**, *191*, 144.
(65) Heberle, J.; Riesle, J.; Thiedemann, G.; Oesterhelt, D.; Dencher, N. A. *Nature* **1994**, *370*, 379.
(66) Antonenko, Y. N.; Kovbasnjuk, O. N.; Yaguzhinsky, L. S. *Biochimica Et Biophysica Acta* **1993**, *1150*, 45.
(67) Prats, M.; Teissie, J.; Tocanne, J. F. *Nature* **1986**, *322*, 756.
(68) Kell, D. B. *Biochimica Et Biophysica Acta* **1979**, *549*, 55.
(69) Alexiev, U.; Scherrer, P.; Mollaaghababa, R.; Khorana, H. G.; Heyn, M. P. *Biophysical Journal* **1995**, *68*, A321.
(70) Georgievskii, Y.; Medvedev, E. S.; Stuchebrukhov, A. A. *Journal of Chemical Physics* **2002**, *116*, 1692.
(71) Agmon, N. *Chem. Phys. Lett.* **1995**, *244*, 456.
(72) Agmon, N. *Chemical Physics Letters* **1995**, *244*, 456.
(73) Agmon, N. *Abstracts of Papers of the American Chemical Society* **1995**, *210*, 328.
(74) Compton, R. G. S., G. H. W. *Electrode Potentials*; PressOxford University UK, 1998.
(75) Gutman, M.; Nachliel, E. *Biochimica Et Biophysica Acta-Bioenergetics* **1995**, *1231*, 123.
(76) Scherrer, P. *Nature* **1995**, *374*, 222.
(77) Sakurai, I.; Suzuki, T.; Sakurai, S. *Biochimica Et Biophysica Acta* **1989**, *985*, 101.
(78) Teissie, J.; Prats, M.; Soucaille, P.; Tocanne, J. F. *Proceedings of the National Academy of Sciences of the United States of America* **1985**, *82*, 3217.
(79) Prats, M.; Tocanne, J. F.; Teissie, J. *European Journal of Biochemistry* **1985**, *149*, 663.
(80) Gabriel, B.; Prats, M.; Teissie, J. *Biochemistry* **1991**, *30*, 9359.
(81) Antonenko, Y. N.; Pohl, P. *European Biophysics Journal with Biophysics Letters* **2008**, *37*, 865.
(82) Gabriel, B.; Teissie, J. *Proceedings of the National Academy of Sciences of the United States of America* **1996**, *93*, 14521.
(83) Nachliel, E.; Gutman, M. *Journal of the American Chemical Society* **1988**, *110*, 2629.
(84) Gutman, M.; Nachliel, E.; Moshiach, S. *Biochemistry* **1989**, *28*, 2936.
(85) Nachliel, E.; Gutman, M.; Kiryati, S.; Dencher, N. A. *Proceedings of the National Academy of Sciences of the United States of America* **1996**, *93*, 10747.
(86) Gabriel, B.; Prats, M.; Teissie, J. *Biochimica Et Biophysica Acta-Bioenergetics* **1994**, *1186*, 172.
(87) Slevin, C. J.; Unwin, P. R. *Journal of the American Chemical Society* **2000**, *122*, 2597.
(88) Zhang, J.; Unwin, P. R. *Journal of the American Chemical Society* **2002**, *124*, 2379.
(89) Zhang, J.; Unwin, P. R. *Phys. Chem. Chem. Phys.* **2002**, *4*, 3814.
(90) Reviakine, I.; Brisson, A. *Langmuir* **2000**, *16*, 1806.
(91) Notter, R. H. *Lung surfactants: basic science and clinical applications*; 1st ed.; CRC Press: New York, 2000; Vol. 149.
(92) Branden, M.; Sanden, T.; Brzezinski, P.; Widengren, J. *Proceedings of the National Academy of Sciences of the United States of America* **2006**, *103*, 19766.

(93) Medvedev, E. S.; Stuchebrukhov, A. A. *Journal of Mathematical Biology* **2006**, *52*, 209.
(94) Springer, A.; Hagen, V.; Cherepanov, D. A.; Antonenko, Y. N.; Pohl, P. *Proceedings of the National Academy of Sciences of the United States of America* **2011**, *108*, 14461.
(95) Cherepanov, D. A.; Feniouk, B. A.; Junge, W.; Mulkidjanian, A. Y. *Biophysical Journal* **2003**, *85*, 2069.
(96) Smondyrev, A. M.; Voth, G. A. *Biophysical Journal* **2002**, *82*, 1460.
(97) Cherepanov, D. A.; Junge, W.; Mulkidjanian, A. Y. *Biophysical Journal* **2004**, *86*, 665.

Conclusion

As highlighted in the introduction (chapter 1), this thesis has considered various experimental techniques and simulation, for describing diffusion in electrochemical systems and beyond. A key aspect of the thesis has been the quantification of concentration gradients produced at active surfaces during an electrode reaction with a wide range of materials. Progress has been made in each area investigated, providing a foundation for the future. The combination of fluorescence confocal laser scanning microscopy (CLSM) with electrochemical techniques has allowed such processes to be visualised and the defining parameters to be determined. Many electrode and interface processes are accompanied by local changes in pH, and the methodology described in this thesis could find wider application in quantifying associated pH gradients and in providing mechanistic information.

Chapter 3 considered the concentration profile of redox reactions adjacent to novel OT-UMEs comprising ultrathin films of SWNTs. The SWNT films are grown by cCVD on a single crystal ST-cut quartz substrate. They exhibited both complete transparency and disc-shaped UME characteristics. In particular, the OT-SWNT-UMEs demonstrated the attractive properties of small-scale electrodes, e.g., high diffusion rates and good signal-to-noise, with the ability to probe electrochemical processes optically, from the rear of the electrode. This enabled optical measurements of the solution, close to the electrode

surface, without significant interference from absorption or scattering processes. The electrochemical activity of the UMEs was quantified using CLSM with the temporal and spatial resolution in the millisecond and micrometer range, respectively. The investigation involved use of fluorophores which were either redox active ($Ru(bpy)_3^{2+}$ oxidation) or had the luminescent properties which were pH sensitive (fluorescein in oxygen reduction reaction (ORR)). These proof-of-concept experiments broaden the potential applications of the introduced SWNT disc UMEs as reliable and effective sensors for broad optical and electrochemical applications. Further developments in OT-UME fabrication will allow quantitative analysis of reaction dynamics at a greatly enhanced level. Initial improvements in the OT-UME design by using thinner quartz substrates, both fused quartz and single crystal, would enable use of higher magnification objectives with increased resolution capabilities which should allow the more faithful measurement of concentration profiles. With the suggested improvement, several classes of experiments could be carried out such as electrogenerated chemiluminescence studies of species providing intense luminescence. The technique would be particularly useful in detecting defects in electrodes and active sites on heterogeneous electrode surfaces.

An important outcome of the studies herein is the ability to assess the effectiveness of inhibitors on enamel dissolution that could be expanded to include many types of substrate. The use of CLSM combined scanning electrochemical microscopy (SECM) provides a very powerful tool, which enables the visualisation of the proton gradient established near the surface of an UME, thus permitting the tracking of proton movement on various substrates located nearby. This provided an analytical method with high spatial and temporal resolution permitting sub-second analysis of treatment

effects on enamel substrates. Localised dissolution of dental enamel has been achieved by the application of a proton flux to the enamel surface from a UME positioned in close proximity to the enamel, in aqueous solution. It has been shown that fluoride and zinc as dissolution inhibitors cause changes in the morphology of pH profile that forms on treated enamel compared to untreated enamel due to their barrier effect. Fluoride treatment of enamel provides an initial barrier to proton attack with a rate constant similar to that of zinc treated enamel, but this barrier only lasted for approximately one second before returning to a rate comparable to that of untreated enamel. Experimental observations were quantified by solving the diffusion equations numerically. The experimental data were compared to the finite element model, which allowed rate constants of dissolution to be assigned for different surface treatments at different proton fluxes controlled by the applied current. Simulated pH profiles were found to be in close agreement with the experimental CLSM pH profiles, including inhibitor effects at short and long time scales. Based on these data, CLSM-SECM appears to be particularly powerful and it would be possible to assess many complex inhibitors of acid erosion with this method.

A new approach has been developed and tested to examining proton uptake and lateral proton diffusion at thin films surfaces (polymers, lipid bilayers and related systems), to further extend the capabilities of the method developed using CLSM combined with SECM to directly visualise proton fluxes at modified surfaces. The methodology was verified by application to galvanostatic water reduction as a well characterised system. For studies of proton diffusion, silica surfaces were modified by multilayer assemblies of poly-L-lysine (PLL) and poly-L-glutamic acid (PLG) thereby changing the electrostatic properties of the surface and facilitating the study of different electrostatic

interactions. The resulting surface charge is positive in the case of PLL and negative in the case of a PLL/PLG bilayer. Both PLL and PGA functionalised interfaces were studied as controls for comparison to the lipid bilayers. The different surfaces had a significant impact on the extent of proton uptake. In the future phospholipids with hydrocarbon chains of different lengths or degrees of unsaturation, could be used to examine the effects of packing and organisation of the bilayer on proton uptake. The fluidity of the bilayer may also have an effect on proton diffusion and this could be investigated by incorporating cholesterol into the phospholipid bilayer. The incorporation of protein channels such as bacterial photosynthetic membrane proteins, light-harvesting complex 2 (LH2), and light-harvesting core complex (LH1-RC) could also be the subject of future work. This can be achieved by introducing spacers between the membrane and the substrate using polymer cushions and pillars as the typical supported lipid bilayer is separated from the surface of the substrate by a 1-2 nm of water layer, which has been believed this water layer cannot provide enough space for large protuberant domains of membrane proteins. The high resolution of the technique would allow visualisation of the diffusion profile through labelling the bilayer itself with a pH sensitive fluorophore in addition to the one that exists in the bulk solution. Simulation model will now need to be developed to describe the proton gradient established at the UME surface in the presence of an inert and active substrate in order to obtain quantitative data and deduce uptake extent and lateral proton diffusion.

Appendix

Attached to the thesis there are a series of movies related to experiments described in chapter 3, 4 and 5.

Movie 1: Oxidation of 10 mM $Ru(bpy)_3^{2+}$ in 0.1 M NaCl at a 50 µm diameter disc-shaped OT-SWNTs-UME

Movie 2: Proton gradient following the oxidation of water in 8 µM fluorescein solution with 0.1 M potassium nitrate at a 25 µm diameter Pt UME. Current applied: 20 nA.

Movie 3: Proton gradient following the oxidation of water in 8 µM fluorescein solution with 0.1 M potassium nitrate at a 25 µm diameter Pt UME, positioned 20 µm away from glass surfaces. Current applied: 20 nA

Movie 4: Proton gradient following the oxidation of water in 8 µM fluorescein solution with 0.1 M potassium nitrate at a 25 µm diameter Pt UME, positioned 20 µm away from enamel surface. Current applied: 20 nA

Movie 5: Proton gradient following the oxidation of water in 8 µM fluorescein solution with 0.1 M potassium nitrate at a 25 µm diameter Pt UME, positioned 20 µm away from modified surface. Current applied: 20 nA